

REPORT DOCUMENTATION PAGE

Form Approved
OMB No. 0704-0188

Public reporting burden for this collection of information is estimated to average 1 hour per response, including the time for reviewing instructions, searching existing data sources, gathering and maintaining the data needed, and completing and reviewing the collection of information. Send comments regarding this burden estimate or any other aspect of this collection of information, including suggestions for reducing this burden, to Washington Headquarters Services, Directorate for Information Operations and Reports, 1215 Jefferson Davis Highway, Suite 1204, Arlington, VA 22202-4302, and to the Office of Management and Budget, Paperwork Reduction Project (0704-0188), Washington, DC 20503.

1. AGENCY USE ONLY (Leave blank)			2. REPORT DATE	3. REPORT TYPE AND DATES COVERED
			9 Dec 96	
4. TITLE AND SUBTITLE <i>Utah Local Area Model Sensitivity To Boundary Conditions For Summer Rain Simulations</i>			5. FUNDING NUMBERS	
6. AUTHOR(S) <i>Steven Paul DeSordi</i>				
7. PERFORMING ORGANIZATION NAME(S) AND ADDRESS(ES) <i>University of Utah</i>			8. PERFORMING ORGANIZATION REPORT NUMBER <i>96-084</i>	
9. SPONSORING / MONITORING AGENCY NAME(S) AND ADDRESS(ES) DEPARTMENT OF THE AIR FORCE AFIT/CI 2950 P STREET, BLDG 125 WRIGHT-PATTERSON AFB OH 45433-7765			10. SPONSORING / MONITORING AGENCY REPORT NUMBER	
11. SUPPLEMENTARY NOTES				
12a. DISTRIBUTION / AVAILABILITY STATEMENT <i>Unlimited</i>			12b. DISTRIBUTION CODE	
13. ABSTRACT (Maximum 200 words)				
14. SUBJECT TERMS				
15. NUMBER OF PAGES <i>12</i>				
16. PRICE CODE				
17. SECURITY CLASSIFICATION OF REPORT	18. SECURITY CLASSIFICATION OF THIS PAGE	19. SECURITY CLASSIFICATION OF ABSTRACT	20. LIMITATION OF ABSTRACT	

GENERAL INSTRUCTIONS FOR COMPLETING SF 298

The Report Documentation Page (RDP) is used in announcing and cataloging reports. It is important that this information be consistent with the rest of the report, particularly the cover and title page. Instructions for filling in each block of the form follow. It is important to *stay within the lines* to meet *optical scanning requirements*.

Block 1. Agency Use Only (Leave blank).

Block 2. Report Date. Full publication date including day, month, and year, if available (e.g. 1 Jan 88). Must cite at least the year.

Block 3. Type of Report and Dates Covered.

State whether report is interim, final, etc. If applicable, enter inclusive report dates (e.g. 10 Jun 87 - 30 Jun 88).

Block 4. Title and Subtitle. A title is taken from the part of the report that provides the most meaningful and complete information. When a report is prepared in more than one volume, repeat the primary title, add volume number, and include subtitle for the specific volume. On classified documents enter the title classification in parentheses.

Block 5. Funding Numbers. To include contract and grant numbers; may include program element number(s), project number(s), task number(s), and work unit number(s). Use the following labels:

C - Contract	PR - Project
G - Grant	TA - Task
PE - Program Element	WU - Work Unit
	Accession No.

Block 6. Author(s). Name(s) of person(s) responsible for writing the report, performing the research, or credited with the content of the report. If editor or compiler, this should follow the name(s).

Block 7. Performing Organization Name(s) and Address(es). Self-explanatory.

Block 8. Performing Organization Report Number. Enter the unique alphanumeric report number(s) assigned by the organization performing the report.

Block 9. Sponsoring/Monitoring Agency Name(s) and Address(es). Self-explanatory.

Block 10. Sponsoring/Monitoring Agency Report Number. (If known)

Block 11. Supplementary Notes. Enter information not included elsewhere such as: Prepared in cooperation with...; Trans. of...; To be published in.... When a report is revised, include a statement whether the new report supersedes or supplements the older report.

Block 12a. Distribution/Availability Statement.

Denotes public availability or limitations. Cite any availability to the public. Enter additional limitations or special markings in all capitals (e.g. NOFORN, REL, ITAR).

DOD - See DoDD 5230.24, "Distribution Statements on Technical Documents."

DOE - See authorities.

NASA - See Handbook NHB 2200.2.

NTIS - Leave blank.

Block 12b. Distribution Code.

DOD - Leave blank.

DOE - Enter DOE distribution categories from the Standard Distribution for Unclassified Scientific and Technical Reports.

NASA - Leave blank.

NTIS - Leave blank.

Block 13. Abstract. Include a brief (*Maximum 200 words*) factual summary of the most significant information contained in the report.

Block 14. Subject Terms. Keywords or phrases identifying major subjects in the report.

Block 15. Number of Pages. Enter the total number of pages.

Block 16. Price Code. Enter appropriate price code (*NTIS only*).

Blocks 17. - 19. Security Classifications. Self-explanatory. Enter U.S. Security Classification in accordance with U.S. Security Regulations (i.e., UNCLASSIFIED). If form contains classified information, stamp classification on the top and bottom of the page.

Block 20. Limitation of Abstract. This block must be completed to assign a limitation to the abstract. Enter either UL (unlimited) or SAR (same as report). An entry in this block is necessary if the abstract is to be limited. If blank, the abstract is assumed to be unlimited.

UTAH LOCAL AREA MODEL SENSITIVITY TO BOUNDARY
CONDITIONS FOR SUMMER RAIN SIMULATIONS

by

Steven Paul DeSordi

A thesis submitted to the faculty of
The University of Utah
in partial fulfillment of the requirements for the degree of

Master of Science

Department of Meteorology

The University of Utah

August 1996

19961212 046

Copyright © Steven Paul DeSordi 1996

All Rights Reserved

THE UNIVERSITY OF UTAH GRADUATE SCHOOL

SUPERVISORY COMMITTEE APPROVAL

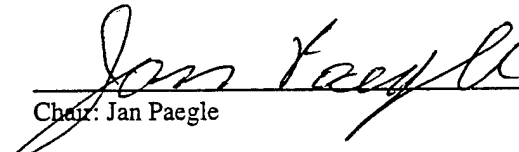
of a thesis submitted by

Steven Paul DeSordi

This thesis has been read by each member of the following supervisory committee and by majority vote has been found to be satisfactory.

May 31, 1996

Chair: Jan Paegle



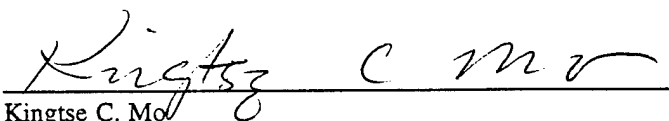
May 31, 1996

Julia Nogués-Paegle



May 31, 1996

Kingtse C. Mo



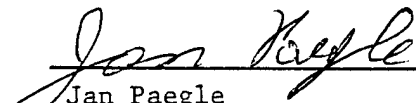
THE UNIVERSITY OF UTAH GRADUATE SCHOOL

FINAL READING APPROVAL

To the Graduate Council of the University of Utah:

I have read the thesis of Steven Paul DeSordi in its final form and have found that (1) its format, citations and bibliographic style are consistent and acceptable; (2) its illustrative materials including figures, tables and charts are in place; and (3) the final manuscript is satisfactory to the supervisory committee and is ready for submission to The Graduate School.

7 JUNE 1996
Date



Jan Paegle
Chair, Supervisory Committee

Approved for the Major Department



J.E. Geisler
Chair/Dean

Approved for the Graduate Council

Ann W. Hart
Dean of The Graduate School

ABSTRACT

The Utah Limited Area Model is integrated over a period of approximately 2 weeks during the summer floods that occurred in 1993 over the Upper Mississippi River Basin. The central goal is to determine the sensitivity of the simulated precipitation pattern to the method of specifying the upper and lateral boundary conditions. Three different upper boundary conditions are tested. The first does not allow feedback from the local model upon the pressure field at the model top. The second includes a modification of this field suggested by Klemp and Durran (1983) to allow vertical propagation of gravity waves through the model top. The third tested upper boundary condition specifies a pressure modification designed to eliminate w at the model top, as proposed by Innocentini et al. (1993). Model forecasts using the first two boundary conditions overpredict rainfall over Iowa, whereas the third simulation underpredicts the rainfall here and in most other regions. All simulations are poor with regard to heavy rain that was underpredicted southwest of Iowa where the NCEP reanalysis rainfall is relatively superior. Some of the limited area simulations are relatively better in the southeast portion of the country, where they provide more realistic rainfall structure than does the NCEP reanalysis. The limited area model predictions are also rather sensitive to the model used for boundary conditions. Boundary conditions interpolated from NGM model analyses and 6-h forecasts produce significantly more realistic regional Utah Limited Area Model simulations than boundary conditions interpolated from the NCEP reanalysis. There is relatively less sensitivity to the spectral relaxation of limited area forecasts to outer model results, although this did generate rainfall in some regions that were excessively dry. One experiment modifying the treatment of water vapor and relaxing the condition for condensation from 100% to 95%

relative humidity suggests that the relative influences of the water vapor treatment are about as large as those associated with boundary conditions. The experiments are generally in agreement with earlier simulations regarding the dominant role of atmospheric moisture transport for the 1993 summer floods.

TABLE OF CONTENTS

ABSTRACT	iv
ACKNOWLEDGMENTS.....	vii
Chapter	
1. INTRODUCTION.....	1
2. MODEL DESCRIPTION	5
Model Equations.....	5
Model Overview.....	8
Boundary Condition Specification	13
3. PRECIPITATION AND WIND ANALYSES	16
Precipitation Analysis.....	16
Low-Level Jet.....	25
4. UPPER BOUNDARY CONDITION SENSITIVITY.....	36
The $p' = 0$ Experiment	40
The K-D Experiment.....	47
The $w = 0$ Experiment.....	51
5. LATERAL BOUNDARY CONDITION SENSITIVITY	58
Lateral Boundary Data Origin.....	58
Lateral Boundary Implementation Method	66
Wave 0 Relaxation.....	69
Wave 1 Relaxation.....	77
Wave 2 Relaxation.....	85
6. ATMOSPHERIC WATER FLUXES	93
7. CONCLUSIONS	107
REFERENCES.....	110

ACKNOWLEDGMENTS

I would like to thank my advisor, Dr. Jan Paegle. He was instrumental in keeping this research focused and on track. Without his experience, expertise, and guidance this thesis could not have been completed. I would also like to thank my committee members, Dr. Kingtse C. Mo and Dr. Julia Nogués-Paegle for suggesting a number of ideas and useful recommendations during this research.

I would also like to extend special thanks to my wife, Janice, and my daughter, Lauren, for their understanding, patience, and support of my countless hours away from the home throughout the last 2 years.

This research used precipitation and reanalysis data sets provided by Dr. Mo and Dr. Nogués-Paegle and NGM archives provided by Dr. John Horel. Numerous simulations were performed on the workstations in the Department of Meteorology and on the IBM RISC/6000 workstation cluster at the Utah Supercomputing Institute.

This research was partially supported by National Science Foundation grant ATM9119433 and National Oceanographic and Atmospheric Administration grant NA56GP0175 to the University of Utah. In addition, my attendance at the University of Utah was supported by the U.S. Air Force, Air Force Institute of Technology (AFIT).

Finally, I would like to recognize all of the students, staff, and faculty in the Department of Meteorology for their help, encouragement, and friendship.

CHAPTER 1

INTRODUCTION

The sources of limited area model (LAM) predictive errors have been studied and prioritized by many previous investigators. The role of lateral boundary conditions has been given special emphasis in a series of recent studies using the Utah LAM and variable resolution models. Paegle and Vukicevic (1987) performed real-data experiments over Europe with the Utah LAM and found that the method of lateral boundary conditions specification was much more important than both random perturbations and substantial analysis differences of the initial state within the LAM.

Vukicevic and Paegle (1989) demonstrated relatively small roles for initial analysis uncertainty relative to boundary uncertainty in bounded, barotropic versions of the Utah variable resolution model in all cases that used domain size smaller than about 6000 km. Vukicevic (1989) and Vukicevic and Errico (1990) reached a similar conclusion using the MM4, which is an advanced, multilevel primitive equation LAM developed at Pennsylvania State University and the National Center for Atmospheric Research.

Yang (1992) and Paegle et al (1996) demonstrate that global-scale changes of the initial state are more critical to regional forecasts than are regional uncertainties of the initial state. The result is consistent with Thompson's (1957) and Lorenz's (1969) conclusion that slight initial uncertainties of the large-scale advecting wind field are more important error sources for subsequent smaller scale error evolution than are slight initial errors of the smaller scales themselves.

Waldron (1994) and Waldron et al. (1996) find that very short-range LAM forecasts (0-12 h) over domains on the order of 1000 km have a sensitivity to current outer model uncertainty that approximately matches the value added by the higher LAM resolution. The large sensitivity of the inner LAM forecasts to boundary conditions supplied by the outer model led Waldron et al. (1996) to more detailed investigations of optimal methods to impose outer model guidance within the LAM domain through relaxation of larger inner scales of the LAM toward states predicted by the outer model.

The relaxation is done in spectral space and therefore permits outer model solutions to affect the entire LAM forecast domain, rather than just in a thin region adjacent to the lateral boundaries (e.g., Davies nudging, 1976) as done in most other LAM studies. The justification for the approach is based upon the hypothesis that the larger inner scales of a LAM may be more accurately predicted by a global model than by a LAM which allows larger-scale advective influences to occur only through the lateral boundaries. Unfortunately, that study was unable to verify or repudiate this hypothesis in the single studied case.

A number of investigations of methods to implement lateral boundary conditions have been performed (e.g., Wurtele et al. 1971; Davies 1976; Perkey and Kreitzberg 1976; Waldron et al. 1996; and others). Relatively less attention has been paid to the specification of LAM upper boundary conditions. This may in part be because many past LAMs have been written in sigma coordinates founded upon pressure. Such an approach requires vertical integration of the continuity equation downward from a specified upper boundary value of vertical motion to obtain vertical motion at lower levels. A natural assumption is that the vertical motion is zero at the model top, because this is usually consistent with the boundary condition used by the global model or analysis that provides the initial and boundary state to the LAM.

The Utah LAM is founded upon terrain following coordinates based on height rather than pressure. This approach requires specification of perturbation pressure rather

than vertical motion at the model top (Ciliberti 1996, unpublished master's thesis draft). The analogue of the approach in pressure-based sigma coordinates would be to set the perturbation pressure equal to zero at the model top. Unlike the zero vertical motion specified at the upper boundary in pressure based sigma coordinates, this condition does not close the domain to vertical transports through the upper boundary.

Other boundary conditions for the model top have also been proposed. Klemp and Durran (1983) recommended specification of a pressure perturbation that would minimize reflection of upwardly propagating gravity waves at the model top and thereby reduce distortion of the gravity wave spectrum below that level. Ross and Orlanski (1981) and Innocentini et al. (1993) proposed upper boundary conditions that would close the domain vertically through imposition of zero vertical velocity at the model top.

Recently, Ciliberti (1996, unpublished master's thesis draft) adapted this type of boundary condition for the Utah LAM. She also demonstrated that this upper boundary condition filters out the most rapidly propagating gravity waves allowed by other upper boundary conditions and therefore allows larger model time steps and more efficient integrations. Paegle et al (1996) used a version of the Utah LAM that employs internal spectral relaxation and closed upper boundary conditions in a two-week simulation of the 1993 Mississippi River Basin floods of summer 1993.

The goal of the present thesis is to explore the sensitivity of the Utah LAM forecasts to the way that the lateral and upper boundary conditions are applied. The approach is different from most past studies of LAM boundary specification because it is founded upon a medium-range simulation using real data. Many other studies of boundary conditions have used idealized cases, or short-term (a few days or less) predictions. The principal benefits of the medium-range simulation is that boundary conditions should permeate the entire LAM domain on these time scales, and the verification would include a number of events rather than just a single short case study.

Chapter 2 presents a summary of the equations and numerical methods used by the Utah LAM. Chapter 3 describes the selected period of study. This period covers 13 days from 27 June to 9 July 1993, and the domain of interest is centered on the Mississippi River Basin. The interval includes several heavy rainfall events, which are illustrated by station precipitation summaries, objective analyses of these data, and reanalyses of precipitation as given by the Reanalysis Project at the National Centers for Environmental Prediction (NCEP, Kalnay et al. 1996). Strong nocturnal low-level jets characterized this period, and rainfall tended to be especially heavy at night as summarized in Chapter 3.

The Utah LAM is initialized and bounded with NCEP analyses and forecasts imposed at the model boundaries in different ways in order to study model forecast sensitivity to specification of upper and lateral boundaries. Chapter 4 outlines the background analysis leading to the $p' = 0$ upper boundary condition, the Klemp-Durran (1983) upper boundary condition, and the Innocentini et al. (1993) closed upper boundary condition. Precipitation and low-level jet simulations produced by the Utah LAM using each of these upper boundary conditions are also presented.

Chapter 5 explores the sensitivity of the Utah LAM rainfall simulations to the type of boundary data and the effect of spectral nudging upon the resulting simulations. Chapter 6 describes water budgets, and conclusions are summarized in Chapter 7.

CHAPTER 2

MODEL DESCRIPTION

The earliest version of the Utah LAM is described by Paegle and McLawhorn (1983). Various enhancements have been examined and implemented over the years, many of these are discussed by Waldron (1994). Of particular interest is the choice of upper boundary condition, the type of lateral boundary condition and its application method, and several precipitation processes. This chapter will highlight the model equations, overview model physics and parameters, and discuss boundary condition specifications.

Model Equations

The most recent summaries of the Utah LAM are provided by Paegle et al. (1996) and Waldron et al. (1996). The following summarizes those descriptions.

The model is based upon the following hydrostatic, anelastic set of equations using a terrain following height coordinate:

$$\begin{aligned} \frac{\partial u}{\partial t} + \frac{u}{r \cos \phi} \frac{\partial u}{\partial \lambda} + \frac{v}{r} \frac{\partial u}{\partial \phi} + w \frac{\partial u}{\partial z} - fv - \frac{uv}{r} \tan \phi \\ = -\frac{1}{\rho_s r \cos \phi} \frac{\partial p'}{\partial \lambda} - \frac{\rho'}{\rho_s} \frac{g}{r \cos \phi} \frac{\partial Z_t}{\partial \lambda} + F_u, \end{aligned} \quad (2.1)$$

$$\begin{aligned}
& \frac{\partial v}{\partial t} + \frac{u}{r \cos \phi} \frac{\partial v}{\partial \lambda} + \frac{v}{r} \frac{\partial v}{\partial \phi} + w \frac{\partial v}{\partial z} + fu - \frac{u^2}{r} \tan \phi \\
& = -\frac{1}{\rho_s r} \frac{\partial p'}{\partial \phi} - \frac{\rho'}{\rho_s} \frac{g}{r} \frac{\partial Z_T}{\partial \phi} + F_v,
\end{aligned} \tag{2.2}$$

$$\frac{\partial \theta}{\partial t} + \frac{u}{r \cos \phi} \frac{\partial \theta}{\partial \lambda} + \frac{v}{r} \frac{\partial \theta}{\partial \phi} + w \frac{\partial \theta}{\partial z} = F_\theta + H, \tag{2.3}$$

$$\frac{\partial p'}{\partial z} = -\rho' g, \tag{2.4}$$

$$\frac{\partial(\rho_s w)}{\partial z} = -\left[\frac{1}{r \cos \phi} \frac{\partial(\rho_s u)}{\partial \lambda} + \frac{1}{r} \frac{\partial(\rho_s v \cos \phi)}{\partial \phi} \right], \tag{2.5}$$

$$p' = \rho_s RT' + \rho' RT_s + \rho' RT'. \tag{2.6}$$

Here u , v , and w are the zonal, meridional, and vertical wind components, respectively. The atmosphere density ($\rho = \rho_s + \rho'$) and pressure ($p = p_s + p'$) have been decomposed into basic state (subscript s) and deviations (primes) as described by Paegle and McLawhorn (1983), g represents the gravitational acceleration, Z_T the terrain height, f is the Coriolis parameter, and θ potential temperature, where

$$\theta = T \left(\frac{P_0}{p} \right)^{\frac{R}{C_p}}. \tag{2.7}$$

Here P_0 is reference pressure (1013.25 mb), R is the atmospheric gas constant, C_p is the specific heat of dry air at constant pressure, and t , λ , ϕ , and z are time,

longitude, latitude, and height, respectively, while H in (2.3) represents heating. The friction terms F_u , F_v , and conduction F_θ are expressed as

$$F_u = \nabla_h (K_h \nabla u) + \frac{\partial}{\partial z} \left(K_z \frac{\partial u}{\partial z} \right), \quad (2.8)$$

with similar forms for F_v and F_θ (only the deviation, θ' , is diffused horizontally in the expression for F_θ , in the thermodynamic equation 2.3). K_h and K_z are the horizontal and vertical turbulence conductivities, and ∇_h is the horizontal gradient operator. The horizontal diffusion coefficient, K_h , is defined as

$$K_h = \alpha(\Delta S)^2 \left[\left(\frac{\partial u}{\partial x} + \frac{\partial v}{\partial y} \right)^2 + \left(\frac{\partial u}{\partial y} + \frac{\partial v}{\partial x} \right)^2 \right]^{\frac{1}{2}}, \quad (2.9)$$

where ΔS is the grid interval and α is a constant ($\alpha=0.36$ except when specified otherwise). The definition of vertical diffusion coefficient K_z follows Yamada and Bunker (1989) (see Waldron 1994). The equation governing specific humidity q is

$$\frac{\partial q}{\partial t} + \frac{u}{r \cos \phi} \frac{\partial q}{\partial \lambda} + \frac{v}{r} \frac{\partial q}{\partial \phi} + w \frac{\partial q}{\partial z} = F_q - P + E_a, \quad (2.10)$$

where F_q represents turbulent diffusion, P is condensation rate, and E_a is the evaporation rate in the atmosphere.

Model Overview

Table 2.1 summarizes the model overview provided below. The Utah LAM predicts turbulent kinetic energy and retains solar and longwave radiative heating of the atmosphere and surface, including cloud radiation interactions. Turbulence parameterization is detailed by Waldron (1994) and is based on the method used by Yamada and Bunker (1989). The amount of solar radiation reaching the surface is computed at each grid point, based on the time of day, day of year, latitude, and longitude, with an albedo of 0.3. Solar radiation also includes parameterizations for clear air scattering according to Kondratyev (1969) and attenuation due to clouds from no more than four cloud layers (high, middle, low, and surface) adapted from the Norwegian Model

Table 2.1 Utah Lam Overview

Domain	25°N to 57°N 78°W to 110°W
Resolution	0.5° x 0.5°
Topography Resolution	0.5° x 0.5°
Grid	65 x 65 points, non-staggered
Vertical Levels	17 atmospheric: surface, 1, 10, 100, 300, 500, 1000, 2000, 3000, 4000, 5500, 7000, 8500, 10 000, 11 500, 13 000, 14 500 (meters). 5 soil: surface, 0.05, 0.1, 0.15, 0.2 (meters).
Vertical Coordinate	terrain following, height based
Precipitation	convective: convective adjustment parametrization stable: grid box RH \geq 100% sub-cloud evaporation: yes
Turbulence Parameterization	Yamada and Bunker (1989)
Albedo	0.3

(Nordeng 1986). The longwave radiation budget, composed of fluxes from the atmosphere and the surface (both upward and downward), includes interactions with water vapor (Welch 1976) and carbon dioxide (Nordeng 1986). Solar radiation calculations are performed every time step; however, longwave fluxes are computed only once each hour, thus reducing computer time. This has been shown to be adequate for simulation of the boundary layer diurnal oscillation (Nicolini et al. 1993).

The prognostic equations are solved by finite difference quotient approximation in the horizontal and finite element method in the vertical. The model's terrain following coordinate has variable resolution, with higher resolution in the boundary layer. There are 17 vertical levels, one at the surface, and the remaining levels are at 1, 10, 100, 300, 500, 1000, 2000, 3000, 4000, 5500, 7000, 8500, 10 000, 11 500, 13 000, and 14 500 m above the surface. Soil temperature is also forecast on five equally spaced levels down to 0.2 m below the surface. The atmosphere and soil are coupled with a heat balance condition at the soil-atmosphere interface:

$$C_a \rho_a K_z \frac{\partial \theta}{\partial z} - C_s \rho_s K_s \frac{\partial T_{sub}}{\partial z} + G_r - F_n - \rho_w L_v E = 0, \quad (2.11)$$

where ρ_a , ρ_s , and ρ_w are air, soil, and water density, respectively, C_a and C_s are atmosphere and soil heat capacity, and K_s is soil conductivity. G_r is solar radiation and F_n is longwave radiation (considered positive for downward and upward flux, respectively), E is surface evaporation rate, and L_v is latent heat of vaporization. Table 2 of Paegle and McLawhorn (1983) provides values for the soil parameters ρ_s , C_s , K_s and roughness height.

Land and water surfaces are distinguished by their roughness height, specific heat, density, and conductivity. The conductivity of water is several orders of magnitude larger than that for soil. Surface evaporation is specified over land and water using estimates for

June 1993 obtained from the NCEP operational global analysis. There is no surface evaporation over land at night (e.g., Figure 11 of Sellers 1987). Over the ocean, the lower boundary condition on the specific humidity specifies $q = q_s$ (saturation value).

Convective and stable precipitation parameterizations are based on the National Center for Atmospheric Research (NCAR) Community Climate Model, CCM1 (Williamson et al. 1987). The convective parameterization engages in regions where two or more adjacent levels are supersaturated and the lapse rate is greater than the saturated adiabatic lapse rate. Once these regions are found, the convective adjustment relaxes the supersaturated atmosphere toward the moist adiabat, while preserving total moist energy. The explicit stable precipitation scheme reduces the model's specific humidity and increases its temperature at points that are supersaturated with stable stratification. Water in liquid and ice phase is not separately retained in the model. Evaporation of falling precipitation is allowed below cloud base until liquid disappears or relative humidity falls below 100%.

The horizontal latitude-longitude grid contains 65x65 points, spaced 0.5° in latitude by 0.5° in longitude with the southwest corner of the domain at 25°N , 110°W . Figure 2.1 shows the location of the gridpoints within the domain and Figure 2.2 shows the model topography. Variables forecast by the Utah LAM are carried on a nonstaggered grid. This has been shown to cause computational modes in space, and the common solution is to employ a staggered grid. The computational modes are observed to have wavelengths between two and four grid intervals, and these scales are removed with a Fourier filter applied at each time step. This is accomplished by calculating the deviation of the LAM predicted fields from the outer model forecast. Resulting fields are zero on the LAM boundaries, where values from the outer model are imposed. These periodic fields are projected onto Fourier series that are filtered as described by Waldron et al. (1996).

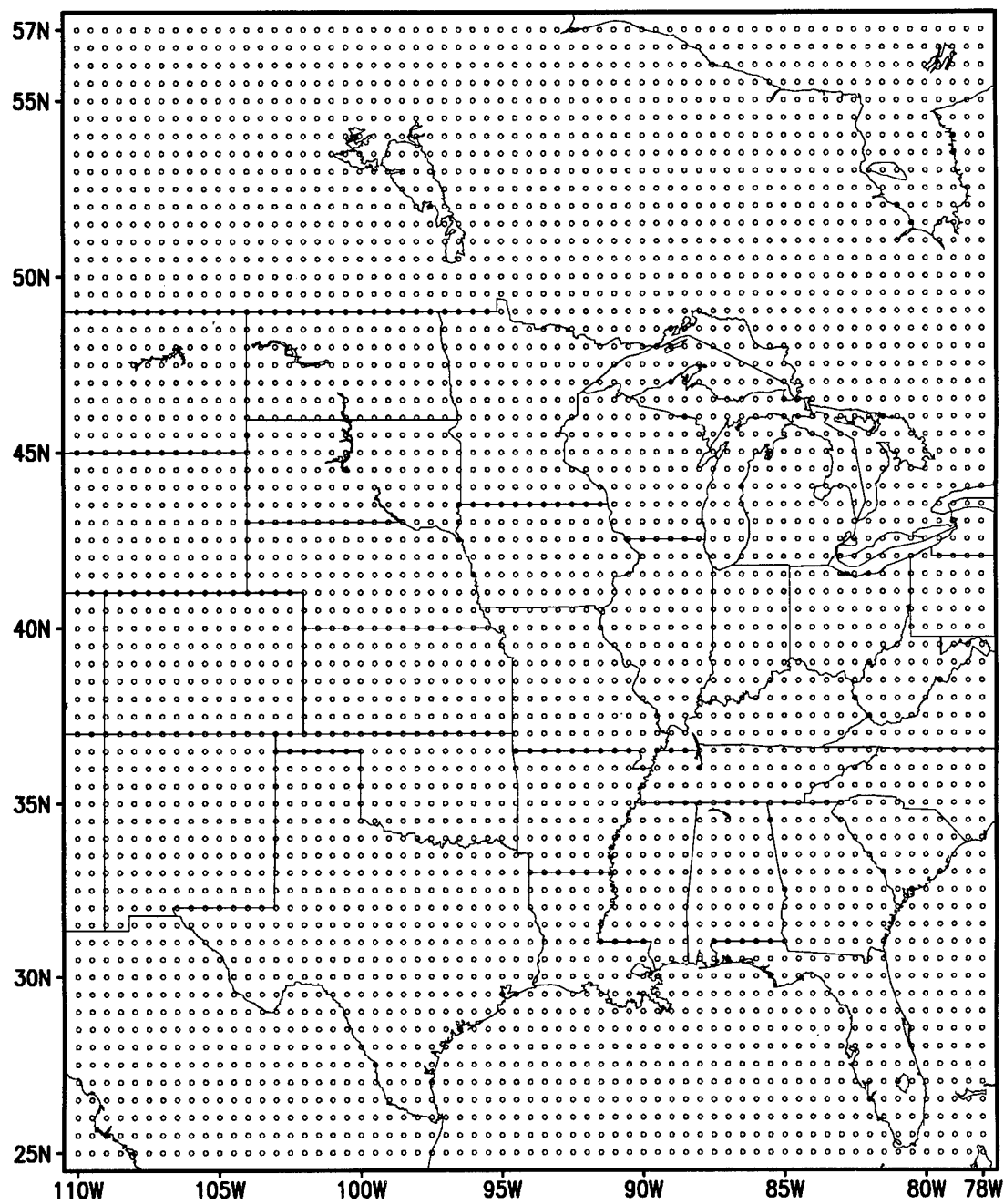


Figure 2.1. Utah LAM domain and gridpoint location.

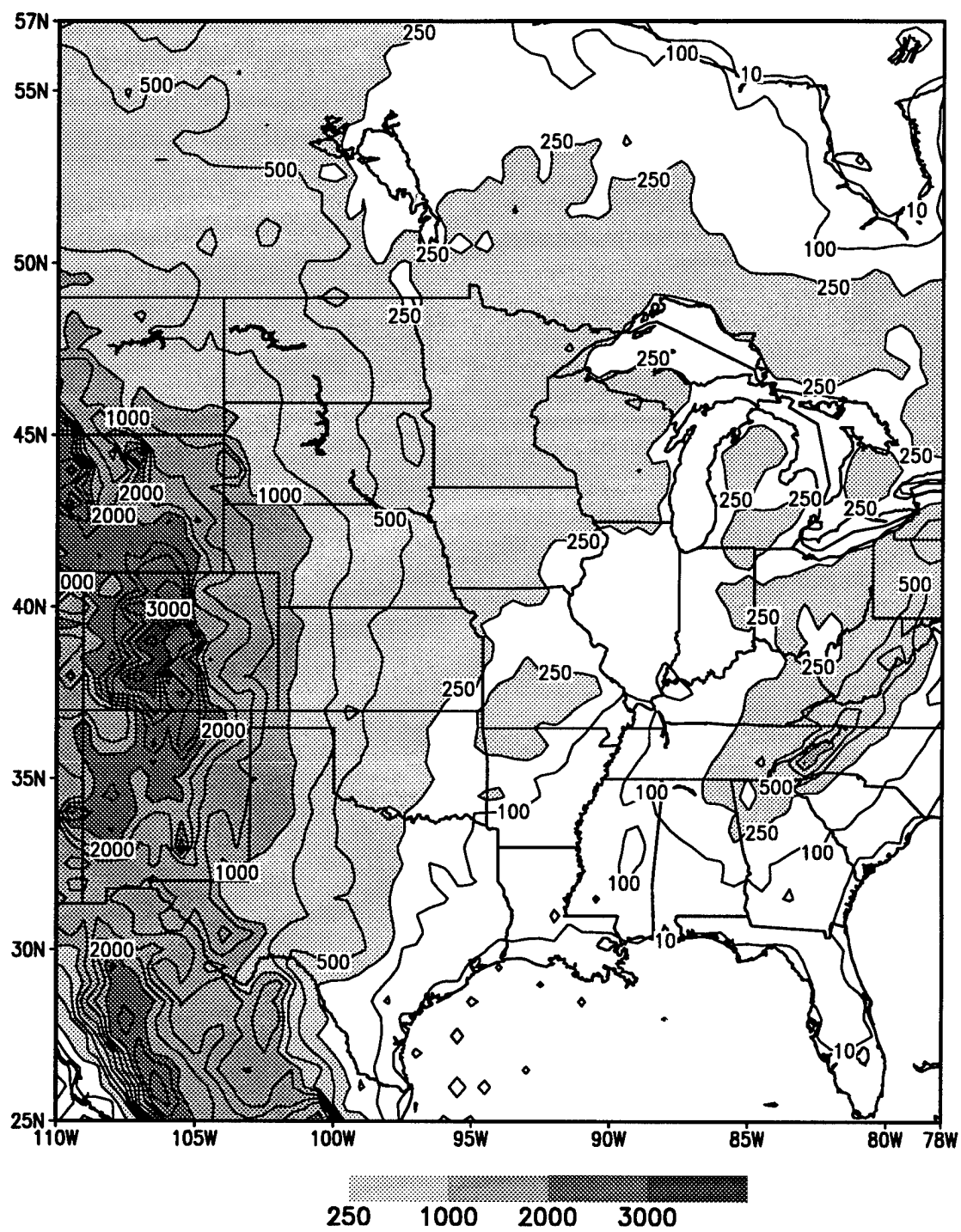


Figure 2.2. Utah LAM model topography. Contours are at 10, 100, and 250 m, then increments of 250 m up to 3500 m. Shaded values are 250, 1000, 2000, and 3000 m.

Boundary Condition Specification

The present goal is to use the model as a regional, high-resolution space and time interpolator for data extracted from large-scale outer model conditions supplied at 6 h intervals. Two different data sources were used as outer model input: the NCEP Nested Grid Model (NGM) on an 80 km by 80 km grid and the global reanalysis wavenumber 62 field on a 2.5° by 2.5° grid, as described by Kalnay et al. (1996). These outer model conditions are applied at the lateral and top boundaries of the LAM using Davies (1976) nudging in a thin layer (five grid points) adjacent to each lateral boundary. The boundary conditions are obtained from the outer model analyses/forecasts with a linear time interpolation to the time step of the local model and a cubic spline vertical interpolation to the local model levels.

The Utah LAM is relatively unique in the flexibility allowed for the specification of the lateral and upper boundary conditions. The effects of the outer model analysis/forecast, presently supplied by either NGM analyses/forecasts or by the global reanalysis fields, can be imposed upon the LAM either at the lateral boundaries or in spectral relaxation methods wherein the larger inner scales are rapidly relaxed toward the outer model (Waldron et al. 1996). The spectral relaxation can be selectively applied over any prespecified range of internal scales, for some or all of the forecast variables, and the rate of relaxation can be height dependent. The method in principle allows the inner model forecast field to evolve smoothly with the outer field, minimizing spurious gradients that may otherwise arise because of possible incompatibilities produced, for example, by different heating rates within the LAM domain than those resulting in the outer model over this region. Davies (1976, 1983) nudging is also included to blend the outer and inner model solutions over five grid columns adjacent to the lateral boundaries and is applied in all cases.

The sensitivity of the Utah LAM's forecasts to the degree of spectral relaxation has not been systematically investigated, particularly for longer term simulations, when both its impact and potential benefits may be greater. One of the present goals is to perform more

systematic tests of this method for the 13-day simulations of the 1993 Mississippi River Basin floods.

As noted earlier, the Utah LAM assumes hydrostatic and anelastic forms of the vertical momentum and continuity equations, (2.4) and (2.5), respectively. The pressure perturbation, p' , is computed from the integral of the hydrostatic equation from the top down,

$$p'(z) = p'(z_{top}) + \int_{z_{top}}^z g\rho' dz, \quad (2.12)$$

which requires an upper boundary condition on p' . Similarly, the vertical velocity, w , can be obtained by integrating the continuity equation, which requires a boundary condition either at the surface or the model top. This leads to the three upper boundary conditions described below.

The simplest upper boundary condition can be provided from the pressure values obtained from the outer model (NGM or reanalysis), leaving the pressure deviation produced by the LAM, p' , to be everywhere zero at the model top. This will be hereafter referred to as the $p' = 0$ upper boundary condition. Upper boundary values on p' can also be modified following the approach of Klemp and Durran (1983, hereafter referred to as the K-D upper boundary condition). The K-D upper boundary condition modifies the pressure field obtained from the outer model at the upper boundary to allow vertically propagating gravity waves generated within the LAM to pass freely through its top. This boundary condition modification depends upon the vertical velocity diagnosed at the model top.

Another type of upper boundary condition is suggested by Innocentini et al. (1993). Their approach is to produce a lid at the LAM top by modifying the pressure field obtained from the outer model in an amount required to cancel exactly the vertically integrated

horizontal divergence acceleration. This boundary condition effectively eliminates the vertical velocity at the model top and is subsequently referred to as the $w = 0$ upper boundary condition. The potential advantages to this method are that it produces effectively closed domains in the vertical and also retains only the more slowly propagating gravity waves, allowing larger time steps. The latter benefit and modifications of the method originally proposed by Innocentini et al. (1993) are discussed in more detail by Ciliberti (unpublished master's thesis draft).

The Utah LAM has options to include each of these upper boundary conditions, but they have not been systematically intercompared for precipitation forecasting on the space and time scales of interest to the 1993 flood simulations.

CHAPTER 3

PRECIPITATION AND WIND ANALYSES

Several data sources were used for model verification of forecast precipitation and the low-level jet. This chapter describes the 13-day total precipitation for the period 27 June to 9 July 1993. The 5 July was chosen to illustrate a day with particularly heavy precipitation. The diurnal variation of the precipitation is highlighted as well as the diurnal cycle of the low-level jet.

Precipitation Analysis

Precipitation is measured daily at many stations throughout the United States. The Climate Prediction Center (CPC) issues a Crop Bulletin consisting of 24-h rainfall totals recorded at individual locations scattered across the area of interest. These observations (hereafter referred to as station precipitation) provide the highest resolution and are analyzed in Figure 3.1. A second source of rainfall data is the CPC objectively analyzed hourly station reports (for the U.S.) interpolated to a $2.0^{\circ}\times2.5^{\circ}$ grid (Higgins et al. 1996). This is illustrated in Figure 3.2 and will be referred to as gridded station data. In addition, the NCEP provides a global reanalysis including precipitation (hereafter referred to as reanalysis precipitation) analyzed on a $2.5^{\circ}\times2.5^{\circ}$ grid (Figure 3.3).

Figure 3.1 shows the 13-day total and 5 July rainfall amounts according to the CPC station precipitation. The 5 July rainfall (Figure 3.1b) is a 24-h amount from 0000 LST to 2400 LST, and the 13-day total precipitation (Figure 3.1a) is the sum of all daily reports of 24-h rainfall for 27 June to 9 July. Contouring for this and all subsequent figures containing station data was accomplished with GrADS (Grid Analysis and Display System)

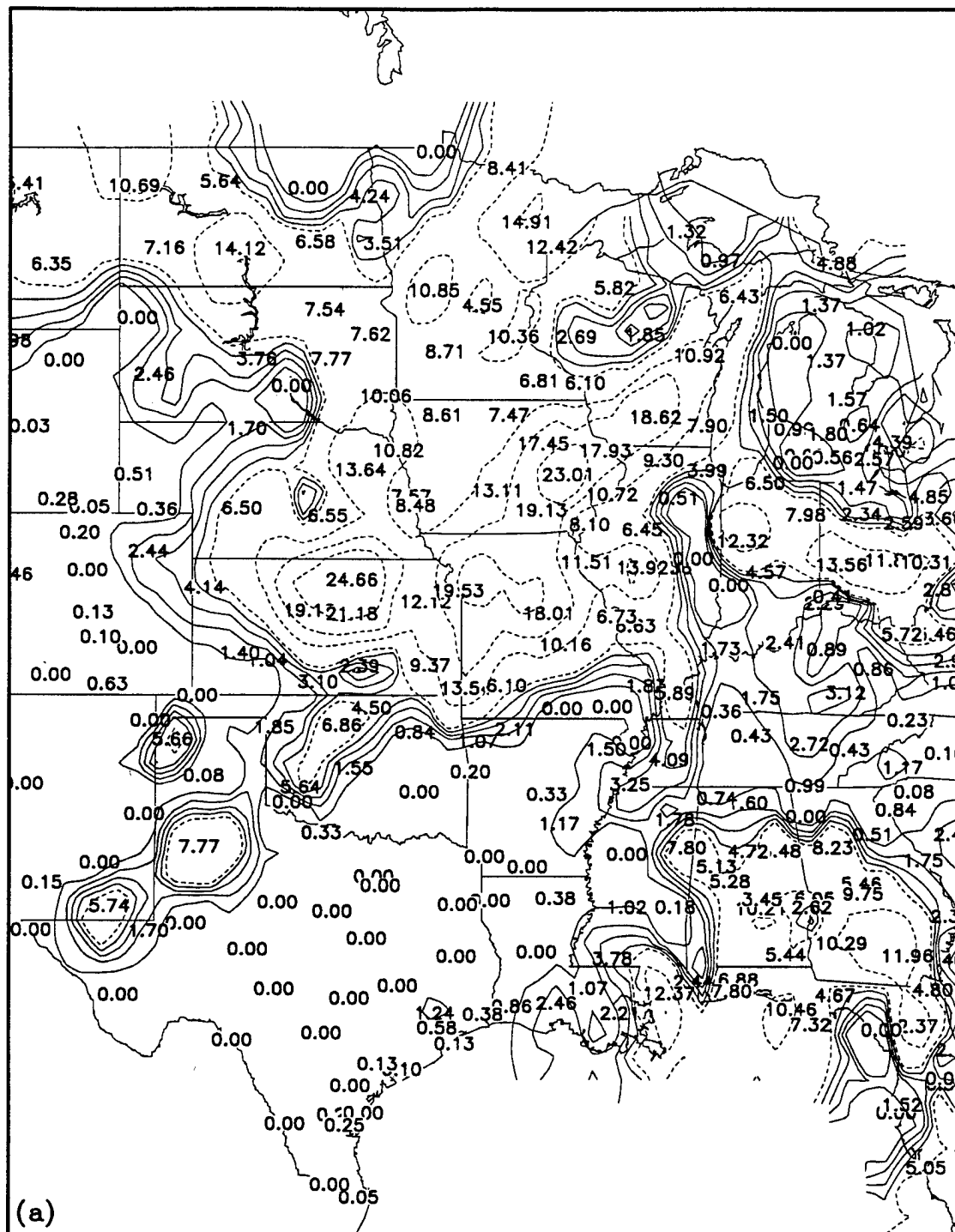


Figure 3.1. Precipitation from station data supplied by the CPC for (a) the 13-day period 27 June to 9 July 1993, and (b) the 24 h of 5 July 1993. Units are cm. In (a), the solid curves represent 1, 2, 3, and 4 cm and the dashed curves represent 5, 10, 15, and 20 cm. Both (a) and (b) were contoured with GrADS using a Cressman objective analysis interpolated to a 0.5° by 0.5° grid. In (b), the contours are dashed at 0.1 and 0.5 cm, solid at 1, 2, 3, and 4 cm, and dashed for 5 and 10 cm.

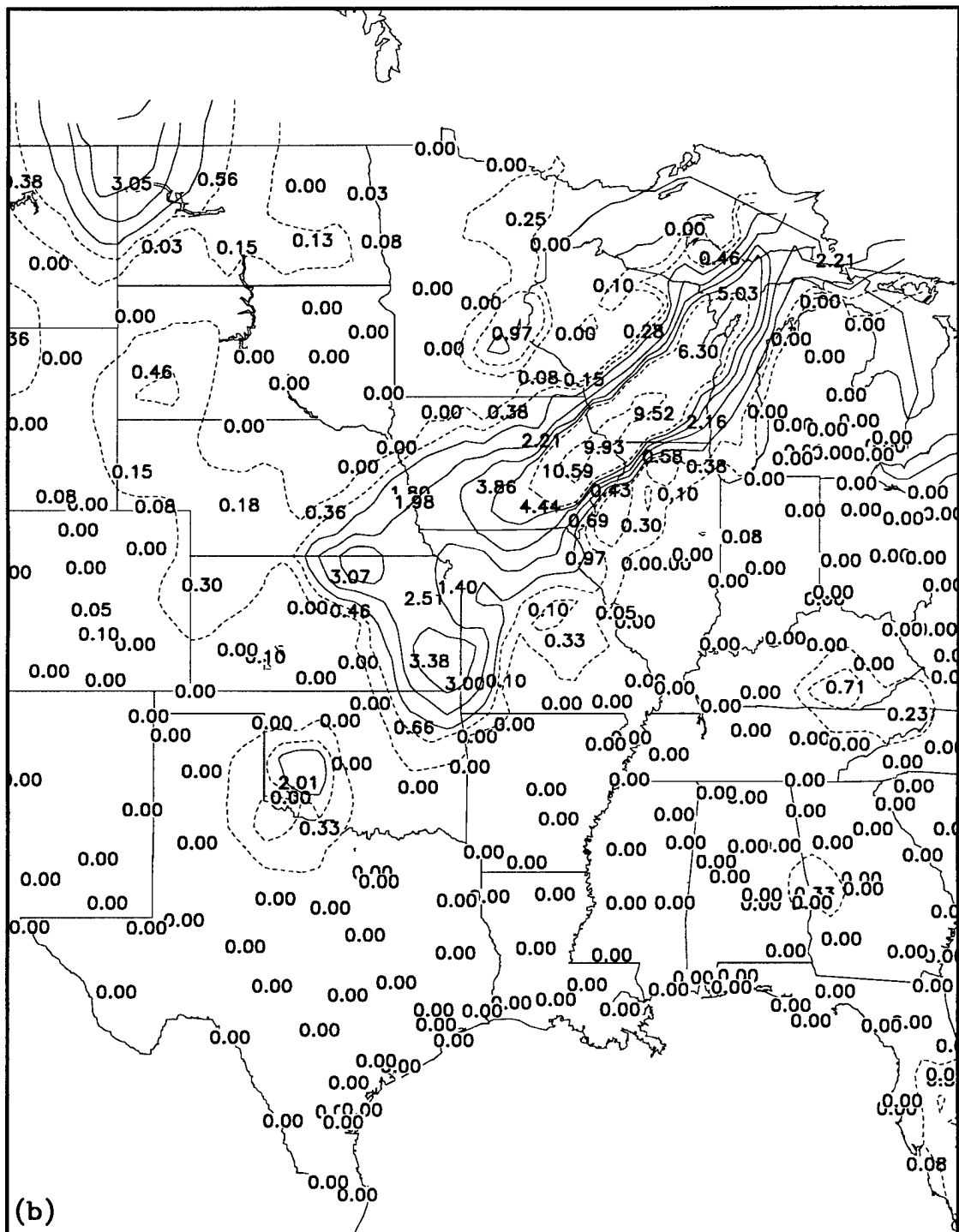


Figure 3.1. (Continued)

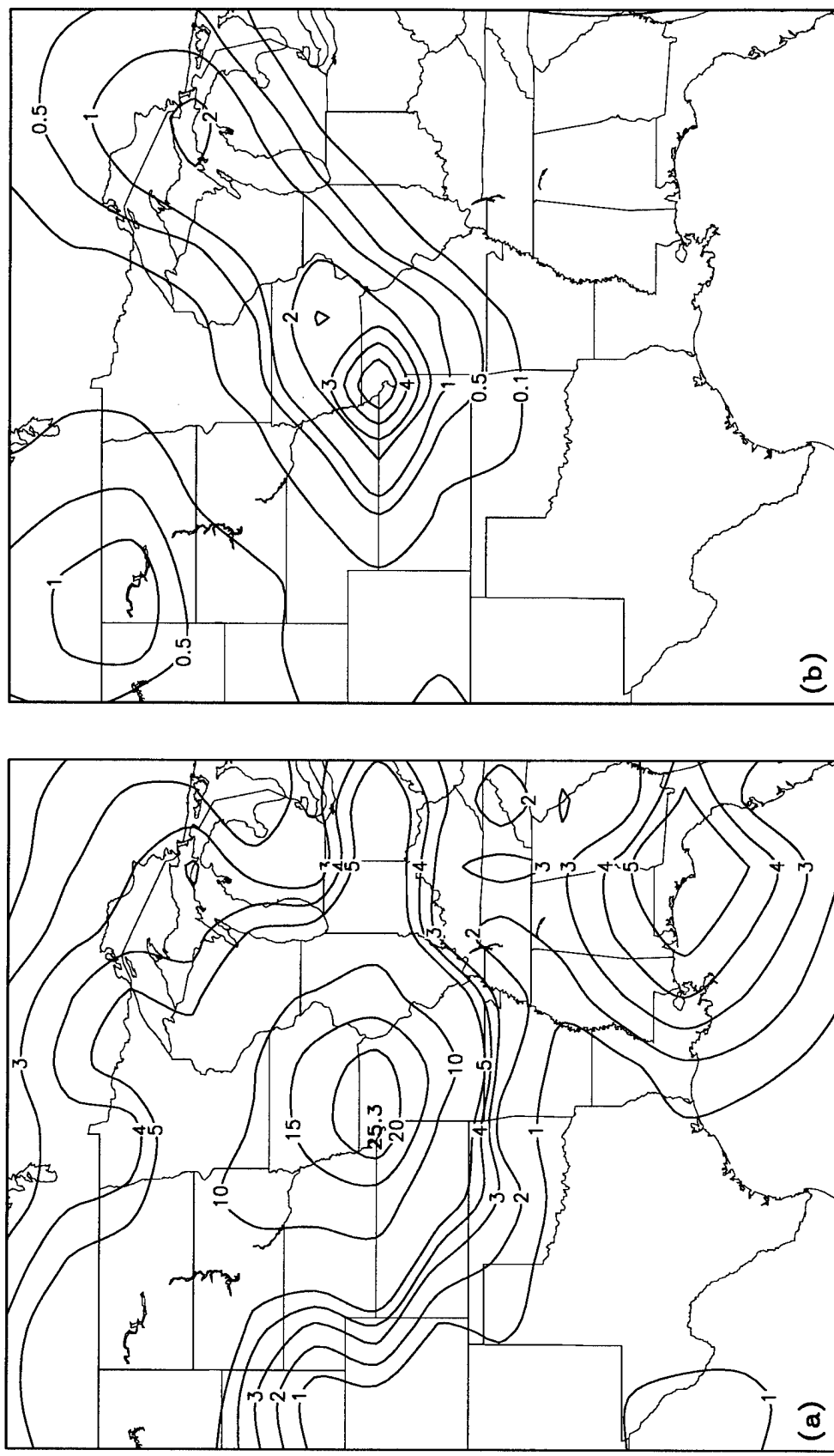


Figure 3.2. Precipitation from the CPC objectively analyzed hourly station reports interpolated to a 2.0° by 2.0° grid for (a) 27 June to 9 July 1993, and (b) 5 July 1993. Units are cm. Contours in (a) are at 1, 2, 3, 4, 5, 10, 15, and 20 cm, and in (b) at 0.1, 0.5, 1, 2, and 3 cm.

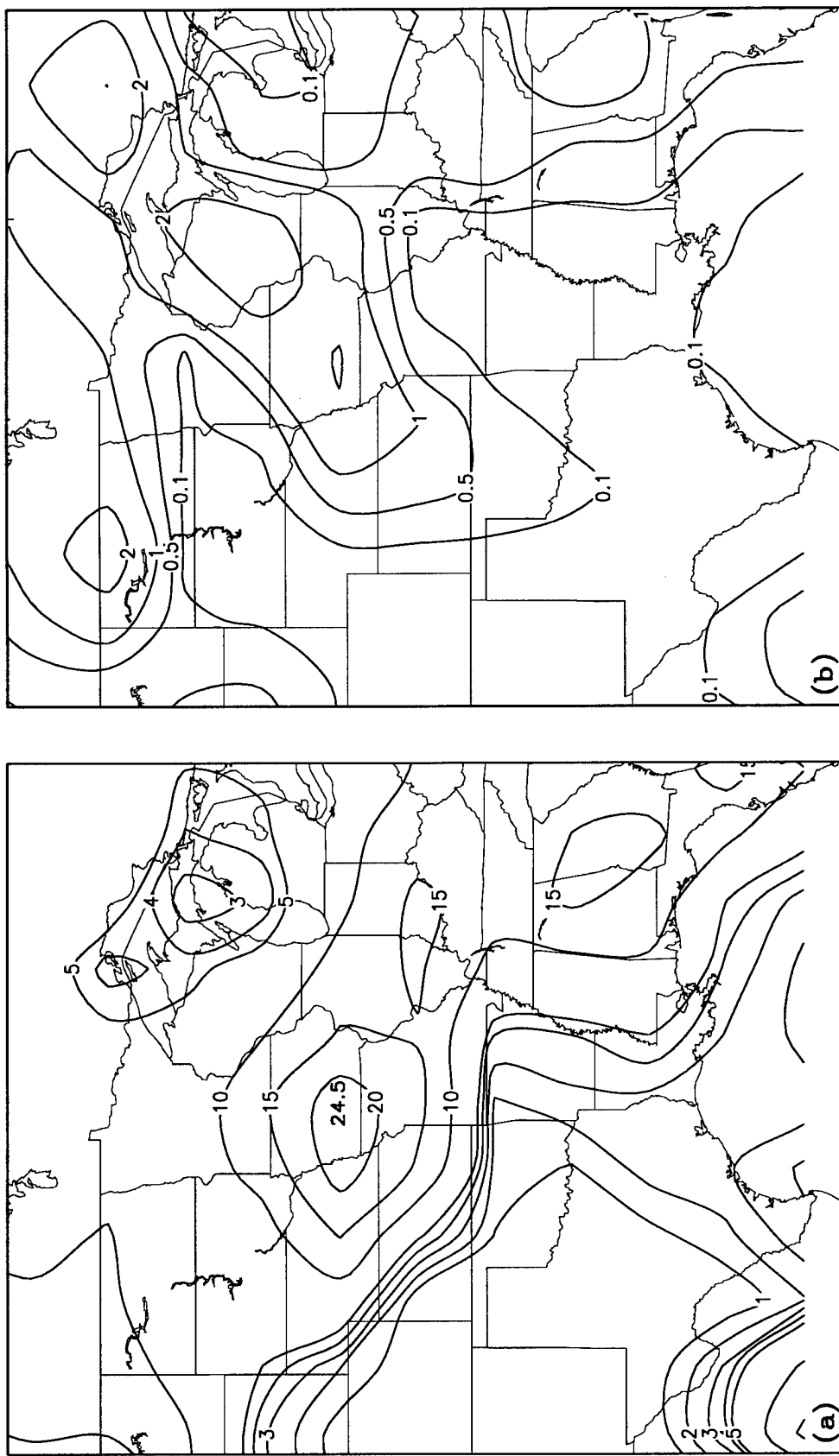


Figure 3.3. Precipitation obtained from the NCEP global reanalysis of daily precipitation rate on a 2.5° by 2.5° grid for (a) 27 June to 9 July 1993, and (b) 5 July 1993. Units are cm. Contours in (a) are at 1, 2, 3, 4, 5, 10, 15, and 20 cm, and in (b) at 0.1, 0.5, 1, 2, and 3 cm.

using a Cressman objective analysis interpolated to a 0.5° by 0.5° grid. The observation density of the station precipitation is better than the resolution of the two gridded data sources (CPC and NCEP), allowing for an improved depiction of the structure of the precipitation events. Although there is no reason to believe any of these data are unreliable, three stations were considered suspect and thus excluded: Lincoln, Nebraska (LNK, 40.85N 96.75W), Spickard, Missouri (P35, 40.25N 93.72W), and Fort Dodge, Iowa (FOD, 42.55N 92.18W). Lincoln reported only 0.89 cm from two days of rain when stations in all directions near Lincoln reported 8 to 11 days of precipitation. Spickard and Fort Dodge reported no rain in the 13-day period whereas neighboring stations reported 11 days of measurable rain.

Figure 3.2 is as Figure 3.1, but for the CPC-gridded station precipitation data. The grid point just north of Kansas City, Missouri, is the location of the 13-day maximum with a value of 25.3 cm (see Figure 3.2a). The general pattern in the Upper Mississippi River Basin is similar to that shown by the NCEP reanalysis precipitation (see Figure 3.3a); however the CPC-gridded station precipitation indicates a drier area through central Arkansas and east through Tennessee. On 5 July (Figure 3.2b) the precipitation was isolated to southeast Nebraska, Iowa, northeast Kansas, and northwest Missouri. In general, the CPC-gridded station precipitation shows 1 to 2 cm or greater over this four state area, with the maximum of 5.5 cm located at the grid point just north of Kansas City. This is less than indicated by the station precipitation shown in Figure 3.1b (especially in Wisconsin) and more than the NCEP reanalysis precipitation in Figure 3.3b. Since the CPC-gridded station precipitation was available with a temporal resolution of 1 h, it is used to illustrate the diurnal variation of precipitation later in this chapter.

The global reanalysis precipitation from NCEP is illustrated in Figure 3.3. This is based on the global model analysis of the available wind and temperature observations and does not include observed precipitation which is a model-predicted field (Kalnay et al. 1996 describes the NCEP reanalysis project). Because the resolution is relatively coarse, the

structure is smooth, as expected. The 13-day maximum of 24.5 cm (Figure 3.3a) is located at the grid point just southwest of Des Moines, Iowa, and there is a minimum over northern Lake Michigan. The reanalysis precipitation totals are too large in a broad region extending from southern Illinois into Georgia and Alabama. The reanalysis underestimated precipitation over portions of Texas and Oklahoma. Specifically for 5 July (Figure 3.3b), the reanalysis precipitation shows a significant lack of precipitation from east Kansas extending northeast into Wisconsin with amounts of 1 to 2 cm, less than the CPC-gridded station precipitation (Figure 3.2b), and much less than the station precipitation of Figure 3.1b.

In Figure 3.1a, there are three stations that reported 13-day rainfall totals greater than 20 cm: (1) Concordia, Kansas, 24.66 cm; (2) Cedar Rapids, Iowa, 23.01 cm; and (3) Salina, Kansas, 21.18 cm, and Kansas City, Missouri, had 19.53 cm. These stations cover a much larger area than indicated by the 20 cm contour in the CPC gridded station precipitation (Figure 3.2a) and the NCEP reanalysis precipitation (Figure 3.3a). Similarities include relatively drier conditions over much of Texas. Station precipitation indicates significantly greater rainfall north of the Ohio River than the gridded data sets, and the five stations reporting 5 cm or more in western Oklahoma, west Texas, and southeast New Mexico are not reflected in either of the gridded fields. On 5 July the station precipitation (Figure 3.1b) indicates a significant band of rainfall extending from eastern Iowa through southern and eastern Wisconsin with three stations reporting greater than 9.5 cm. The gridded CPC and NCEP data did not analyze this feature. In general, the detail in the station precipitation is much more representative of the mesoscale structure associated with the precipitation events over this 13-day period and on 5 July.

The CPC-gridded hourly station precipitation data are used to examine the diurnal variation in the precipitation. Figure 3.4a-d shows the 6-h total rainfall analyzed over the entire 13-day period, separated into time blocks for 0000 UTC to 0600 UTC, 0600 UTC to 1200 UTC, 1200 UTC to 1800 UTC, and 1800 UTC to 2400 UTC, respectively.

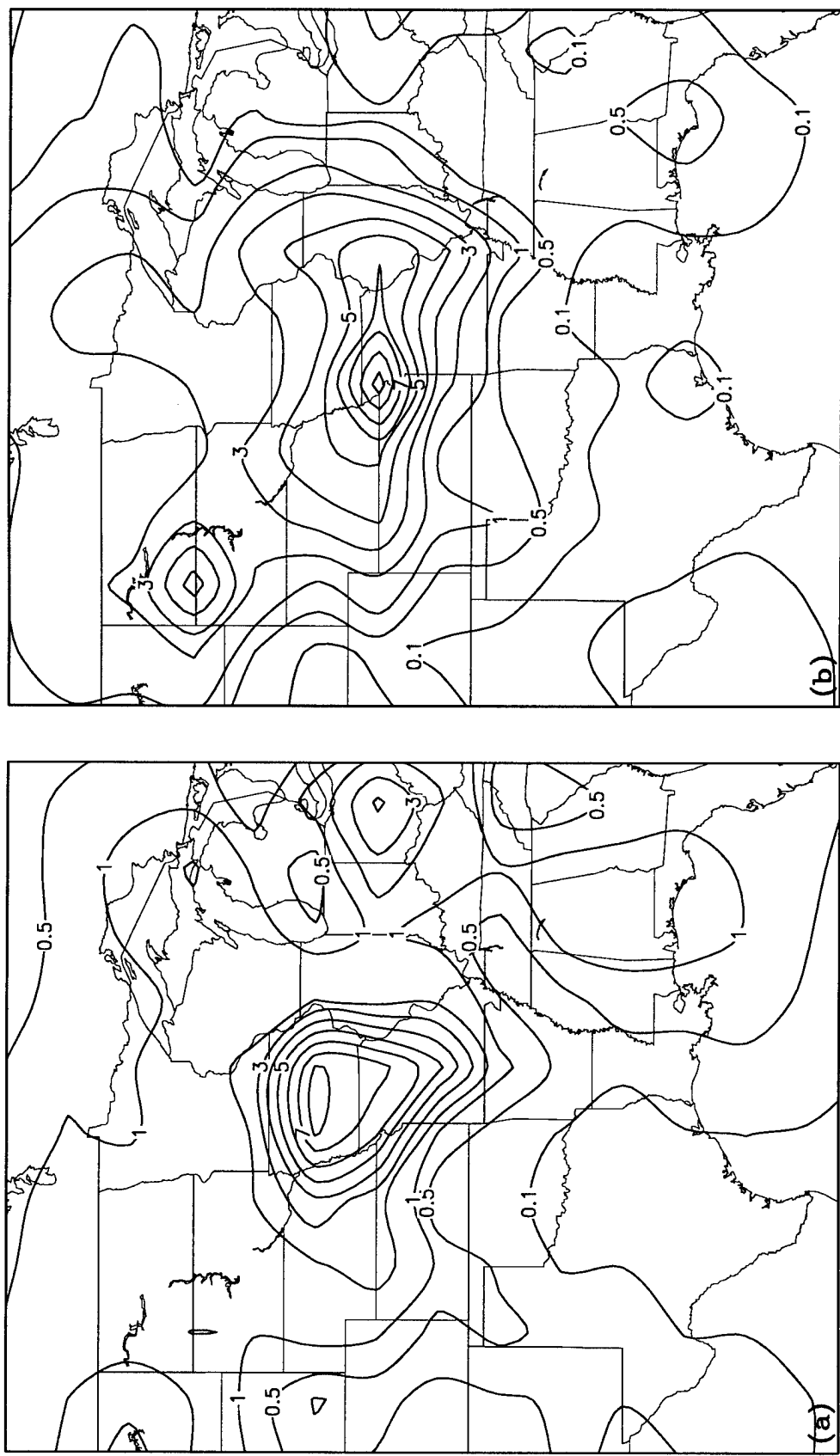


Figure 3.4. Total precipitation during four 6-h time blocks for the 13-day period 27 June to 9 July 1993, as analyzed by the CPC-gridded station precipitation. Each panel represents a different 6-h block: (a) 0000 to 0600 UTC, (b) 0600 to 1200 UTC, (c) 1200 to 1800 UTC, and (d) 1800 to 2400 UTC. Units are cm and the contour interval in all panels is 1 cm and the 0.5 cm contours.

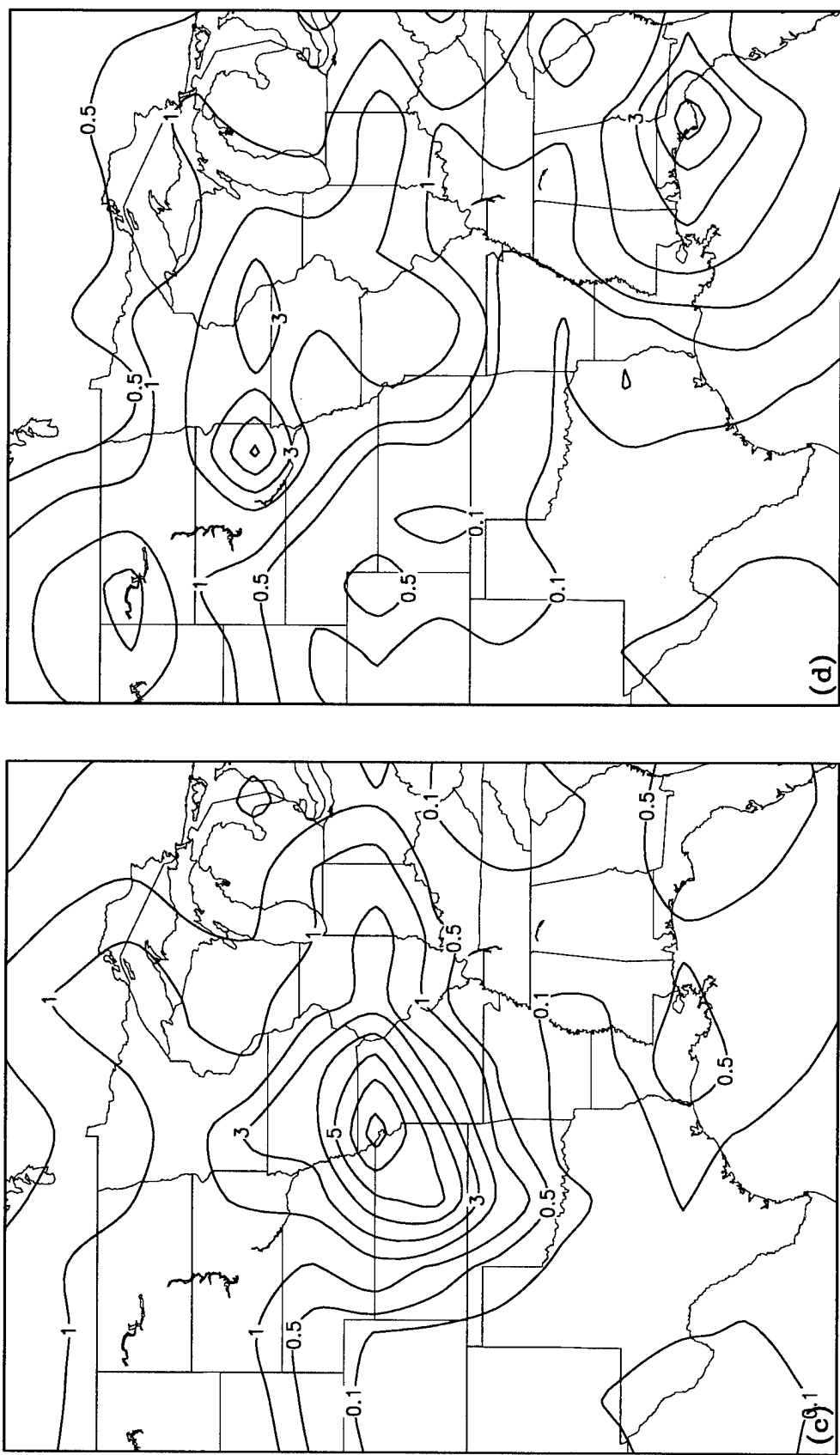


Figure 3.4. (Continued)

The local evening time block (0000 UTC to 0600 UTC, Figure 3.4a) illustrates a significant amount of rainfall in Iowa and north-central Missouri, with a maximum value of 8.19 cm in central Iowa. The 3-cm contour covers Iowa, western Illinois, most of Missouri, northeast Kansas, and eastern Nebraska. During the 0600 UTC to 1200 UTC period (Figure 3.4b), the maximum value is larger than during any other 6-h period with a 9.66 cm grid value north of Kansas City. Additionally, the 3-cm contour has expanded to encompass nearly all of Iowa, Missouri, and Illinois, as well as parts of Wisconsin, the Dakotas, Nebraska, and Kansas. There is a small secondary maximum of 5.78 cm along the eastern border of North Dakota and South Dakota. Rainfall amounts decline in the 1200 UTC to 1800 UTC period (Figure 3.4c), and a local maximum of 7.58 cm is again located north of Kansas City. The 3-cm contour has receded; however it now extends further to the southwest into Kansas. The least amount of rainfall was analyzed during the 1800 UTC to 2400 UTC period (Figure 3.4d). Aside from a small local maximum of 5.24 cm located in eastern South Dakota, the Upper Mississippi River Basin received little more than 2 cm during this 6-hour block over the entire 13 days.

Rainfall forecasting and verification are quite difficult due to meso scale features. Care must be taken in deciding what represents the best estimate of the truth. Of the three different sources of rainfall illustrated in this chapter, the 24-h station data and the CPC-gridded station data appear to be the best estimates. In addition, differences are larger for daily rainfall than for rainfall averaged over space or time, thus illustrating the uncertainty involved in precipitation forecasting and verification.

Low-Level Jet

The importance of the low-level jet (LLJ) and its influence on midwest nocturnal convection has been well documented (Blackadar 1957; Astling et al. 1985). Preliminary investigations of the LLJ concentrated on dynamical explanations based on diurnal oscillations of eddy diffusivity (Blackadar 1957) and buoyancy oscillations caused by the

diurnal heating of sloping terrain (Holton 1967). A discussion of the physical characteristics and structure of the LLJ was documented by Bonner et al. (1968), in which it is shown that the LLJ signature is evident below the 700-mb level (or 0.5 km to 2 km above ground). Additionally, Bonner et al. (1968) distinguished the LLJ as a transient synoptic scale southerly wind maximum of 23 to 34 m s^{-1} with a horizontal scale of approximately 300 km, best analyzed with the 1200 UTC sounding data.

The underlying motivation for analyzing the strength and diurnal variation of the LLJ lies in the aforementioned studies coupled with results of previous research with the Utah LAM. Paegle and McLawhorn (1983), Astling et al. (1985), and Nicolini et al. (1993) performed simulations showing the Utah LAM exhibits skill in forecasting the oscillation of the LLJ due to the enhanced resolution and the model's treatment of the physical parameters within the boundary layer that are key to the formation of this phenomenon. Furthermore, it has been shown by Mo et al. (1995) that the LLJ in the midwest United States was stronger than usual during the 1993 summer.

Panels a and b of Figure 3.5 display the 850-mb wind averaged for all 1200 UTC and 0000 UTC soundings, respectively, from 1200 UTC on 27 June to 0000 UTC on 10 July 1993. The sounding data were obtained from the Time Series RAOB Archive, Data Support Section, Scientific Computing Division, National Center for Atmospheric Research. A diurnal cycle is evident in the observations from Corpus Christi, Texas, north to Topeka, Kansas, where the winds are generally 9 to 13 m s^{-1} from the south at 0000 UTC, increasing to 13 to 19 m s^{-1} from the south through southwest at 1200 UTC. The diurnal oscillation composite shown in Figure 3.5 is not as strong as characterized by Bonner et al. (1968) since averaging tends to smooth out the signature by including days which did not synoptically support a strong LLJ. Figures 3.6a-d show a more typical example with winds of 33 and 29 m s^{-1} over Topeka at 1200 UTC on 4 and 5 July, respectively. In this case, 850-mb wind speeds in excess of 20 m s^{-1} are evident much further north than would be inferred from Figure 3.5b. The location of the heaviest

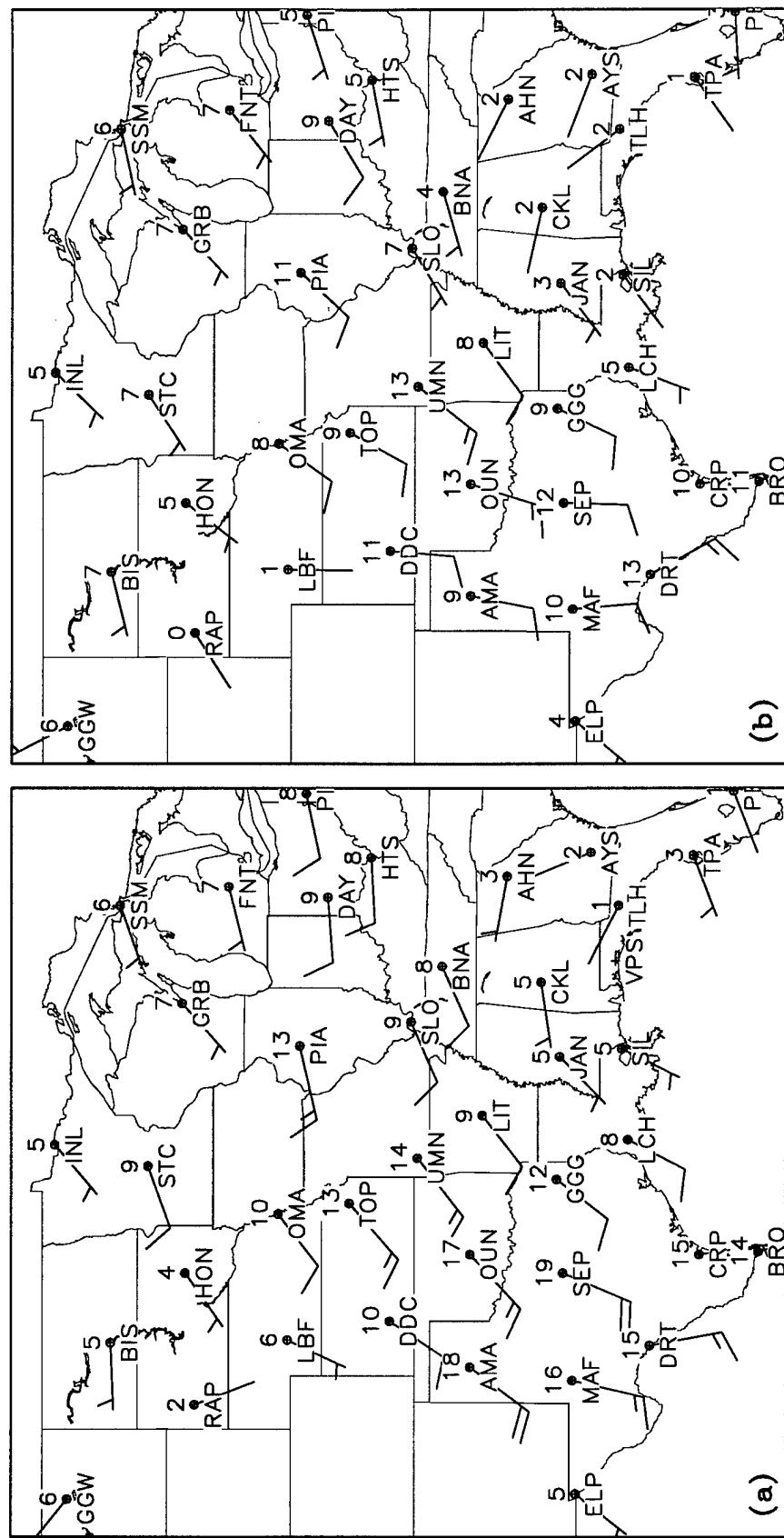


Figure 3.5. Vector average 850-mb wind using (a) all 1200 UTC soundings and (b) all 0000 UTC soundings from 1200 UTC 27 June to 0000 UTC 10 July 1993. Units are m s^{-1} , a full barb represents 10 m s^{-1} , a half barb is 5 m s^{-1} (barb values are rounded to the nearest full or half barb). The plots include the wind speed and the 3-letter station identifier.

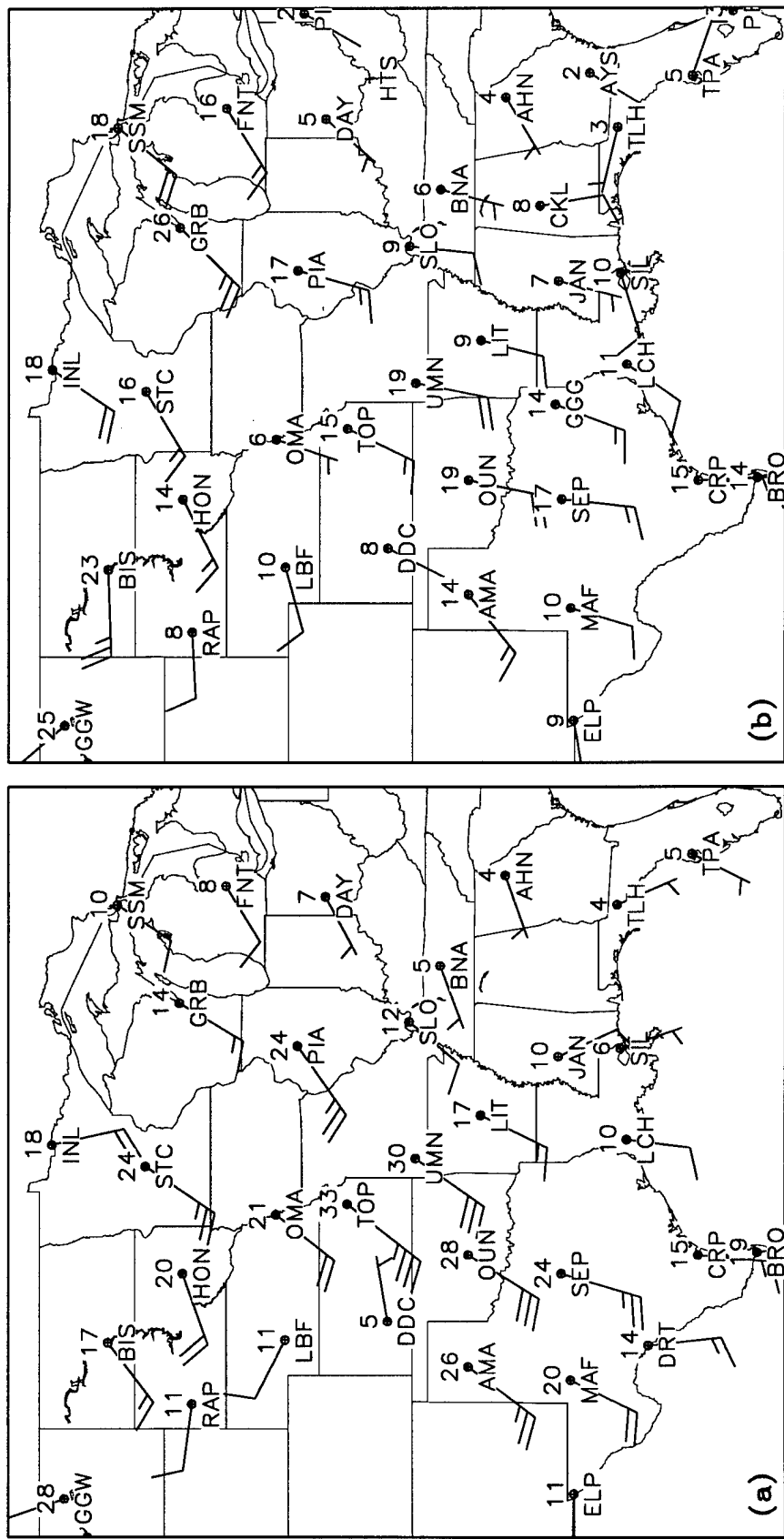


Figure 3.6. 850-mb wind from soundings taken at (a) 1200 UTC on 4 July, (b) 0000 UTC on 5 July, (c) 1200 UTC on 5 July, and (d) 0000 UTC on 6 July 1993. Units are m s^{-1} and full barbs represent 5 m s^{-1} , half barbs represent 10 m s^{-1} . The plots include the wind speed and the 3-letter station identifier.

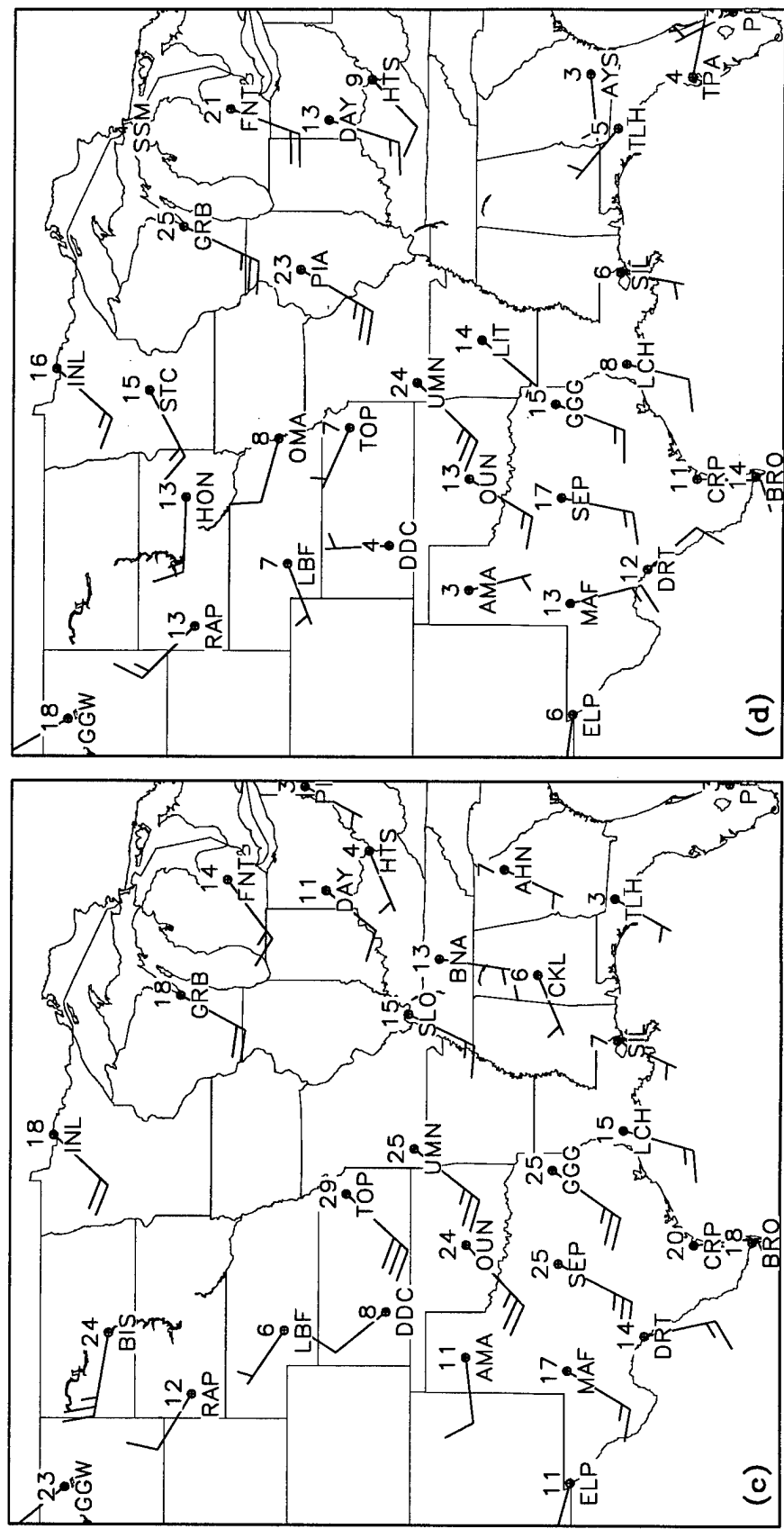


Figure 3.6. (Continued)

precipitation on 5 July (see Figure 3.1b) is well north in eastern Iowa and southern and eastern Wisconsin. Figure 3.7 is as Figure 3.5 but for 500 mb. It is included to show that the diurnal oscillation in the wind field is mainly a low-level feature and the signature is not evident at the 500-mb level.

Figures 3.8 and 3.9 display the 13-day average of the 850-mb wind at 0600, 1200, 1800, and 2400 UTC for the NGM and NCEP reanalysis models, respectively. The diurnal variation is similar and in agreement with the sounding data (Figure 3.5); however the reanalysis winds are slightly weaker.

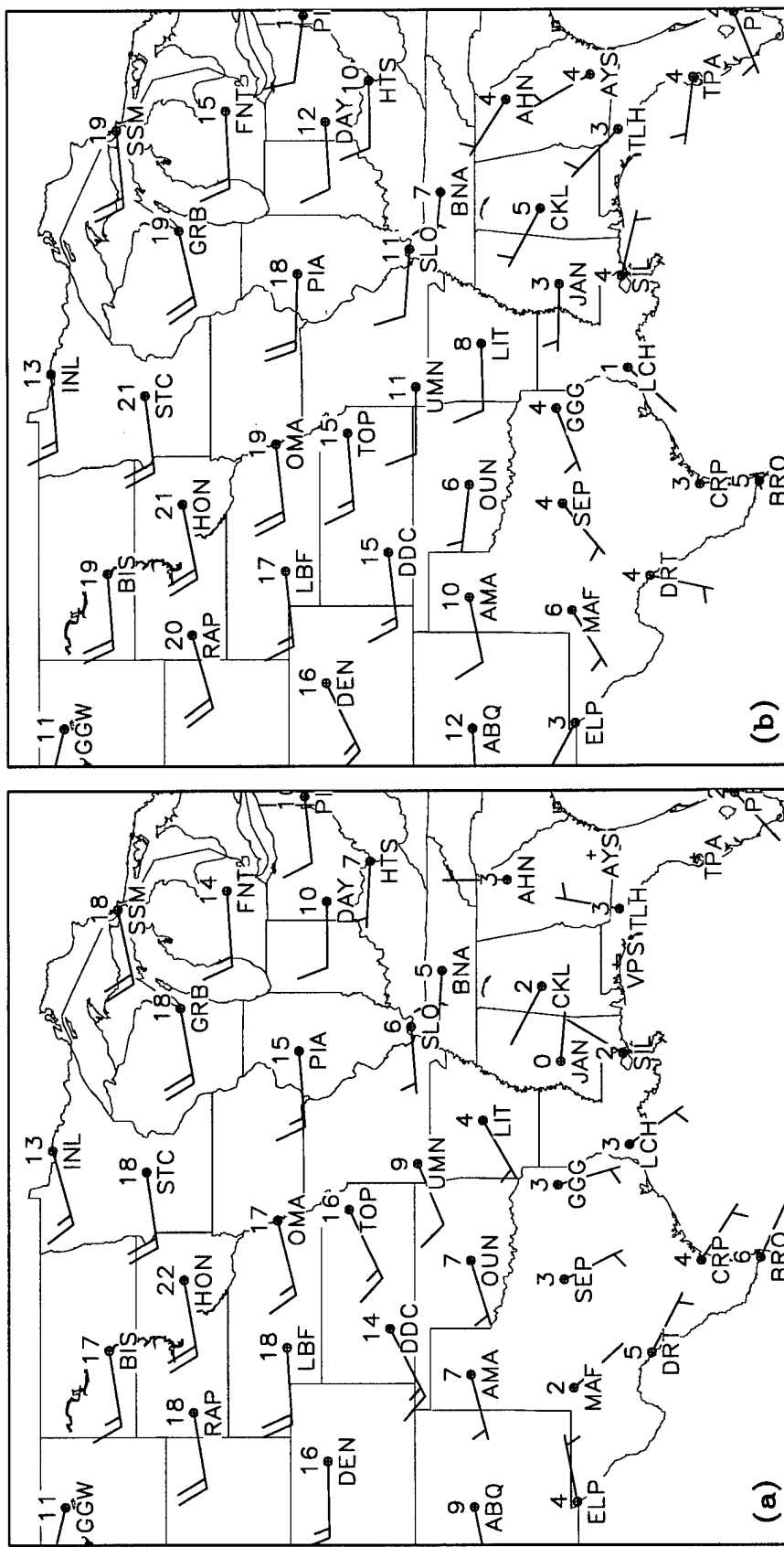


Figure 3.7. Vector average 500-mb wind using (a) all 1200 UTC soundings and (b) all 0000 UTC soundings from 1200 UTC 27 June to 0000 UTC 10 July 1993. Units are m s^{-1} and a full barb represents 10 m s^{-1} , a half barb is 5 m s^{-1} (barb values are rounded to the nearest full or half barb). The plots include the wind speed and the 3-letter station identifier.

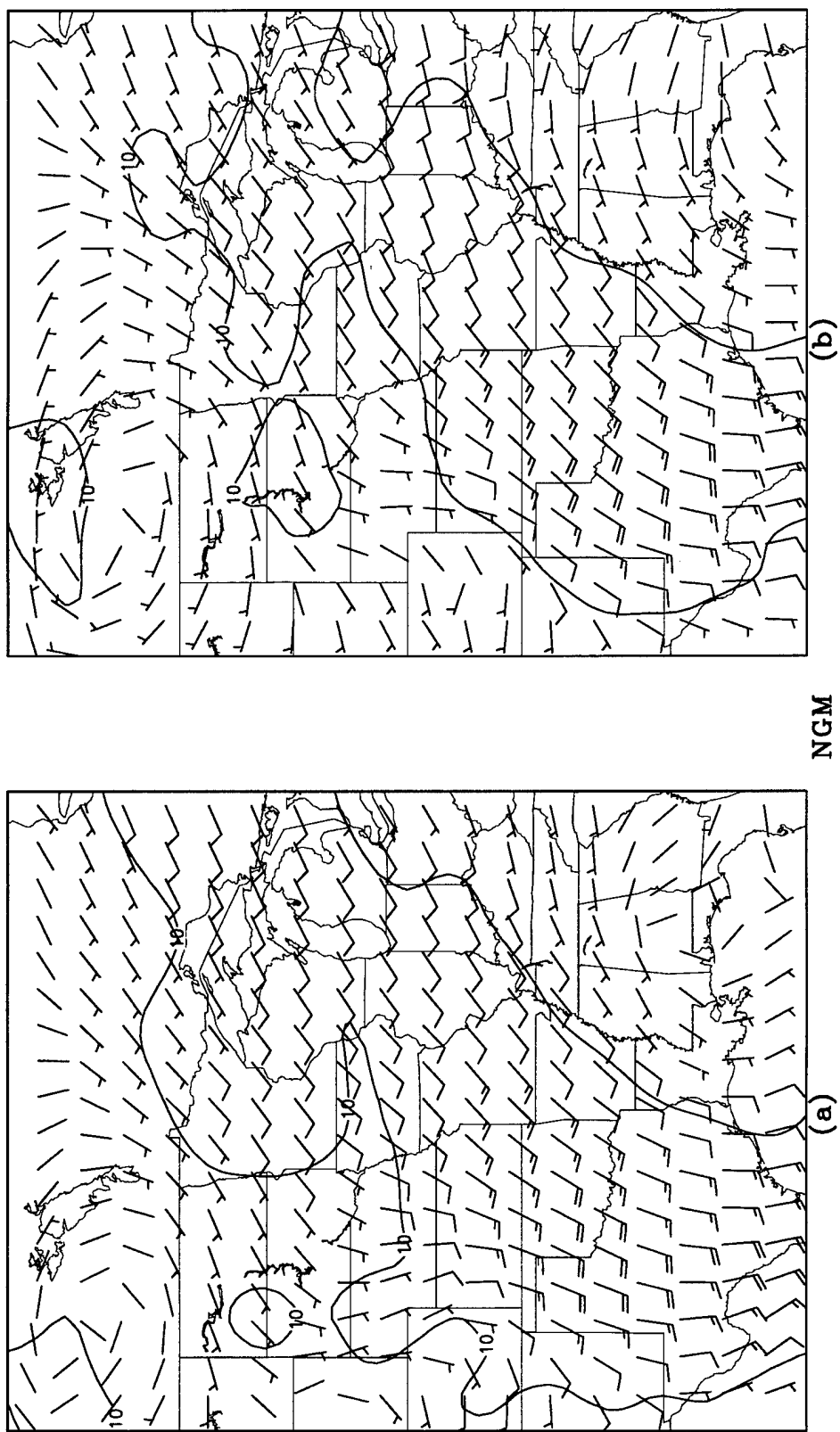


Figure 3.8. NGM 850-mb wind averaged at (a) 0600 UTC, (b) 1200 UTC, (c) 1800 UTC, and (d) 2400 UTC for the 13-day period 27 June to 9 July 1993. Units are m s^{-1} .

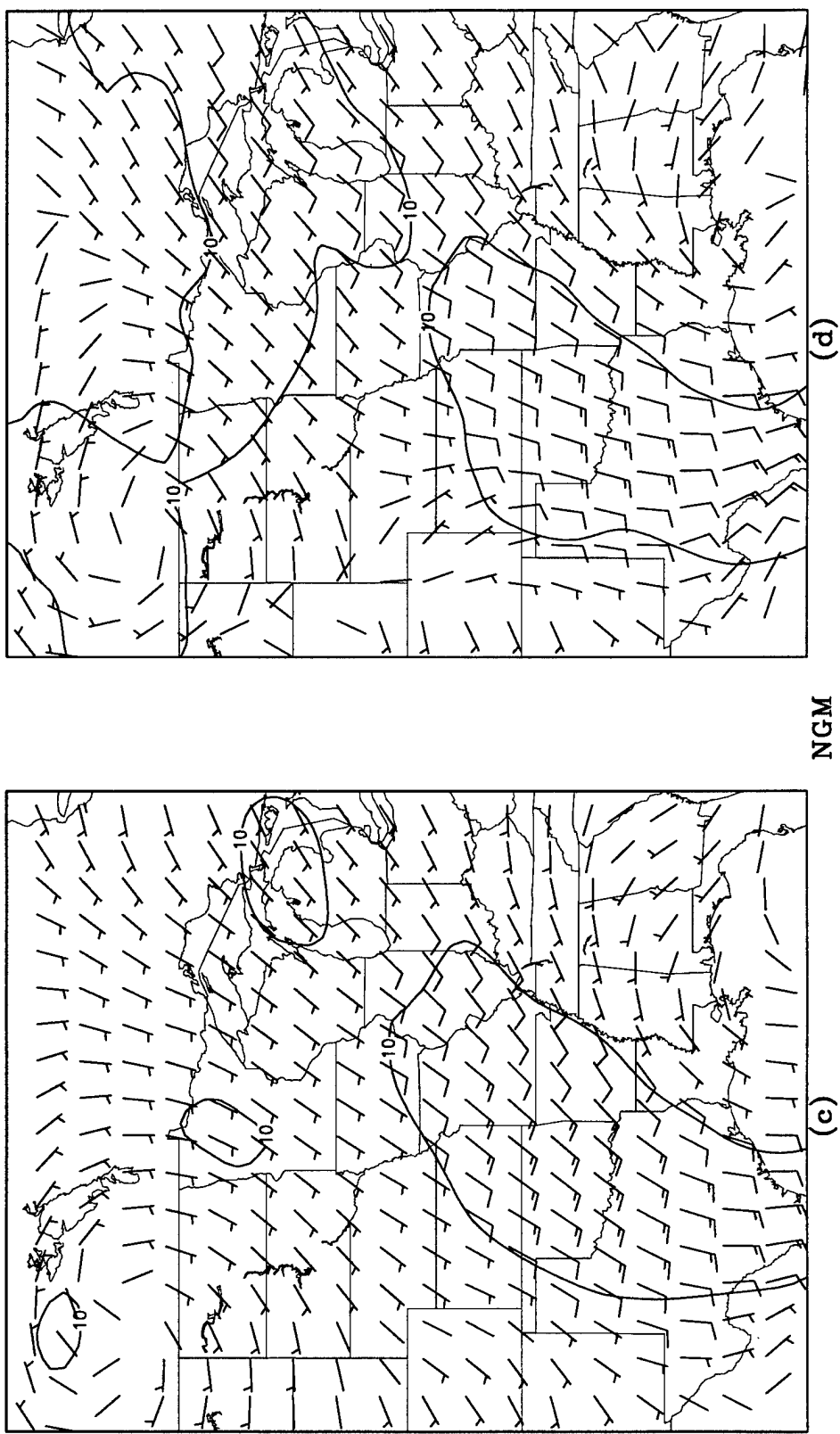


Figure 3.8. (Continued)

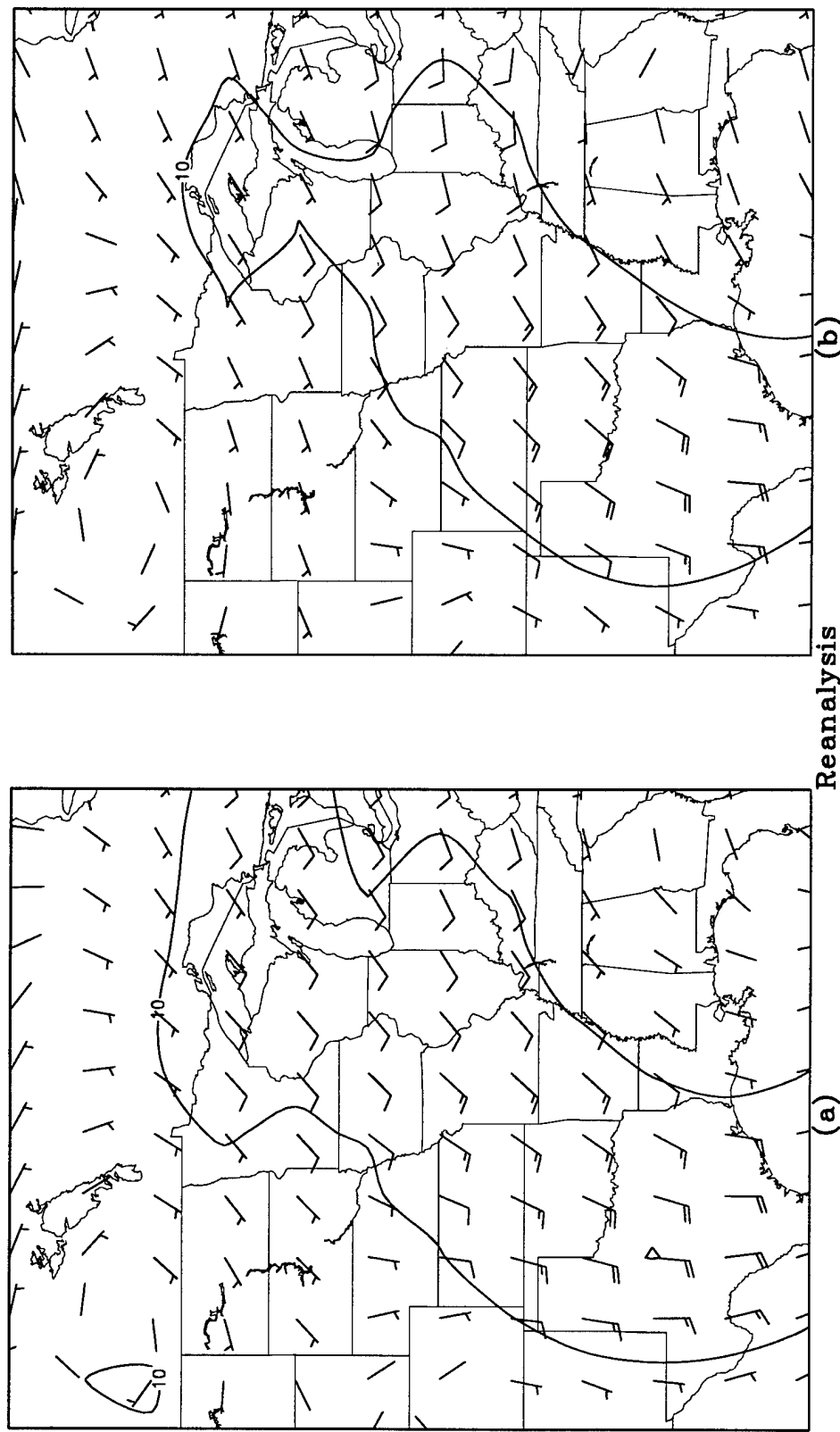


Figure 3.9. NCEP reanalysis 850-mb wind averaged at (a) 0600 UTC, (b) 1200 UTC, (c) 1800 UTC, and (d) 2400 UTC for the 13-day period 27 June to 9 July 1993. Units are m s^{-1} .

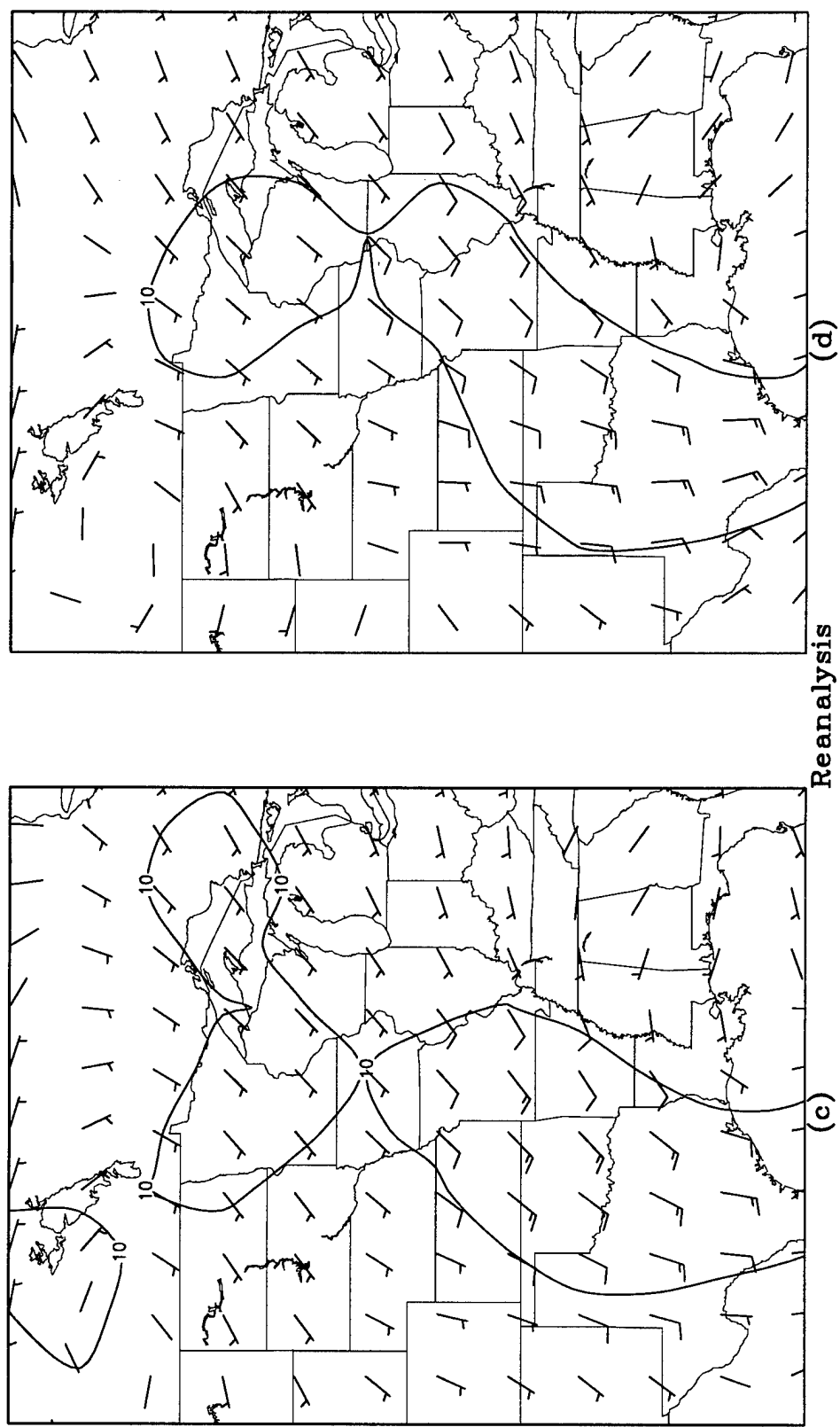


Figure 3.9. (Continued)

CHAPTER 4

UPPER BOUNDARY CONDITION SENSITIVITY

Changing upper boundary conditions on pressure may influence the Utah LAM precipitation forecast because this affects the column integrated divergence acceleration that is directly related to the vertical velocity. The first experiment in this chapter is the control with the $p' = 0$ upper boundary condition. The second experiment uses the Klemp-Durran (K-D) upper boundary condition in place of the $p' = 0$ condition. The third experiment uses an upper boundary condition proposed by Innocentini et al. (1993) which was modified and installed in the Utah LAM by Ciliberti (unpublished master's thesis draft). This will be referred to as the $w = 0$ upper boundary condition. The purpose of this chapter is to evaluate the Utah LAM precipitation forecast sensitivity to the choice of these different upper boundary conditions.

The simplest upper boundary condition is to set the pressure at the top of the model to the value provided by the outer model. This leaves the pressure deviation, p' , at the model top to be zero, and this upper boundary condition is called the $p' = 0$ upper boundary condition. The control experiment utilizes the $p' = 0$ upper boundary condition, a 40-second time step, outer model data from the NGM, Davies nudging at five grid points adjacent to the lateral boundaries, no spectral relaxation in the LAM interior (described in more detail in Chapter 5), a critical relative humidity for precipitation of 100%, subcloud evaporation, and the same diffusion and Fourier filtering of the moisture variable as for other variables.

Klemp and Durran (1983) developed a radiative upper boundary condition to reduce the problem of artificial reflection of gravity waves from the upper boundary. The purpose

of the K-D upper boundary condition is to radiate most of the gravity wave energy through the model top by allowing only gravity waves that propagate energy upward to exist at the upper boundary.

This is accomplished by computing the vertical velocity at the model top, w_{top} , through vertical integration of the continuity equation (from the bottom up) with the lower boundary condition set as the vertical velocity resulting from the wedging effect of the topography. Then, w_{top} is Fourier transformed, and the coefficients, w_{k_λ, k_ϕ} , lead to the following expression:

$$\hat{w}_{k_\lambda, k_\phi} = \frac{N w_{k_\lambda, k_\phi}}{(k_\lambda^2 + k_\phi^2)^{\frac{1}{2}}}, \quad (4.1)$$

where k_λ and k_ϕ are the wavenumbers in the zonal and meridional direction, respectively, and N is the Brunt-Väisälä frequency. The pressure correction for mode (k_λ, k_ϕ) is given at the model top by $\rho_s \hat{w}_{k_\lambda, k_\phi}$. This pressure is used as the upper boundary condition for the vertical integration of the hydrostatic equation (from the top down) to calculate the pressure throughout the column.

Although Klemp and Durran (1983) derived this upper boundary condition using a set of model equations that assumed linear, hydrostatic, Boussinesq flow in a uniform atmosphere without rotation, they show that it may be effective in a wide range of mesoscale modeling applications and in more general atmospheric conditions. Experiment 2 uses the K-D upper boundary condition in place of the $p' = 0$ condition. All other model aspects are as described for the $p' = 0$ experiment, and this experiment will hereafter be referred to as the K-D experiment.

An abbreviated derivation of the $w = 0$ upper boundary condition begins with the horizontal momentum equation:

$$\frac{\partial \bar{V}}{\partial t} = -\frac{1}{\rho_s} \nabla_h p + (\text{other terms}). \quad (4.2)$$

After multiplying both sides by ρ_s and applying the leapfrog time differencing scheme, the above equation becomes

$$\frac{\rho_s \bar{V}^{n+1} - \rho_s \bar{V}^{n-1}}{2\Delta t} = -\nabla_h p^n + (\text{other terms}). \quad (4.3)$$

Applying the horizontal divergence operator, ∇_h , and multiplying by $2\Delta t$ gives

$$\nabla_h \cdot (\rho_s \bar{V}^{n+1}) - \nabla_h \cdot (\rho_s \bar{V}^{n-1}) = 2\Delta t (-\nabla_h^2 p^n) + \nabla_h \cdot (\text{other terms}). \quad (4.4)$$

Integrating equation (4.4) vertically, from the model top down to the surface, results in

$$\int_{z_{top}}^{z_{sfc}} \nabla_h \cdot (\rho_s \bar{V}^{n+1}) dz - \int_{z_{top}}^{z_{sfc}} \nabla_h \cdot (\rho_s \bar{V}^{n-1}) dz = 2\Delta t \left(- \int_{z_{top}}^{z_{sfc}} \nabla_h^2 p^n dz + \int_{z_{top}}^{z_{sfc}} \nabla_h \cdot (\text{other terms}) \right). \quad (4.5)$$

The notation is simplified by substituting an overbar to symbolize the column integral and equation (4.5) becomes

$$\nabla_h \cdot \overline{(\rho_s \bar{V}^{n+1})} - \nabla_h \cdot \overline{(\rho_s \bar{V}^{n-1})} = 2\Delta t \left(-\nabla_h^2 \overline{(p^n)} + \nabla_h \cdot \overline{(\text{other terms})} \right). \quad (4.6)$$

The hydrostatic pressure at any level in the local model is denoted as $p_h(z)$ and given by

$$p_h(z) = - \int_{z_{top}}^z \rho_s g dz, \quad (4.7)$$

where the total pressure, $p(z)$, at any level is the sum of the hydrostatic pressure and the pressure at the model top, or

$$p(z) = p_h(z) + p_{top}. \quad (4.8)$$

Substituting for p in equation (4.6) using equation (4.8) above gives

$$\nabla_h \cdot \overline{(\rho_s \bar{V}^{n+1})} - \nabla_h \cdot \overline{(\rho_s \bar{V}^{n-1})} = 2\Delta t \left(-\nabla_h^2 \overline{p_h^n(z)} - \nabla_h^2 \overline{p_{top}} + \nabla_h \cdot \overline{(\text{other terms})} \right). \quad (4.9)$$

The method described by Innocentini et al. (1993) is to specify both the lower and upper boundary values of the initial vertical velocity to be zero. This specification ensures that the acceleration of the column integrated horizontal divergence remains zero if p_{top} is modified as discussed next.

Innocentini et al. (1993) suggest that the pressure at the model top used in the calculation of \bar{V}^{n+1} be corrected in order to offset the column-integrated horizontal divergence that would be otherwise nonzero at the n^{th} time step. This corrected pressure, $(p_{top}^{corr})^n$, is given by

$$\nabla_h^2 (p_{top}^{corr})^n = \frac{1}{2\Delta t} \nabla_h \cdot \overline{(\rho_s \bar{V}^{n+1})} + \nabla_h^2 (p_{top})^{n-1}. \quad (4.10)$$

If the vertical velocity at the surface is set to zero at every time step and the vertical velocity at the model top is zero at some previous time step, then this pressure correction can be used to predict a horizontal wind whose column integrated divergence acceleration is zero and the vertical velocity at the model top is then zero.

At time step n , the pressure correction term for the local model top is added to the pressure at the top from time step $n-1$. The local model pressure field is then obtained through vertical integration of the hydrostatic equation (from the top down) using the

corrected pressure at the model top. The model wind field can then be recomputed using the updated pressure field. The following steps describe the sequence of calculations discussed above:

- 1) Forecast the wind, \bar{V}^{n+1} , using p^n , w^n , and T^n . The horizontal wind \bar{V}^{n+1} produces w_{top}^{n+1} which does not equal zero because the column integrated horizontal divergence is nonzero.
- 2) Calculate the pressure correction term, $(p_{top}^{corr})^n$, using equation (4.10) and recalculate the pressure field at all model levels.
- 3) Recalculate the wind, \bar{V}^{n+1} . The column-integrated horizontal divergence and the resulting w_{top}^{n+1} will now be equal to zero (or very close to zero).

Innocentini et al. (1993) elected to skip step (3) and simply use the corrected pressure at all levels at the next time step, accepting a small imbalance in the horizontal momentum equations to reduce computations. However, Ciliberti (unpublished master's thesis draft) attempted to utilize this variation in the Utah LAM, and unacceptably large values of vertical velocity were produced at the model top. An advantage to this upper boundary condition, especially appealing to this research, is the ability of the model to remain stable with a larger time step because the condition $w_{top} = 0$ filters the most rapidly propagating gravity waves. This experiment, hereafter referred to as the $w = 0$ experiment, is otherwise configured as the $p' = 0$ and K-D experiments, but allows an 80-second time step (approximately two times that required in the $p' = 0$ and K-D experiments).

The $p' = 0$ Experiment

This and all other simulations performed in this study (unless noted otherwise) were initialized with data from 0000 UTC 27 June and run for 336 forecast hours to 0000 UTC 11 July 1993. However, only the output data from 0600 UTC 27 June to 0600 UTC 10 July are analyzed and presented for each experiment. The results of the control

experiment ($p' = 0$) are illustrated in Figures 4.1 through 4.3. Figure 4.1a shows the total precipitation produced by the Utah LAM for the 13-day period of 27 June to 9 July, and Figure 4.1b shows the 24-h rainfall for 5 July.

The maximum rain produced in this experiment fell in eastern Iowa and northern Illinois with amounts of 50.9 cm in Iowa and 57.1 cm in Illinois (Figure 4.1a). This experiment predicted the dry area in Kentucky and southern Illinois and Indiana, as well as the lack of precipitation throughout most of Texas (refer to Figure 3.1a for comparison). However, the model underpredicted precipitation in Minnesota, South Dakota, Nebraska, and especially Kansas where this simulation totally missed the 20-cm area in north-central Kansas.

For 5 July, the $p' = 0$ experiment generated a band of rainfall covering northeast Iowa and Wisconsin, with maxima slightly greater than 10 cm in Wisconsin. Comparison of Figure 4.1b and Figure 3.1b indicates that the Utah LAM performed well for this 24-h period. The 5-cm contour in Figure 4.1b is very close to the 5-cm contour shown in Figure 3.1b.

As mentioned in Chapter 3, the Utah LAM has been applied to several past studies of the diurnal cycle in the boundary layer. Figures 4.2 and 4.3 illustrate the diurnal cycle of the precipitation and 850-mb winds as produced by the $p' = 0$ experiment. The four maps displaying 6-h precipitation totals for the 6 h preceding 0600 UTC, 1200 UTC, 1800 UTC, and 2400 UTC (Figures 4.2a-d) were created summing all the output (for the respective 6-h time period) from the 13 days of 27 June to 9 July. Figures 4.3a-d show the 850-mb winds for 0600 UTC, 1200 UTC, 1800 UTC, and 2400 UTC, respectively, averaged over the entire 13-day period. The general diurnal cycle of the precipitation is in agreement with the diurnal variation shown in the observation data in Chapter 3 (Figures 3.4a-d) in that the greatest amount of rain was generated between local midnight and 6 am. Of the 55 cm predicted in northern Illinois for the 13-day period (see Figure 4.1a), 25 cm was produced during this 6-h time period. The 850-mb winds, although faster than the

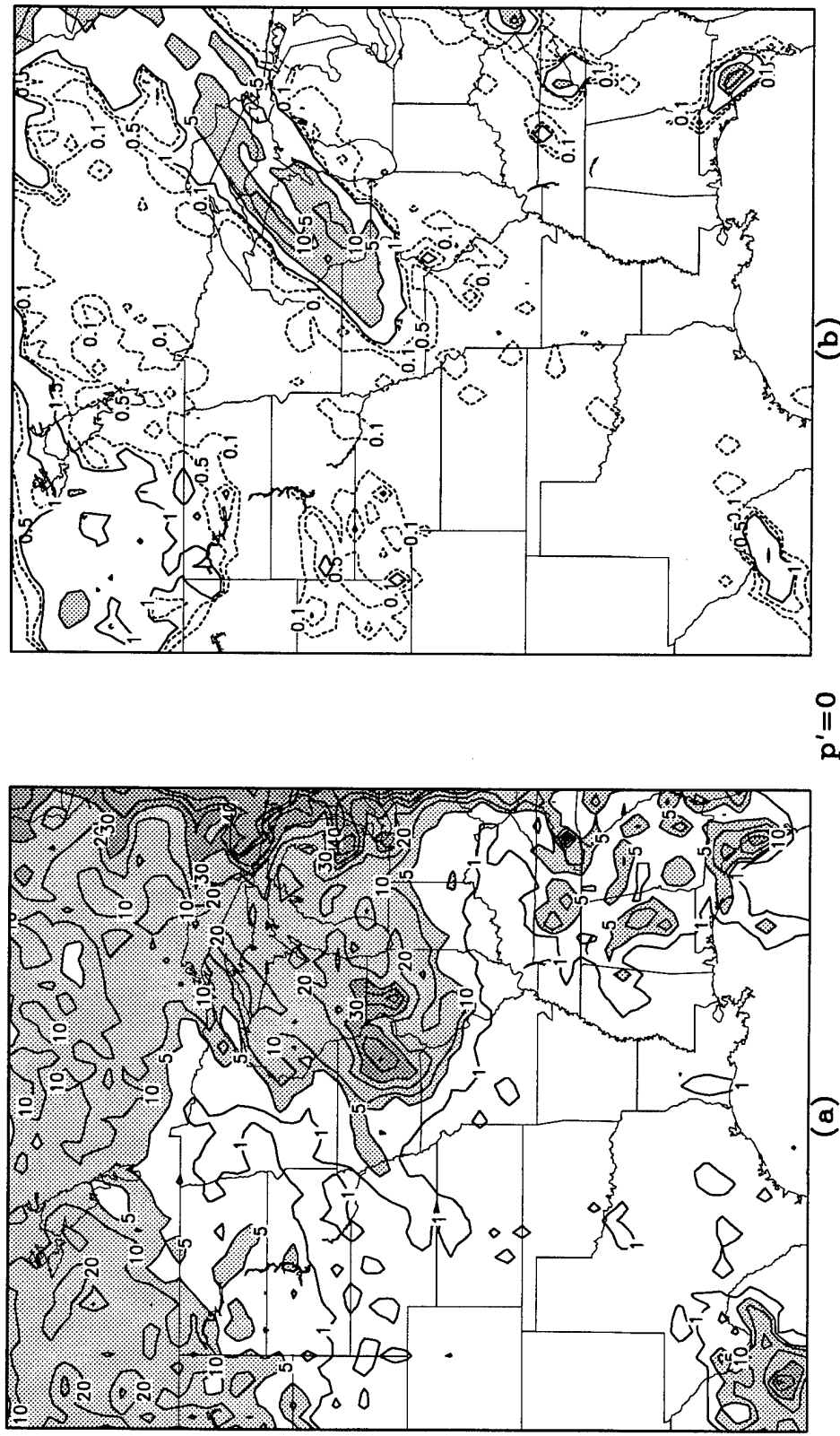


Figure 4.1. Utah LAM output from the $p' = 0$ experiment: (a) 13-day total rainfall predicted for 0600 UTC 27 June to 0600 UTC 10 July, (b) 24-h rainfall predicted for 5 July. In (a), contours are for 1, 5, 10, 20, 30, 40, 50, and 60 cm, with light shading above 5 cm and dark shading above 30 cm. In (b), contours are dashed for 0.1 and 0.5 cm and solid for 1, 5, 10, and 20 cm, with shading above 5 cm.

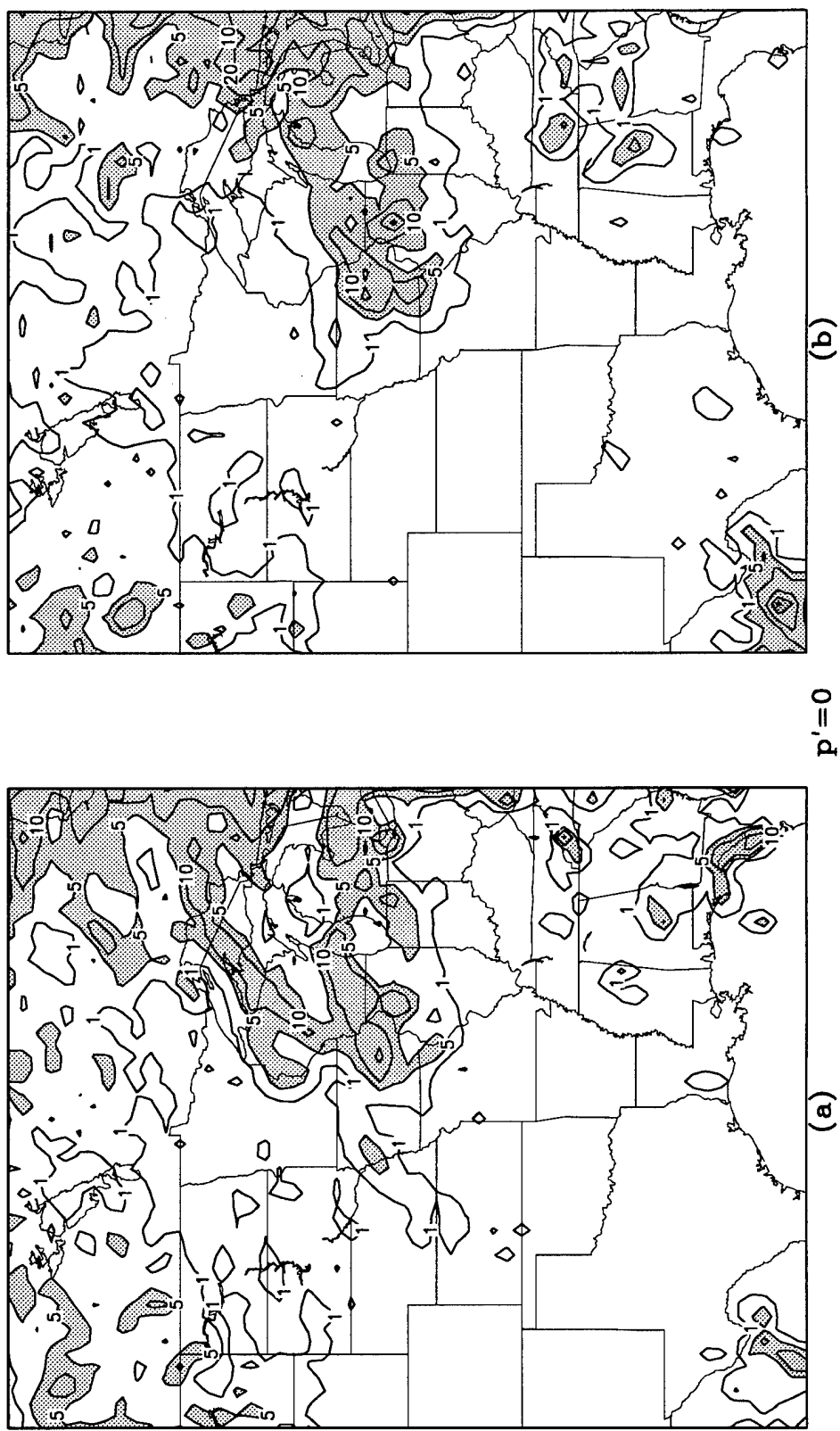


Figure 4.2. Utah LAM total precipitation during four 6-h time blocks for the 13-day period 27 June to 9 July 1993, as predicted by the $p' = 0$ experiment. Each panel represents a different 6-h block: (a) 0000 to 0600 UTC, (b) 0600 to 1200 UTC, (c) 1200 to 1800 UTC, and (d) 1800 to 2400 UTC. Units are cm and contours are at 1, 5, 10, 20, 30, and 40 cm, with light shading above 5 cm and dark shading above 30 cm.

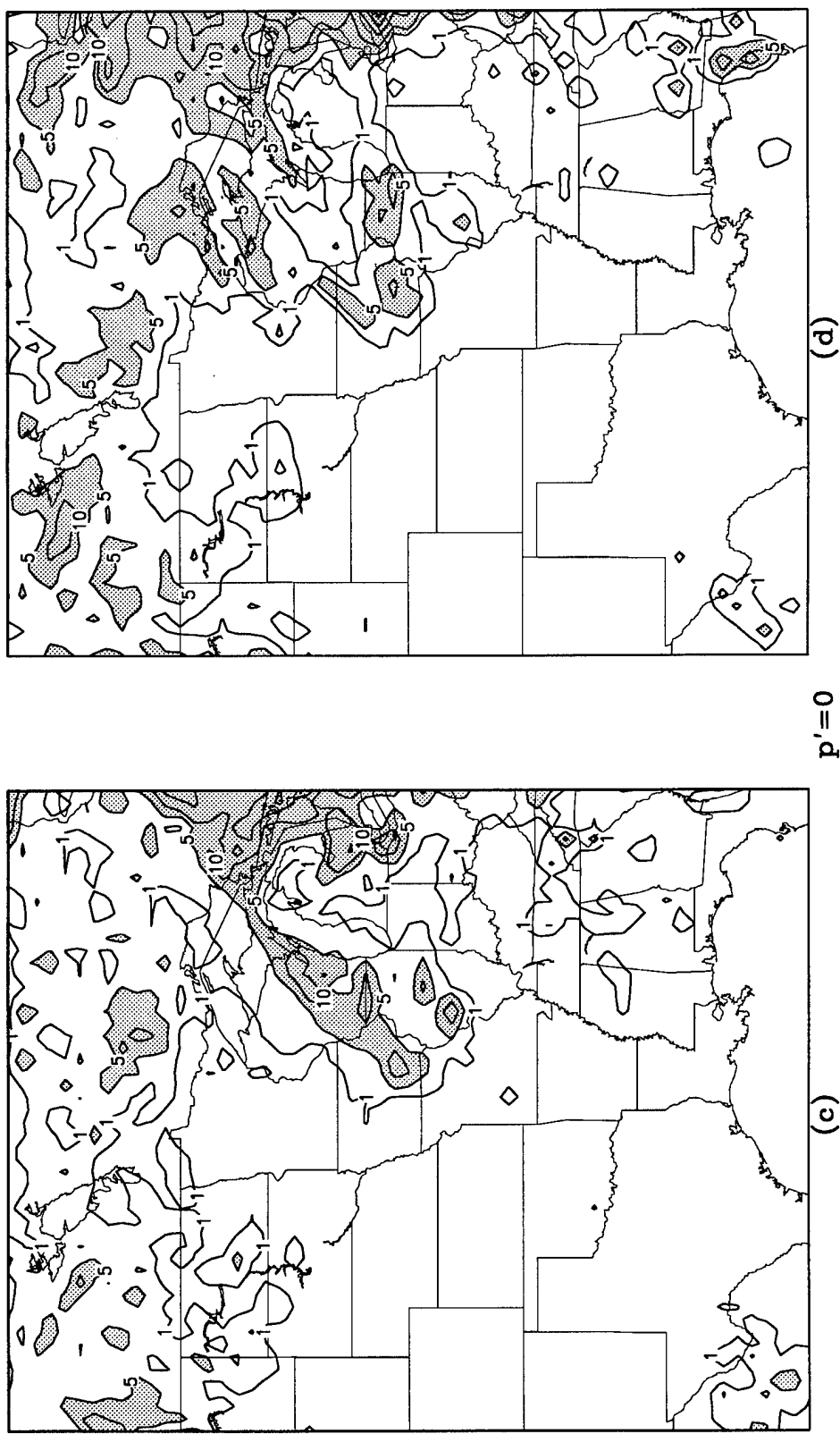


Figure 4.2. (Continued)

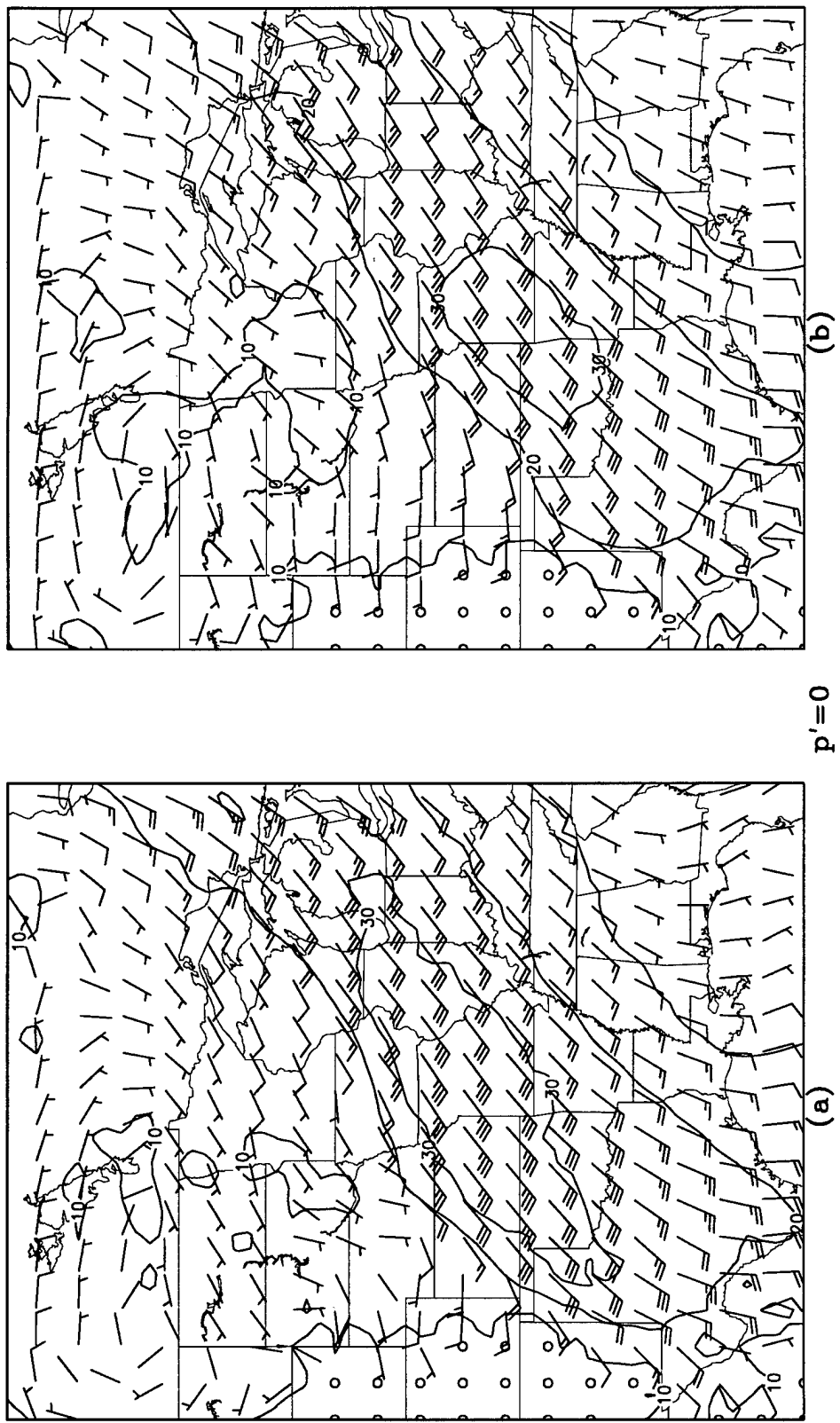


Figure 4.3. Utah LAM 850-mb wind averaged at (a) 0600 UTC, (b) 1200 UTC, (c) 1800 UTC, and (d) 2400 UTC using model output every 6 h from 0600 UTC 28 June to 0600 UTC 10 July from the $p' = 0$ experiment. Units are m s^{-1} . The wind barbs are displayed at every third grid point; however the contouring considers all grid points in the domain.

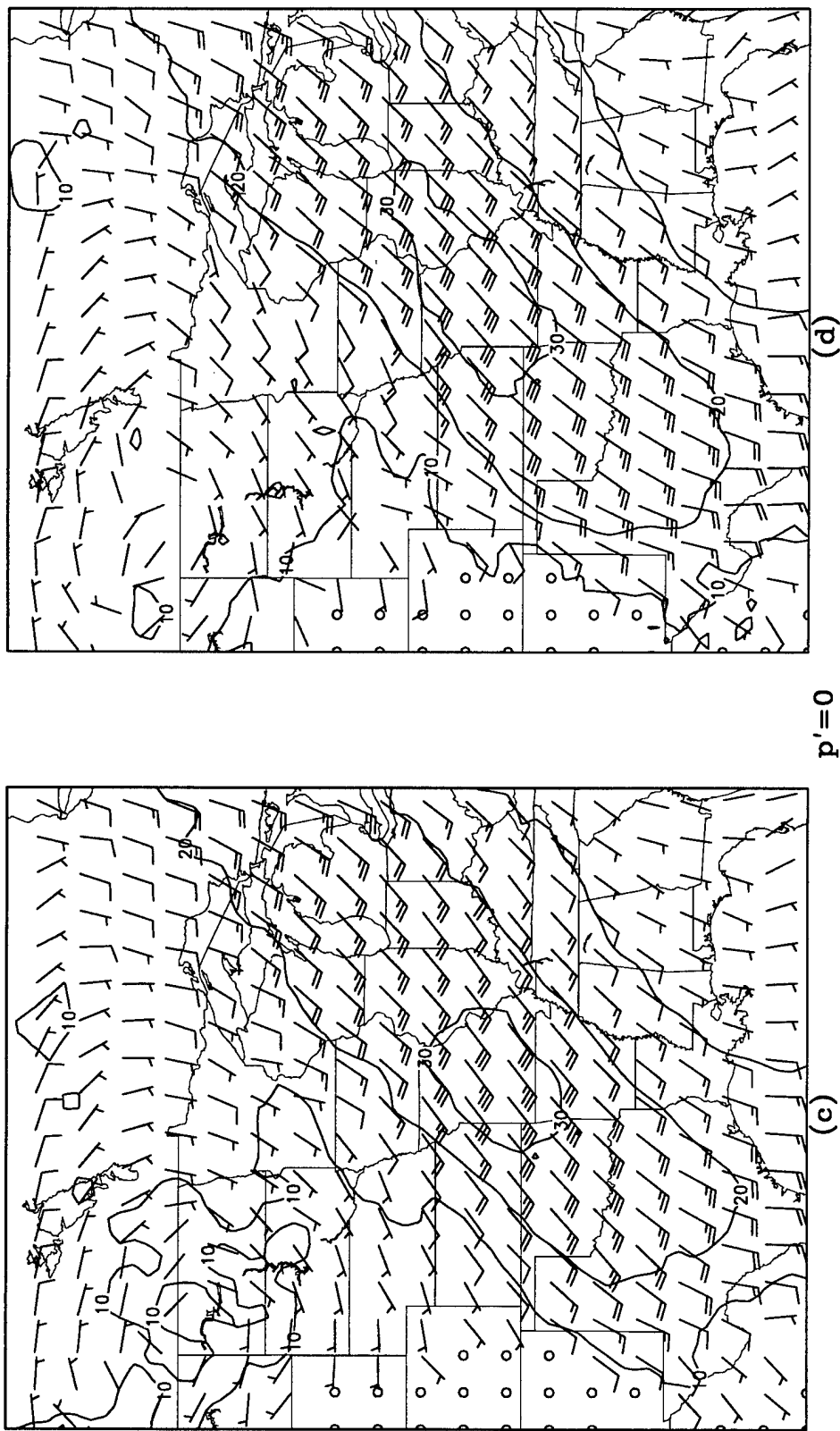


Figure 4.3. (Continued)

850-mb sounding data indicate (Figure 3.5), also exhibit typical diurnal variation with maxima at midnight and 6 am local time (1200 UTC).

The K-D Experiment

The K-D experiment was executed with a 40-second time step, but the solution became unstable and blew-up after 210 h of forecast time. Therefore, a supplemental simulation was executed with a 30-second time step, for 132 h, beginning at 1200 UTC 5 July and ending at 0000 UTC 11 July. The output from the "40 second" simulation was salvaged for 0000 UTC 27 June to 1800 UTC 5 July and merged with the output from the "30 second" simulation to create a full data set. As stated earlier in this chapter, only the output from 0600 UTC 27 June to 0600 UTC 10 July is presented below.

The 13-day rainfall and 24-h 5 July precipitation from the K-D experiment are shown in Figures 4.4 and 4.5 in the same manner as Figures 4.1 and 4.2, respectively. Overall, the K-D experiment produced more rainfall than the $p' = 0$ experiment with a maximum of 64.5 cm in eastern Iowa for the 13 days (Figure 4.4a) and an area of 15 cm or more in northeast Iowa and southwest Wisconsin with a maximum of 25.7 cm for 5 July (Figure 4.4b). Similarities in the 13-day precipitation field include the dryness in Texas and east into Kentucky and Tennessee, as well as the underprediction of rainfall in Kansas and north into western Minnesota. One notable difference is that the K-D experiment did not produce another local maximum in northern Illinois as in the $p' = 0$ experiment, and there is a small area greater than 50 cm in southwest Wisconsin not produced by the previous experiment.

The diurnal variation of the precipitation from the K-D experiment (see Figure 4.5) paralleled the $p' = 0$ experiment with the greatest amounts of rainfall during the 0000 to 0600 UTC and 0600 to 1200 UTC time periods (panels a and b). However, as stated above, the K-D experiment produced more rainfall than the $p' = 0$ experiment over Iowa, Illinois, and Wisconsin. The placement and variation of the LLJ in the K-D and $p' = 0$

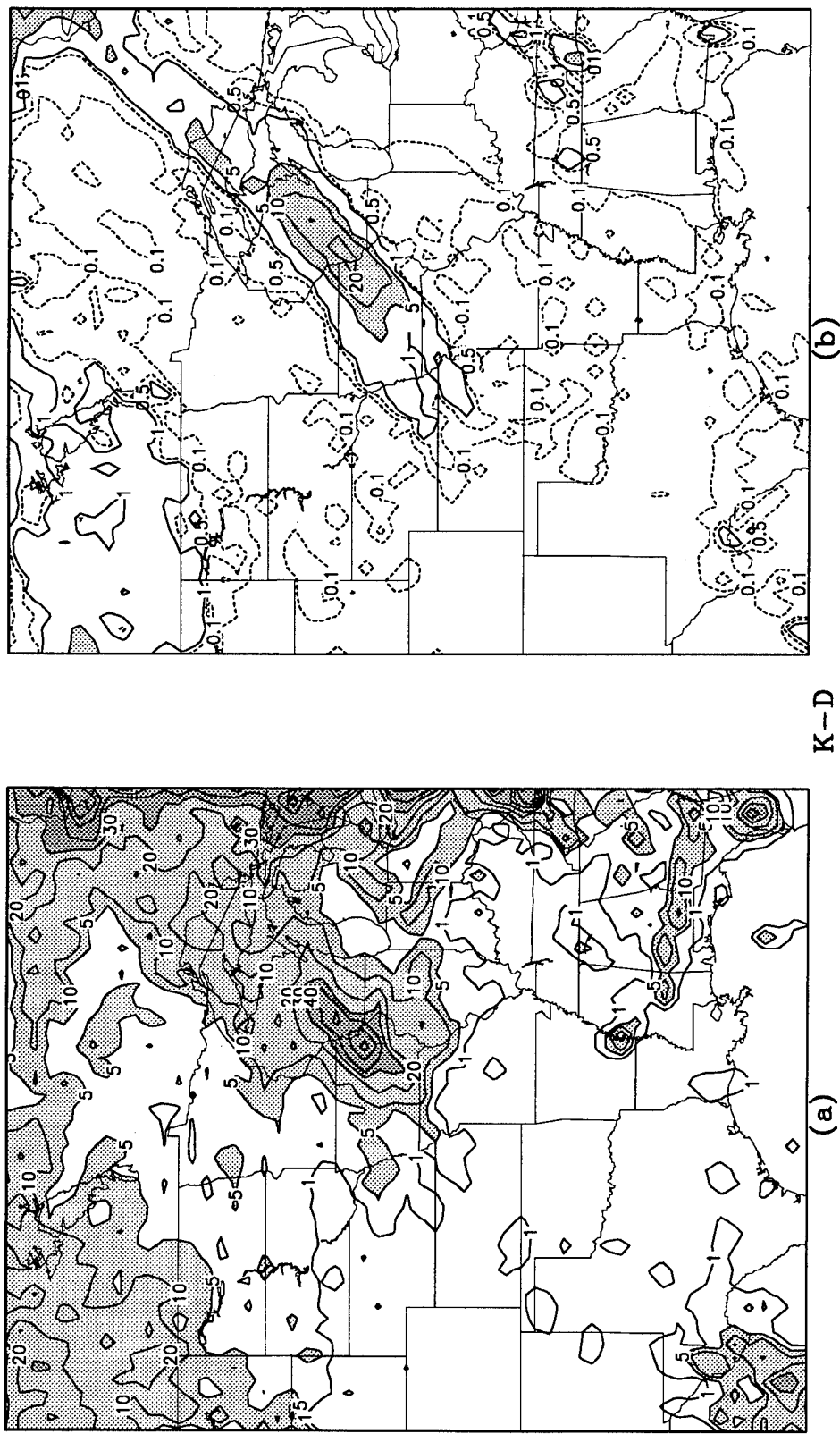


Figure 4.4. Utah LAM output from the K-D experiment: (a) 13-day total rainfall predicted for 0600 UTC 27 June to 0600 UTC 10 July, (b) 24-h rainfall predicted for 5 July. In (a), contours are for 1, 5, 10, 20, 30, 40, 50, and 60 cm, with light shading above 5 cm and dark shading above 30 cm. In (b), contours are dashed for 0.1 and 0.5 cm and solid for 1, 5, 10, and 20 cm, with shading above 5 cm.

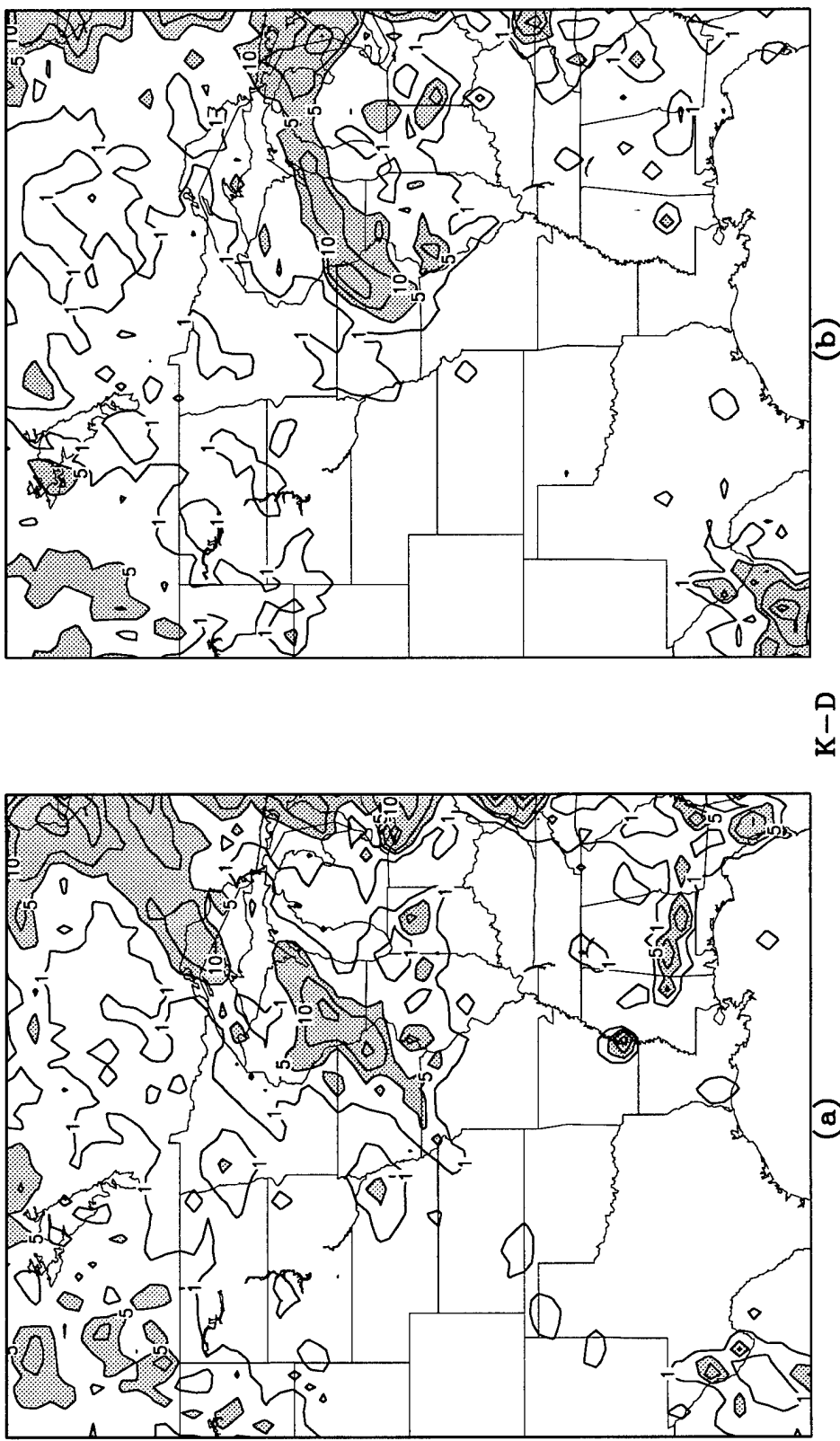


Figure 4.5. Utah LAM total precipitation during four 6-h time blocks for the 13-day period 27 June to 9 July 1993, as predicted by the K-D experiment. Each panel represents a different 6-h block: (a) 0000 to 0600 UTC, (b) 0600 to 1200 UTC, (c) 1200 to 1800 UTC, and (d) 1800 to 2400 UTC. Units are cm and contours are at 1, 5, 10, 20, 30, and 40 cm, with light shading above 5 cm and dark shading above 30 cm.

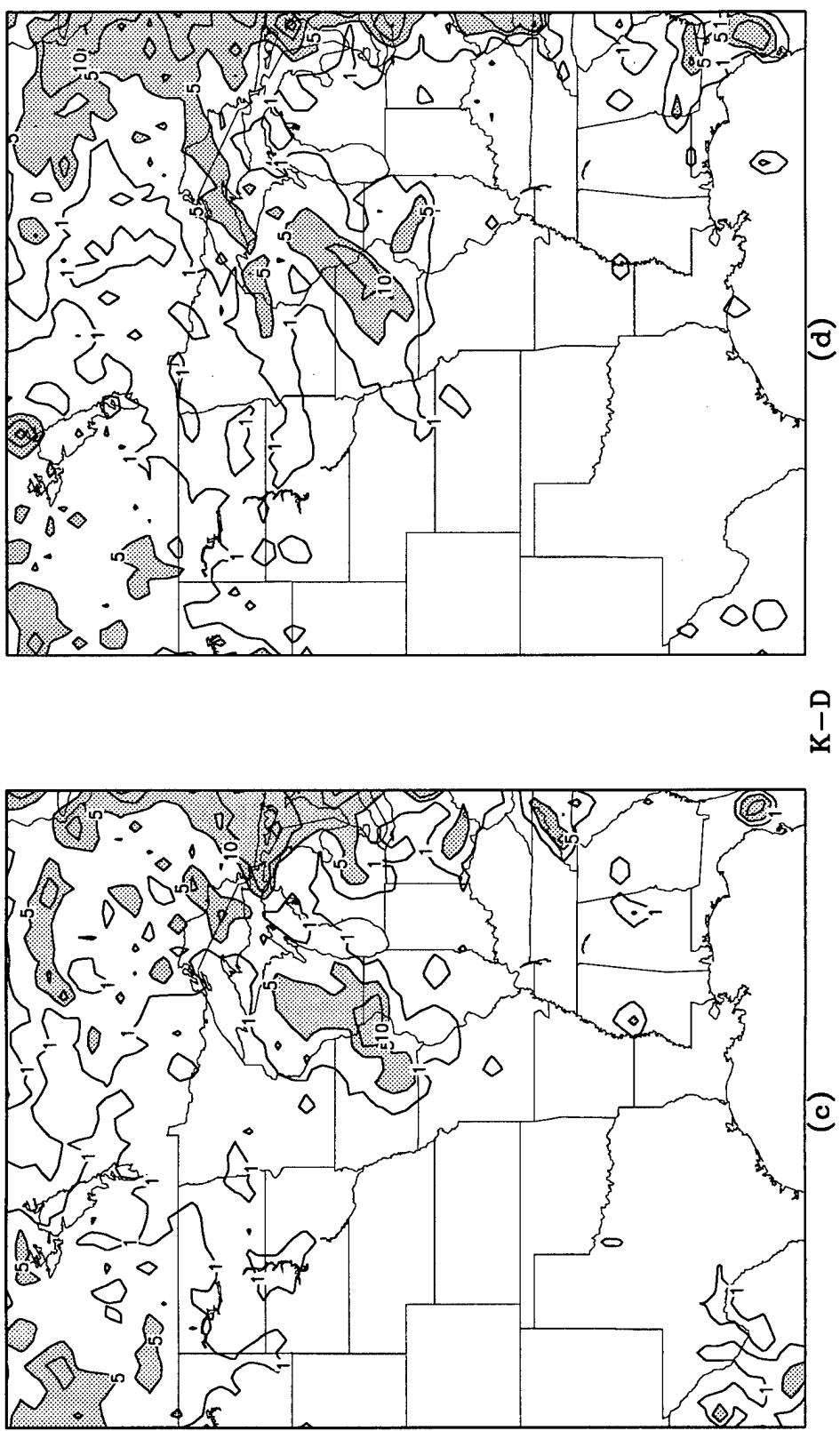


Figure 4.5. (Continued)

experiments are similar, but the wind speeds in the K-D experiment are slightly slower (results not shown).

The $w=0$ Experiment

The LAM output for the $w = 0$ experiment is illustrated in Figures 4.6, 4.7, and 4.8. Figure 4.6a shows that the $w = 0$ experiment produced significantly less rainfall than the previous two experiments. The 13-day maximum is 36.5 cm located in northern Illinois and the 20 cm contour covers little more than the northern part of the state. Significantly less rain was produced over eastern Iowa; however an area of 5 cm was generated to the southwest, just north of Kansas City, Missouri, and into northeast Kansas. Virtually no precipitation was predicted over Minnesota, eastern South Dakota, and Nebraska and the Gulf Coast precipitation seen in the two previous experiments is significantly less. This experiment resulted in a substantial underforecast of rainfall in the Upper Mississippi River Basin for the 13-day period.

The model prediction for 5 July is shown by Figure 4.6b. Although the rain band has been shifted to the east and its area decreased (especially the coverage of the 5 cm contour), the maximum of 8.8 cm is closer in magnitude to the actual precipitation (see Figure 3.1b) than the K-D experiment. The $w = 0$ experiment underpredicted the amount of rainfall for 5 July within the area from northeast Kansas to southwest Wisconsin as it had for the entire 13 days.

This experiment produced some changes to the diurnal variation of the precipitation and the LLJ (see Figs 4.7a-d and Figs 4.8a-d). Unlike the previous two experiments, the $w = 0$ case produced more rainfall in eastern Iowa and northern Illinois between 1200 and 1800 UTC (Figure 4.7c) than during 0600 to 1200 UTC (Figure 4.7b) and 1800 to 2400 UTC (Figure 4.7d). However, more precipitation fell between 0000 and 0600 UTC than the rest of the day, and it is evident that the 5-cm contour in northeast Kansas shown in the 13-day field (Figure 4.6a) (which was not produced in the $p' = 0$ and K-D experiments)

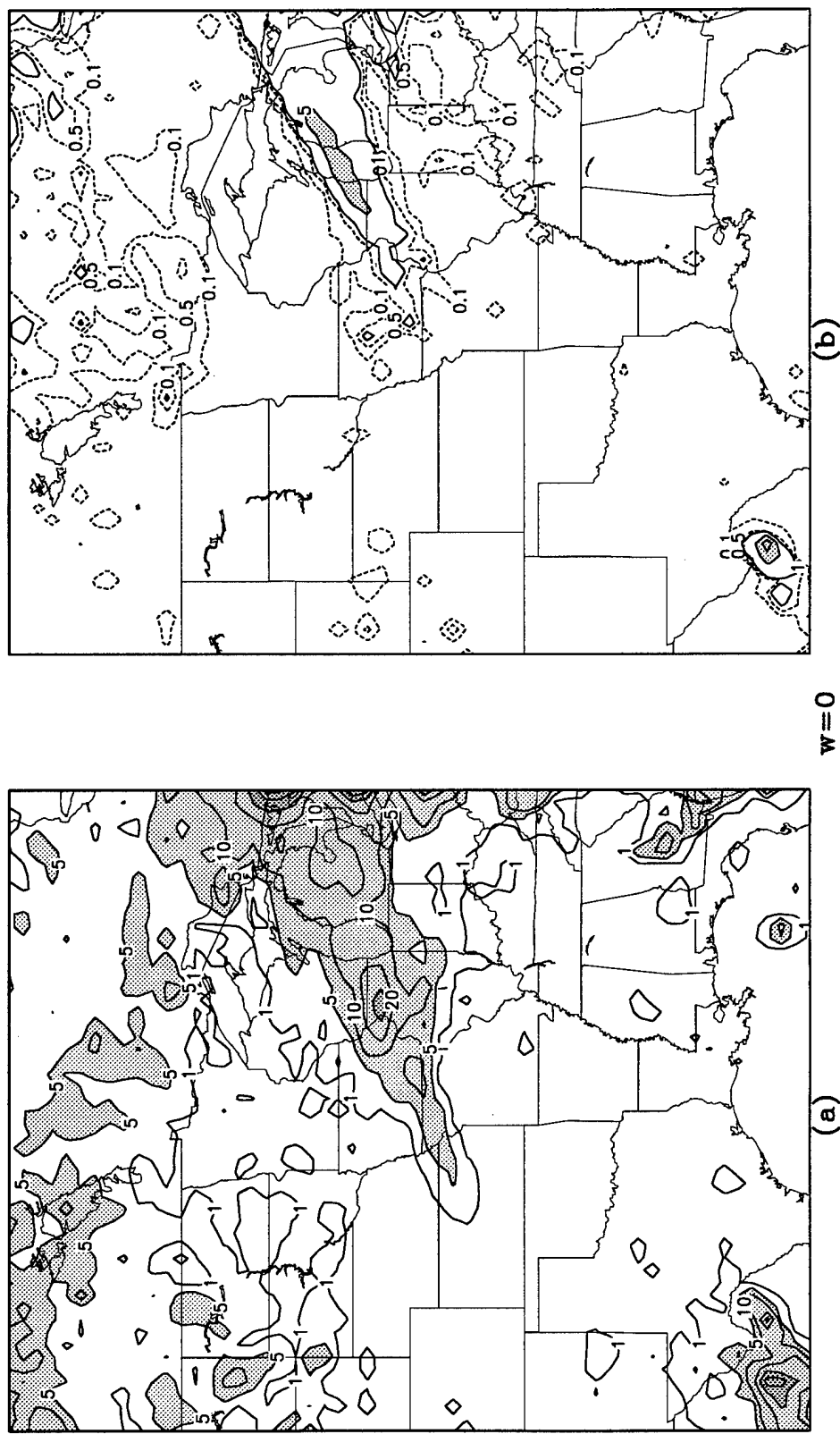


Figure 4.6. Utah LAM output from the $w=0$ experiment: (a) 13-day total rainfall predicted for 0600 UTC 27 June to 0600 UTC 10 July, (b) 24-h rainfall predicted for 5 July. In (a), contours are for 1, 5, 10, 20, 30, 40, 50, and 60 cm, with light shading above 5 cm and dark shading above 30 cm. In (b), contours are dashed for 0.1 and 0.05 cm and solid for 1, 5, 10, and 20 cm, with shading above 5 cm.

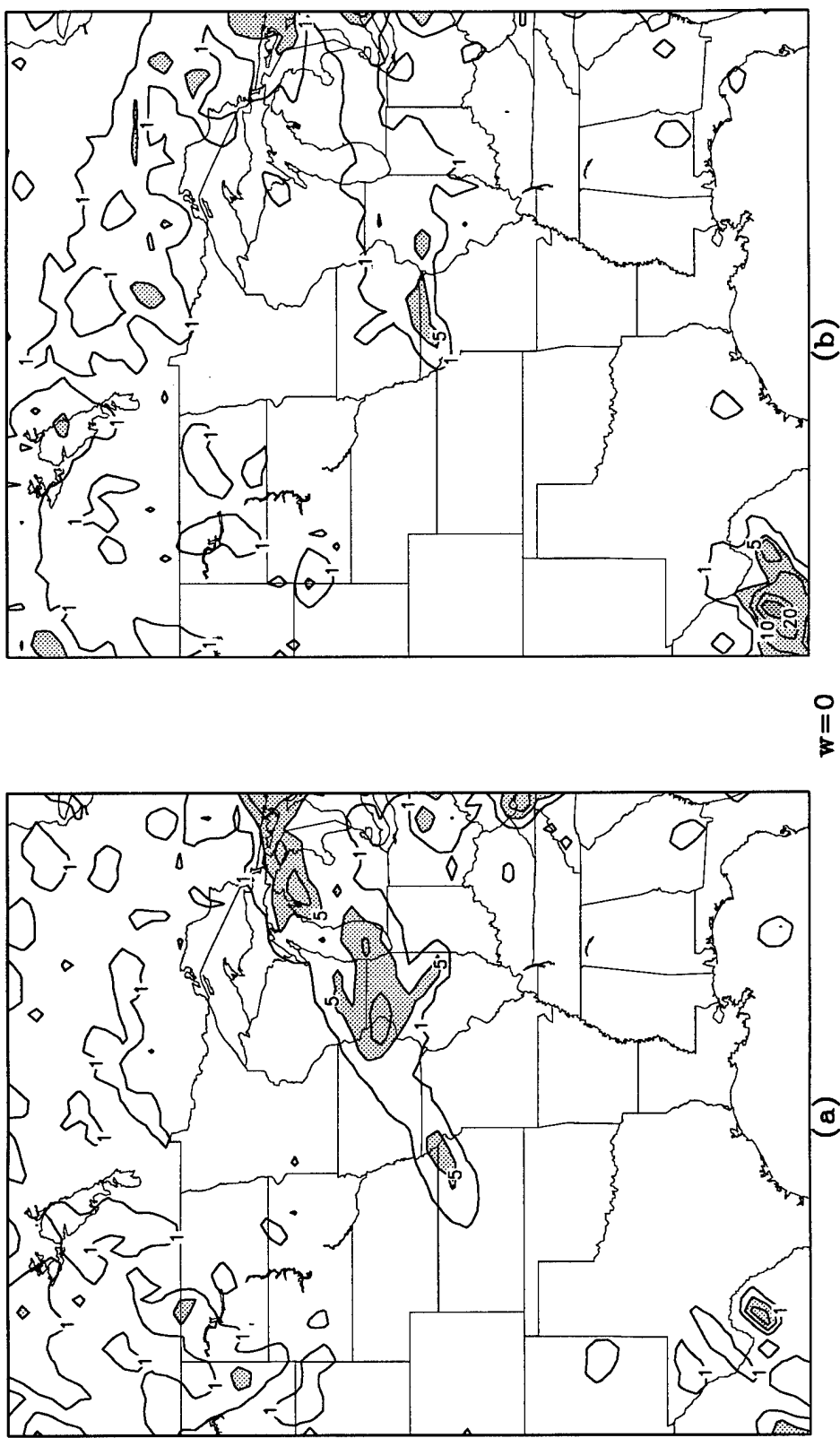


Figure 4.7. Utah LAM total precipitation during four 6-h time blocks for the 13-day period 27 June to 9 July 1993, as predicted by the $w = 0$ experiment. Each panel represents a different 6-h block: (a) 0000 to 0600 UTC, (b) 0600 to 1200 UTC, (c) 1200 to 1800 UTC, and (d) 1800 to 2400 UTC. Units are cm and contours are at 1, 5, 10, 20, 30, and 40 cm, with light shading above 5 cm and dark shading above 30 cm.

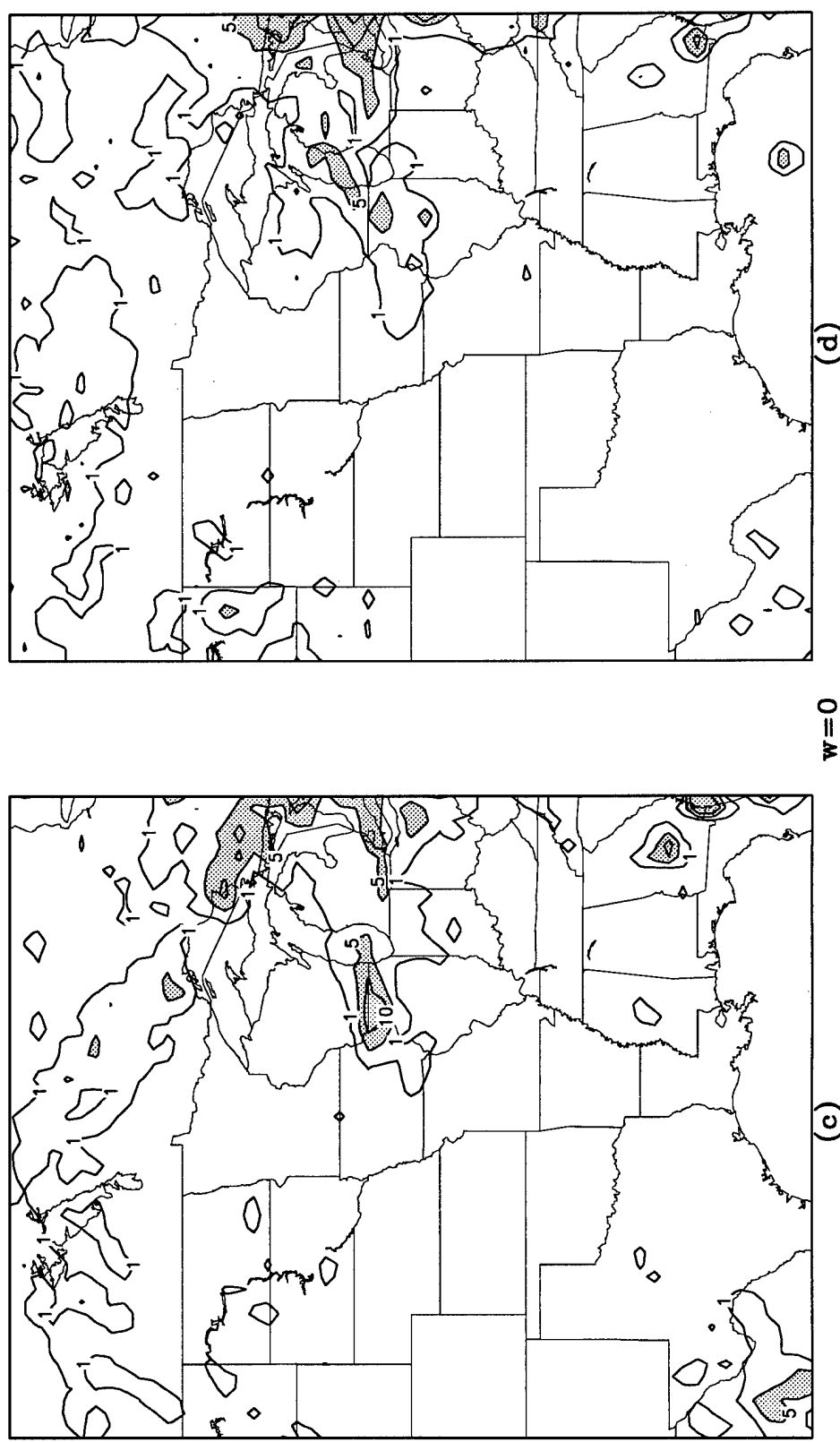


Figure 4.7. (Continued)

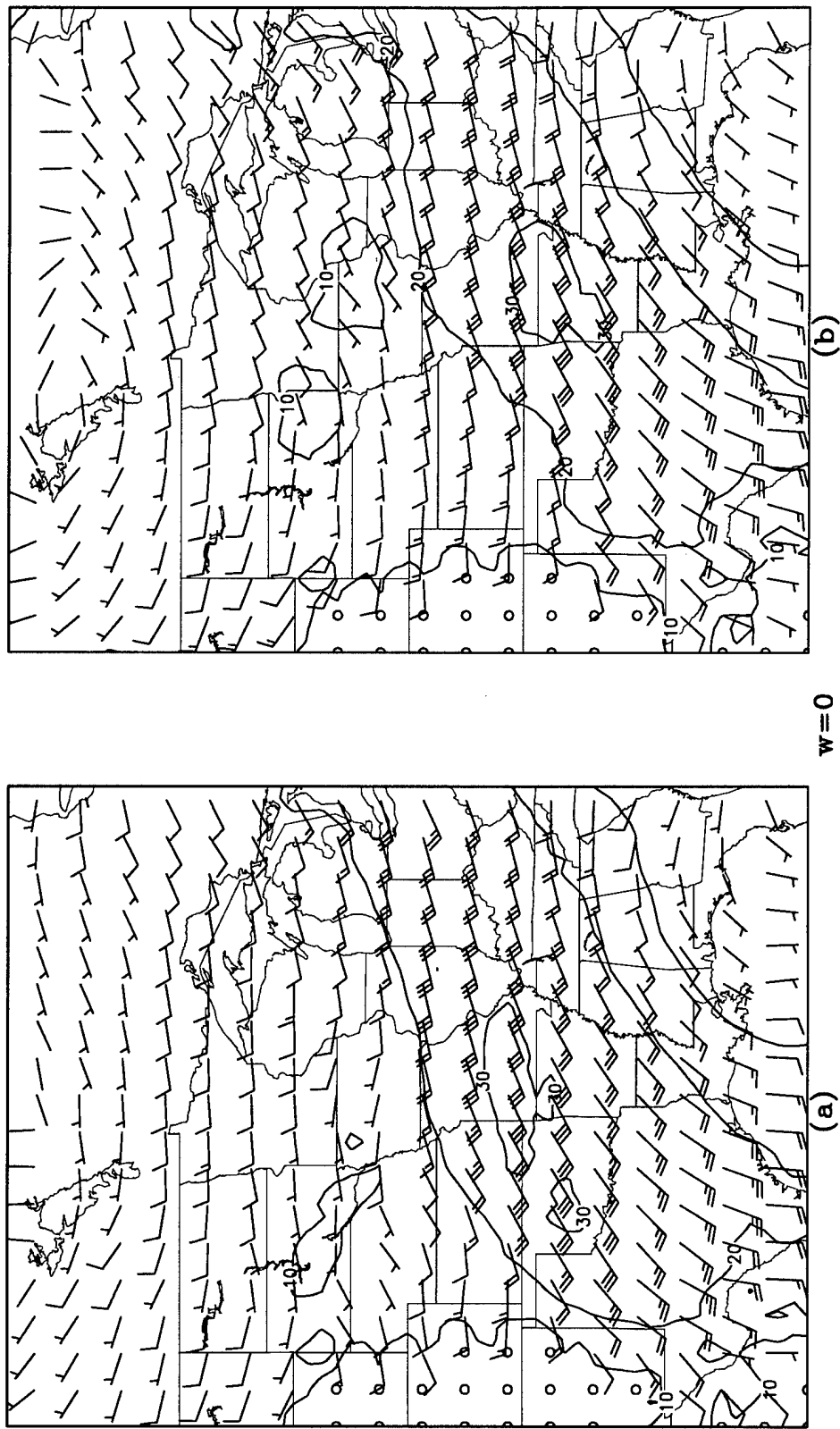


Figure 4.8. Utah LAM 850-mb wind averaged at (a) 0600 UTC, (b) 1200 UTC, (c) 1800 UTC, and (d) 2400 UTC using model output every 6 h from 0600 UTC 28 June to 0600 UTC 10 July from the $w=0$ experiment. Units are m s^{-1} . The wind barbs are displayed at every third grid point; however the contouring considers all grid points in the domain.

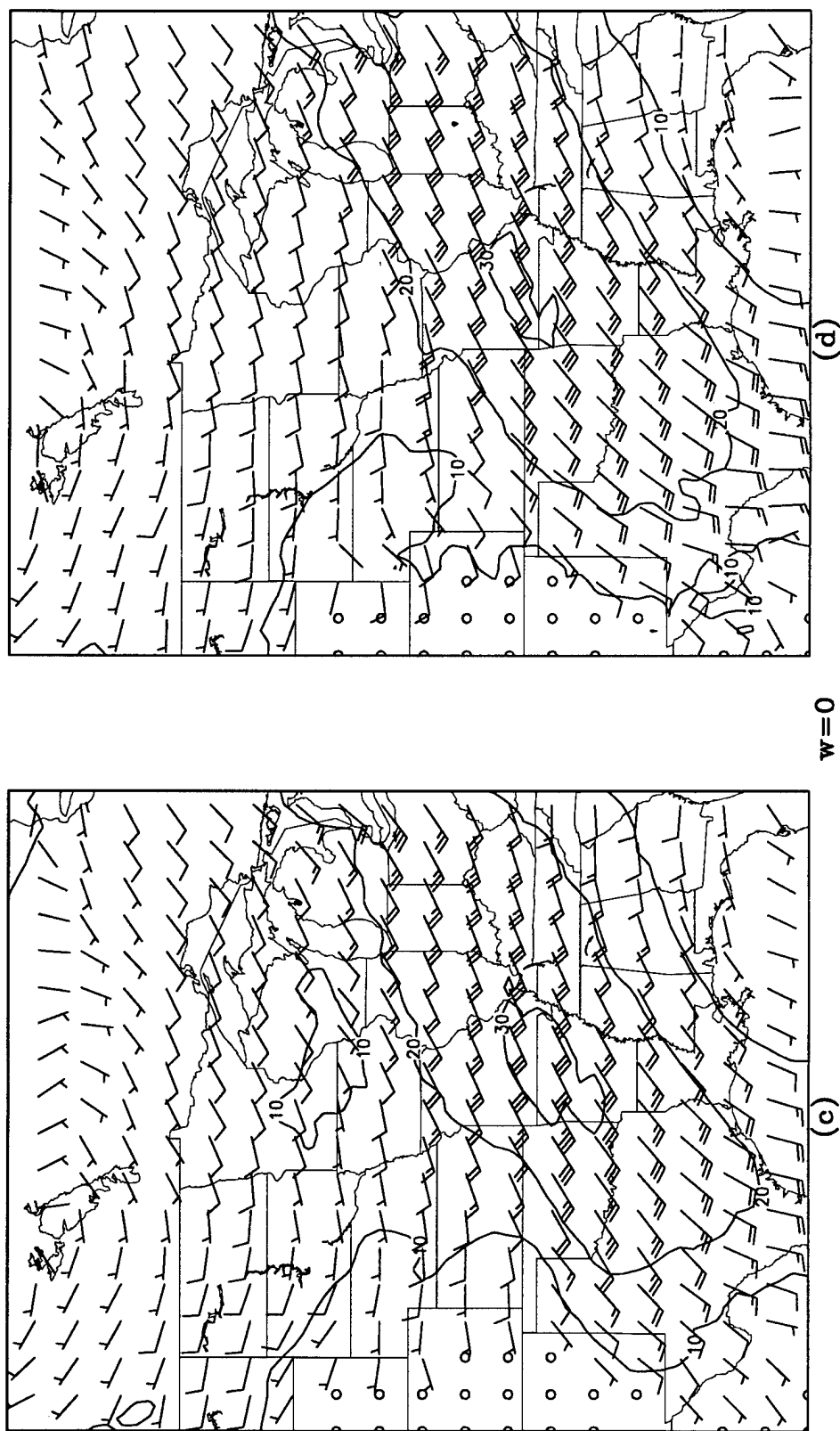


Figure 4.8. (Continued)

was from rain generated primarily between 0000 and 0600 UTC (see Figures 4.7a-d). Further investigation showed that the Utah LAM predicted this precipitation as the sum of accumulations from 7, 8, and 9 July only (these results are not shown). The 850-mb winds from the $w = 0$ experiment (Figure 4.8) show little diurnal variation and a slight increase in the westerly component and do not extend as far north as in the previous two experiments. Evaluation of the 500-m winds from this experiment indicates a stronger diurnal cycle (results not shown). The $p' = 0$ and K-D experiments generated wind speeds of 20 to 30 $m s^{-1}$ in southeast Iowa, northern Illinois, and southeast Wisconsin, and the $w = 0$ experiment generated wind speeds less than 20 $m s^{-1}$ in those areas.

CHAPTER 5

LATERAL BOUNDARY CONDITION SENSITIVITY

The purpose of this chapter is to evaluate the Utah LAM precipitation forecast sensitivity to changes of lateral boundary data analysis and to methods of lateral boundary implementation method.

Lateral Boundary Data Origin

Waldron et al. (1996) examined Utah LAM sensitivity to lateral boundary data origin for short-duration simulations of 12 to 24 h. To test the sensitivity of longer simulations to the type of data applied at the boundaries, two experiments were performed that used the reanalysis data (Kalnay et al. 1996) rather than the NGM analysis and 6 h forecasts. One experiment used the $p' = 0$ upper boundary condition and the other the $w = 0$ upper boundary condition. These two experiments will be referred to as the reanalysis $p' = 0$ and reanalysis $w = 0$ experiments, respectively. The results of these two reanalysis simulations will be compared to the $p' = 0$ experiment and the $w = 0$ experiment discussed previously, as well as to each other. Figures 5.1 and 5.2 show the precipitation generated by the reanalysis $p' = 0$ experiment and Figures 5.3 and 5.4 illustrate the results for the reanalysis $w = 0$ experiment.

Comparison of the 13-day precipitation fields between the two $p' = 0$ experiments (Figures 4.1a and 5.1a) shows that the reanalysis $p' = 0$ experiment produced less rainfall in eastern Iowa and northern Illinois with a maximum value of 45.9 cm in Iowa compared to 50.9 cm in the $p' = 0$ experiment with the NGM data. Similar comparison of the two $w = 0$ experiments (Figures 4.6a and 5.3a) indicates a more significant difference with a

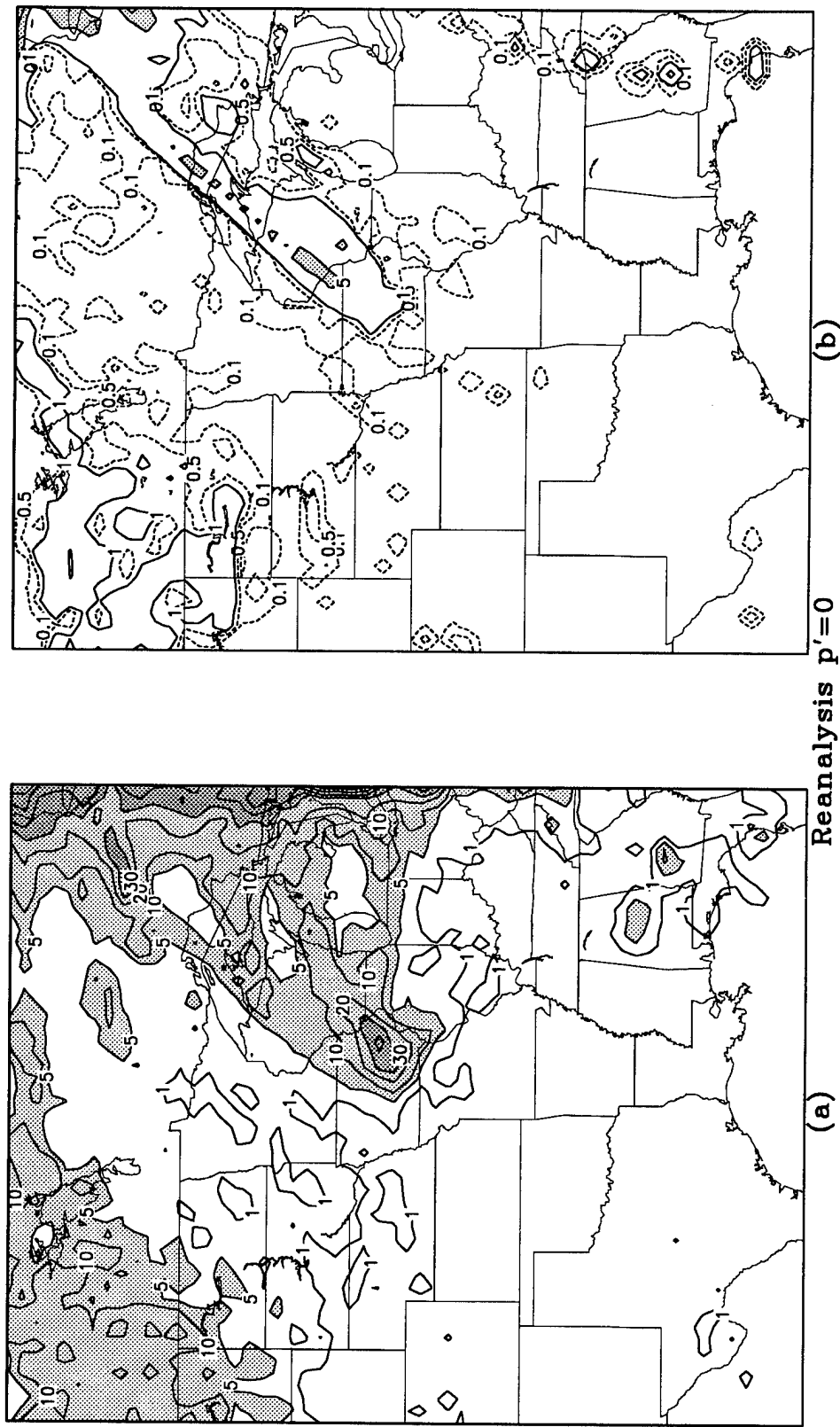


Figure 5.1. Utah LAM output from the reanalysis $p' = 0$ experiment: (a) 13-day total rainfall predicted for 0600 UTC 27 June to 0600 UTC 10 July, (b) 24-h rainfall predicted for 5 July. In (a), contours are for 1, 5, 10, 20, 30, 40, 50, and 60 cm, with light shading above 5 cm and dark shading above 30 cm. In (b), contours are dashed for 0.1 and 0.5 cm and solid for 1, 5, 10, and 20 cm, with shading above 5 cm.

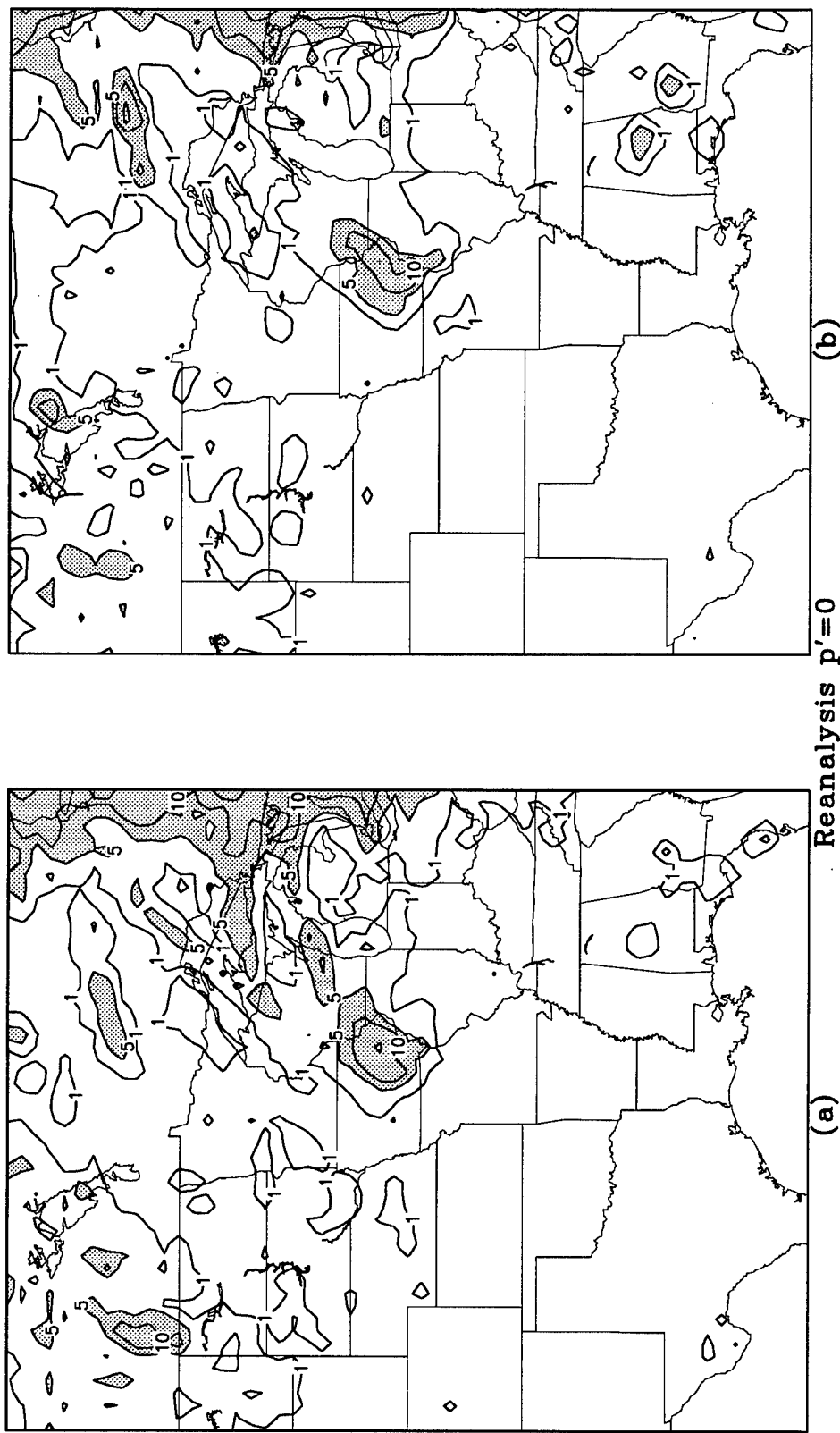


Figure 5.2. Utah LAM total precipitation during four 6-h time blocks for the 13-day period 27 June to 9 July 1993, as predicted by the reanalysis $p' = 0$ experiment. Each panel represents a different 6-h block as follows: (a) 0000 to 0600 UTC, (b) 0600 to 1200 UTC, (c) 1200 to 1800 UTC, and (d) 1800 to 2400 UTC. Units are cm and contours are at 1, 5, 10, 20, 30, and 40 cm, with light shading above 5 cm and dark shading above 30 cm.

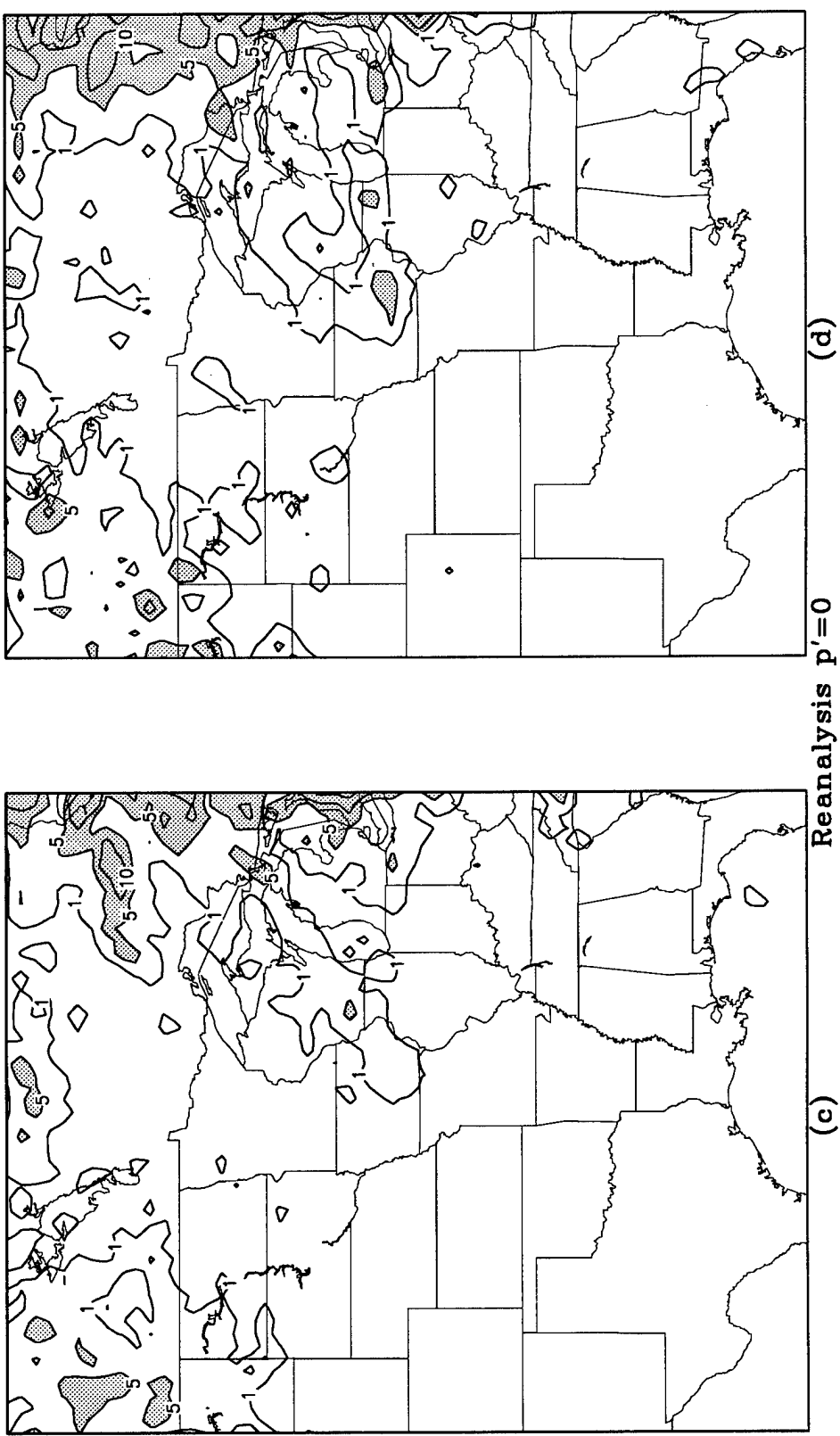


Figure 5.2. (Continued)

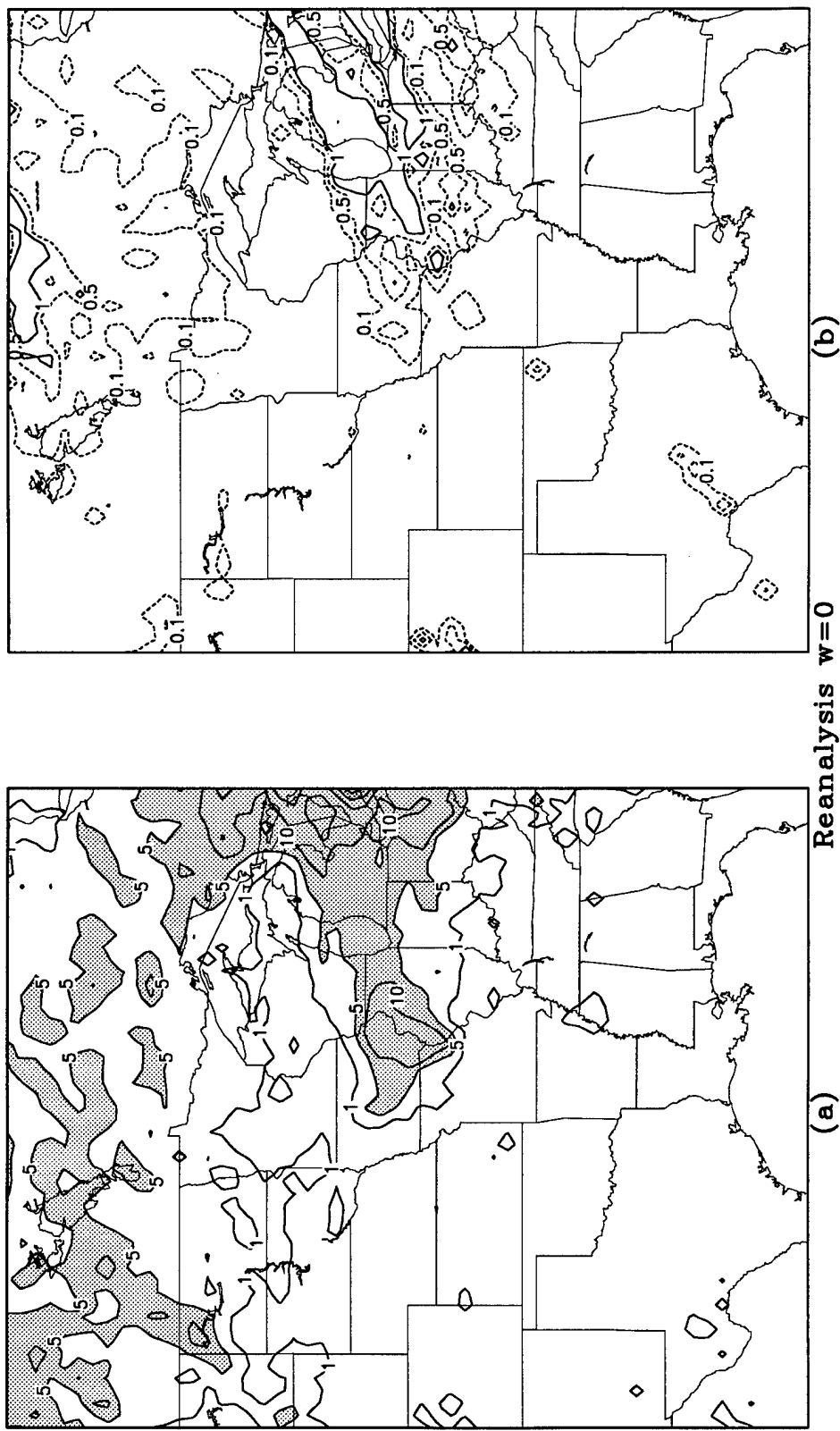


Figure 5.3. Utah LAM output from the reanalysis $w=0$ experiment: (a) 13-day total rainfall predicted for 0600 UTC 27 June to 0600 UTC 10 July, (b) 24-h rainfall predicted for 5 July. In (a), contours are for 1, 5, 10, 20, 30, 40, 50, and 60 cm, with light shading above 5 cm and dark shading above 30 cm. In (b), contours are dashed for 0.1 and 0.5 cm and solid for 1, 5, 10, and 20 cm, with shading above 5 cm.

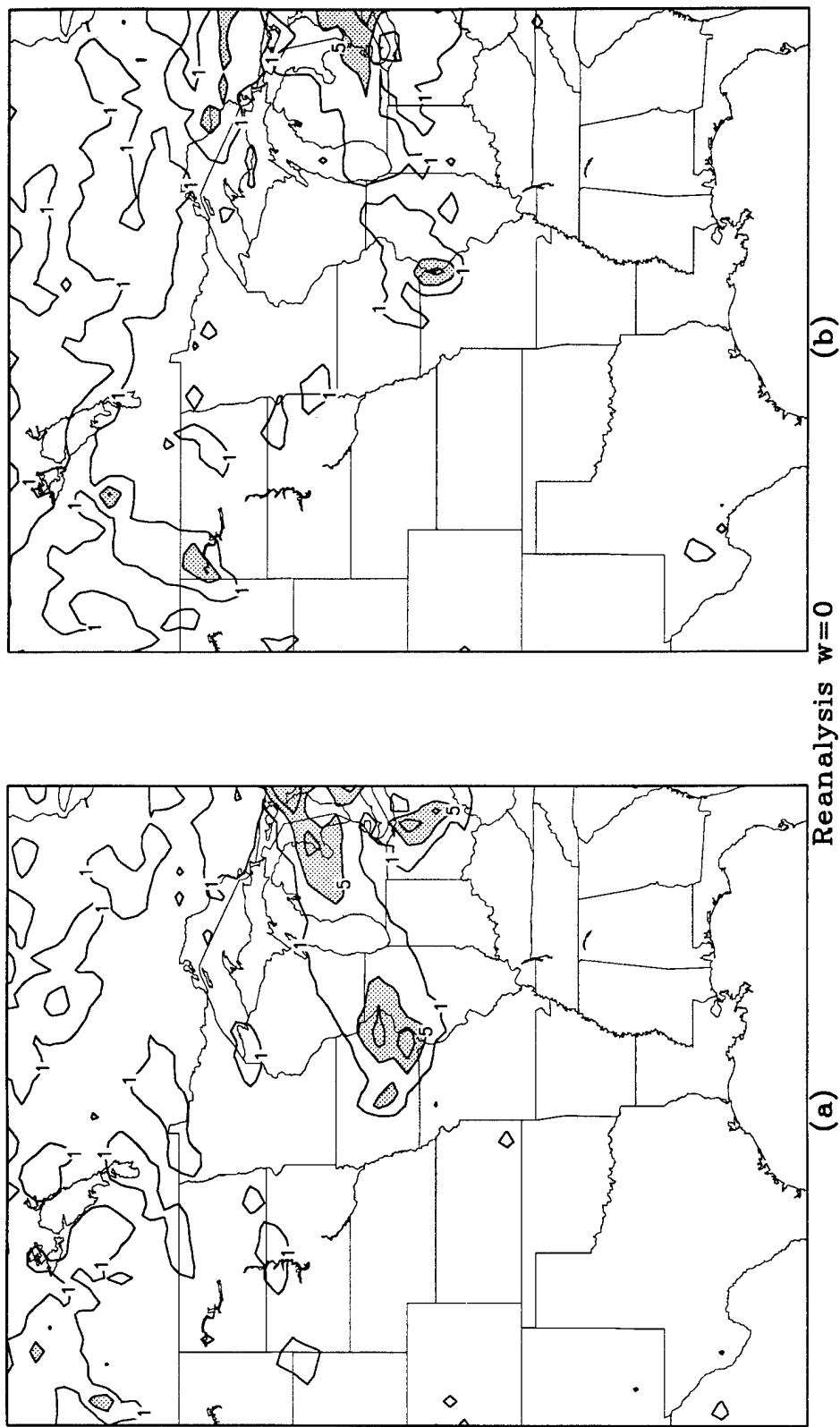


Figure 5.4. Utah LAM total precipitation during four 6-h time blocks for the 13-day period 27 June to 9 July 1993, as predicted by the reanalysis $w=0$ experiment. Each panel represents a different 6-h block as follows: (a) 0000 to 0600 UTC, (b) 0600 to 1200 UTC, (c) 1200 to 1800 UTC, and (d) 1800 to 2400 UTC. Units are cm and contours are at 1, 5, 10, 20, 30, and 40 cm, with light shading above 5 cm and dark shading above 30 cm.

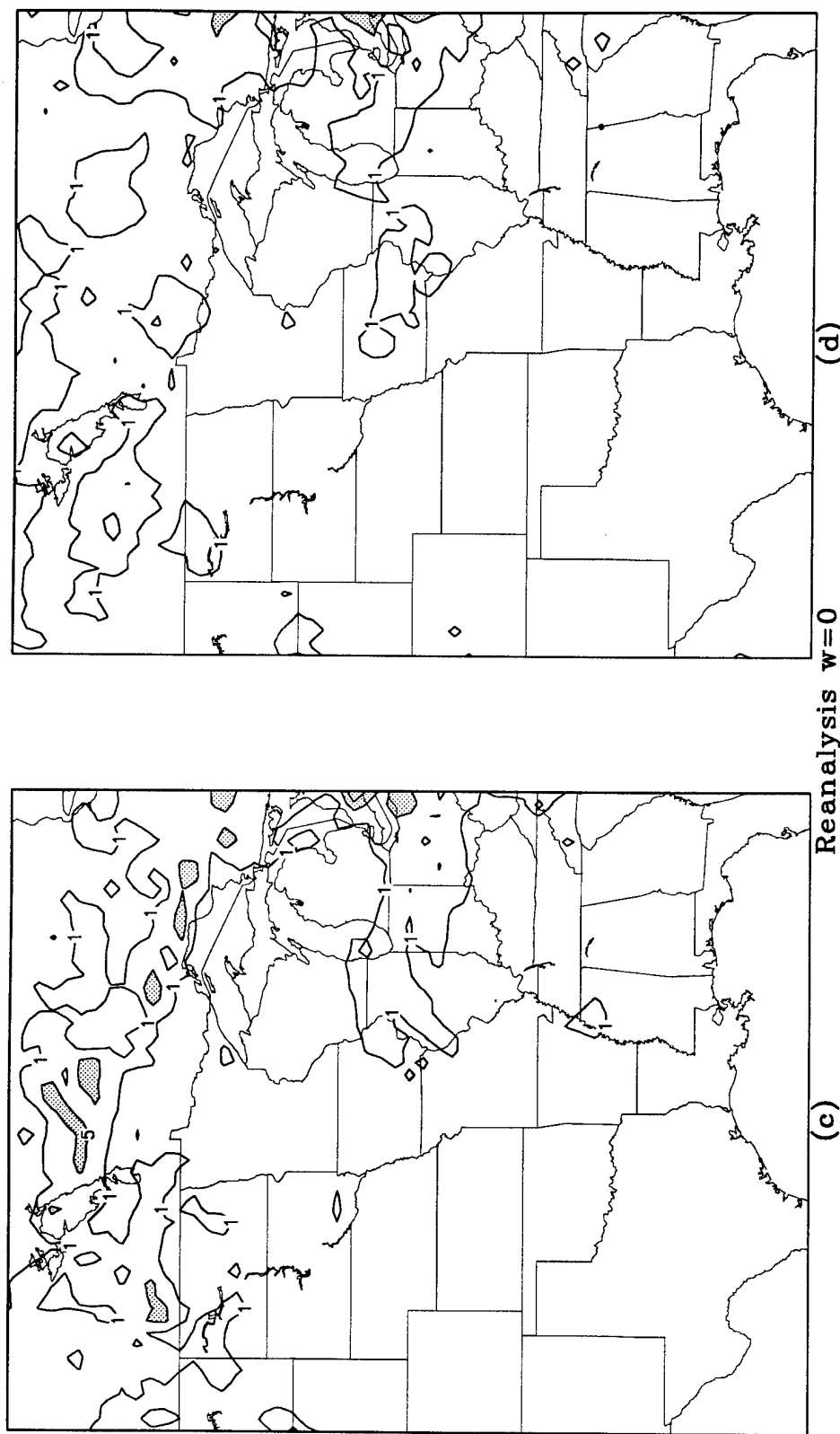


Figure 5.4. (Continued)

maximum rainfall of 18.0 cm in northern Illinois in the reanalysis $w = 0$ experiment compared to 36.5 cm in northern Illinois from the $w = 0$ experiment. Both NGM-bounded simulations ($p' = 0$ and $w = 0$) produced local rainfall maximums in northern Illinois, whereas the two reanalysis experiments did not. Also, the trend for the $p' = 0$ upper boundary condition to produce more precipitation than the $w = 0$ upper boundary condition holds true with either the NGM data set or the reanalysis data set. There is much less rainfall over the southeast for both reanalysis experiments than for the NGM cases. Here the NGM-driven cases agree better with the observed rainfall shown in Figure 3.1.

Similar conclusions may be drawn from examination of the 5 July precipitation fields. Figures 5.1b and 5.3b display the 24-h rainfall for 5 July for the reanalysis $p' = 0$ experiment and the reanalysis $w = 0$ experiment, respectively. Relative to their NGM counterparts, the reanalysis $p' = 0$ experiment provided less rainfall over Wisconsin, in a slightly narrower area, and very similar in location, and the reanalysis $w = 0$ experiment followed a similar trend. More similarities exist between the two $p' = 0$ upper boundary condition experiments and the two $w = 0$ experiments than between the two NGM-bounded simulations and the two reanalysis simulations. This is further illustrated by the eastward shift and substantial decrease of the 5 July precipitation in both of the $w = 0$ experiments (compare Figures 4.6b and 5.3b to Figures 4.1b and 5.1b).

Figures 5.4a-d show the 6-h rainfall for the reanalysis $w = 0$ experiment for the 6 h ending at 0600 UTC, 1200 UTC, 1800 UTC, and 2400 UTC, respectively. The diurnal variation in the reanalysis $w = 0$ simulation is more evident than in the $w = 0$ experiment with the NGM data set shown in Figures 4.7a-d. Rainfall of 10 cm or more was predicted in northeast Missouri between 0600 and 1200 UTC and southeast Iowa between 0000 and 0600 UTC, whereas 2 to 3 cm was predicted during the other two 6-h time periods. Referring back to Figure 4.7 for the $w = 0$ experiment, it is clear that the local 13-day maximum produced in northern Illinois came from rainfall in large part due to the contribution from the 1200 to 1800 UTC and 1800 to 2400 UTC time periods that the

reanalysis $w = 0$ experiment did not produce. Similar conclusions can be made from the output of the two $p' = 0$ experiments (compare Figures 4.2a-d and 5.2a-d).

There is less sensitivity in the precipitation predicted by the Utah LAM over the Upper Mississippi River Basin to the tested upper boundary conditions than to the tested lateral boundary data origins. Analysis of the local model's average 500-m wind over the 13 days exhibited the same correlation (results not shown). Rainfall simulations over northern Illinois and over the southeast show strong sensitivity to origin of boundary conditions.

Lateral Boundary Implementation Method

In this section, sensitivity of the Utah LAM to the method of applying boundary conditions will be analyzed. All previous experiments used Davies nudging applied to the five grid points adjacent to the lateral boundaries in the local model. Those experiments will be used as the baseline to compare new experiments that employ a method of spectral wave relaxation that influences the interior of the LAM domain. The following discussion paraphrases Waldron et al. (1996).

A typical Utah LAM forecast equation can be written schematically as

$$\frac{dQ}{dt} = L(Q), \quad (5.1)$$

where the variable Q may represent a single forecast variable or a vector of forecast variables and $L(Q)$ is the local model representation of the influences contributing to the change in Q .

Juang and Kanamitsu (1994) suggest decomposing Q in a nested regional model into two components as

$$Q = Q_o + Q_i, \quad (5.2)$$

where Q_o represents the scales resolved by the large scale outer model and Q_i represents the smaller scales resolved only by the inner model. Using this in equation (5.1), the forecast equation now becomes

$$\frac{dQ_i}{dt} = L(Q) - L(Q_o). \quad (5.3)$$

The outer model forecast provides the values for $L(Q_o)$, even within the inner model domain. This method is advantageous since $Q = Q_o$ on the local model boundaries resulting in $Q_i = 0$ and a spectral expansion of Q_i is possible due to the resulting periodicity.

The application of Davies nudging in the local model can be expressed by including a nudging term, $-K(Q - Q_o)$, on the right side of equation (5.1):

$$\frac{dQ}{dt} = L(Q) - K(Q - Q_o), \quad (5.4)$$

where K decreases with increasing distance from the lateral boundary. This ensures that the transition to the boundary value is accomplished smoothly. This method has been shown to work well in many models using a one-way interacting boundary condition. Waldron et al. (1996) discuss a modification to this and Juang and Kanamitsu's method which is summarized next.

The wave nudging method available in the Utah LAM allows partial application of the two methods discussed above (Davies and Juang and Kanamitsu) depending on the scale of the forecast field. Equation (5.4) is modified as follows:

$$\frac{dQ}{dt} = L(Q) - \sum_{|m| \leq M''} \sum_{|n| \leq M''} K_{mn} (A_{mn} - A''_{mn}) e^{ik_m x} e^{ik_n y}, \quad (5.5)$$

where M'' is defined as the highest wavenumber (relative to the local model grid) that is well predicted by the outer model, A''_{mn} are the Fourier coefficients of a field that is defined as Q_o within the local model and zero on the boundaries, and A_{mn} are the Fourier coefficients resulting from the solution for Q from the local model with values of zero on the boundary. Equation (5.5) can be used to provide selective relaxation in the wavenumber domain.

If M'' is equal to the local model domain length divided by twice the outer model grid size, and if K_{mn} is sufficiently large, then equation (5.5) will allow the local model fields to be everywhere affected by the outer model. Additionally, if $K_{mn} = 0$ and $L(Q)$ retains Davies nudging as in equation (5.4), then equation (5.5) is equivalent to a one-way interacting boundary condition. If K_{mn} varies with m and n , then the benefits of both methods can be realized by selectively relaxing the longer waves to values forecast by the outer model and allowing the local model to predict the shorter waves. This can be done by setting K_{mn} to a large value for the long waves ($m, n \ll M''$) and to a small value for the short waves ($m, n \approx M''$).

This method of spectral relaxing may be superior to boundary nudging alone because it allows some scales within the Utah LAM to be better predicted by the outer model. Waldron et al. (1996) discuss the results of tests with three different spectral relaxation schemes generated by the Utah LAM. Since the local model grid size, terrain, and boundary layer resolution are significantly different than the outer model, the relaxation is applied to the LAM domain above the 3-km model level and is applied only to wind forecasts. Implementation of spectral relaxation in the Utah LAM is flexible in that a choice can be made of which wavenumbers to relax. For example, wavenumber 0 only, wavenumbers 0 and 1, waves 0, 1, and 2, and so on. Also, previous experiments testing this spectral relaxation method in the Utah LAM were for shorter simulations (see Waldron et al. 1996) than used in this research, and the results of the 13-day simulations are analyzed below.

Six experiments were performed to examine model sensitivity to the degree of spectral relaxation. In two of the simulations, only wavenumber 0 (the LAM domain average) is relaxed in order to produce a subtle influence on the LAM interior. These experiments differ in the choice of upper boundary condition and are hereafter referred to as the wave 0 $p' = 0$ experiment and the wave 0 $w = 0$ experiment. In the second pair of simulations, waves 0 and 1 are relaxed in order to provide a greater response. Similarly, these experiments are called the wave 1 $p' = 0$ experiment and the wave 1 $w = 0$ experiment. The final pair of experiments were performed with relaxation of waves 0, 1, and 2 and are referred to as the wave 2 $p' = 0$ experiment and the wave 2 $w = 0$ experiment.

In all cases the relaxation coefficient, K_{mn} , was set to $1/(40\Delta t)$, where Δt is the model time step. The resulting adjustment of relaxed waves occurs on a rapid time scale of 1 h. The NGM supplied the outer model information for these six experiments.

Wave 0 Relaxation

Figures 5.5 and 5.6 display the results of the wave 0 $p' = 0$ experiment in the same manner as Figures 4.1 and 4.2 for the $p' = 0$ experiment. The 13-day precipitation predicted by the wave 0 $p' = 0$ case (Figure 5.5a) is very similar to the non-relaxed case (Figure 4.1a). The LAM continues to produce a rainfall maximum in eastern Iowa and northern Illinois that is greater than observed (55.2 cm in this case), the dry area from Texas to Kentucky, and an under-prediction of precipitation in Kansas, Nebraska, South Dakota, and Minnesota. However, the wave 0 $p' = 0$ experiment generated 3 to 4 cm of rain in southern Kansas and 5 cm in southeast Nebraska that the nonrelaxed case did not and slightly increased the precipitation in northern Minnesota.

Figure 5.5b shows the 24-h rainfall predicted for 5 July for the wave 0 $p' = 0$ simulation. This experiment predicted precipitation of 5 cm from northeast Iowa through most of Wisconsin, and the 10-cm contour is in good agreement with the station data in

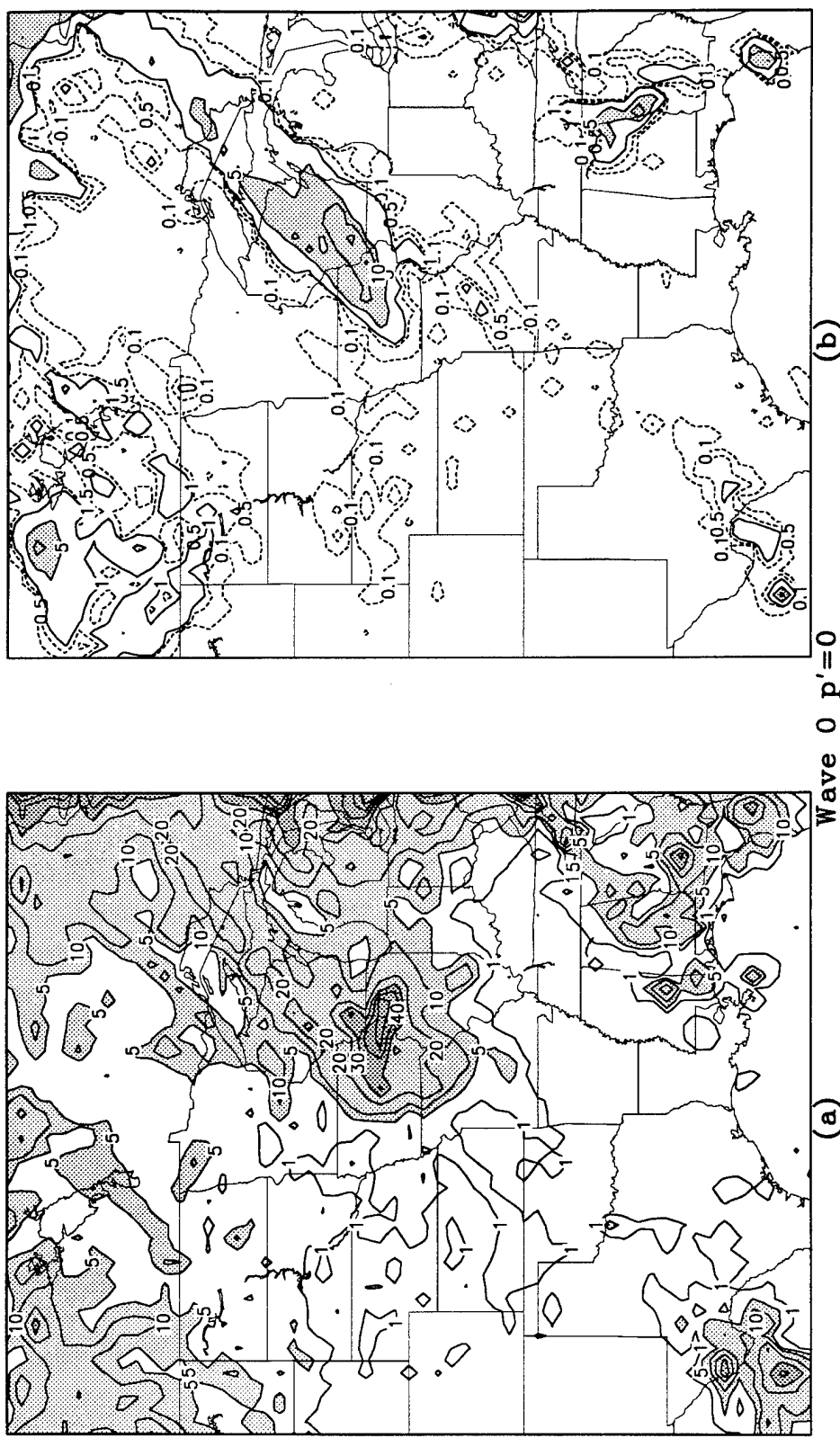


Figure 5.5. Utah LAM output from the wave 0 $p' = 0$ experiment: (a) 13-day total rainfall predicted for 0600 UTC 27 June to 0600 UTC 10 July, (b) 24-h rainfall predicted for 5 July. In (a), contours are for 1, 5, 10, 20, 30, 40, 50, and 60 cm, with light shading above 5 cm and dark shading above 30 cm. In (b), contours are dashed for 0.1 and 0.5 cm and solid for 1, 5, 10, and 20 cm, with shading above 5 cm.

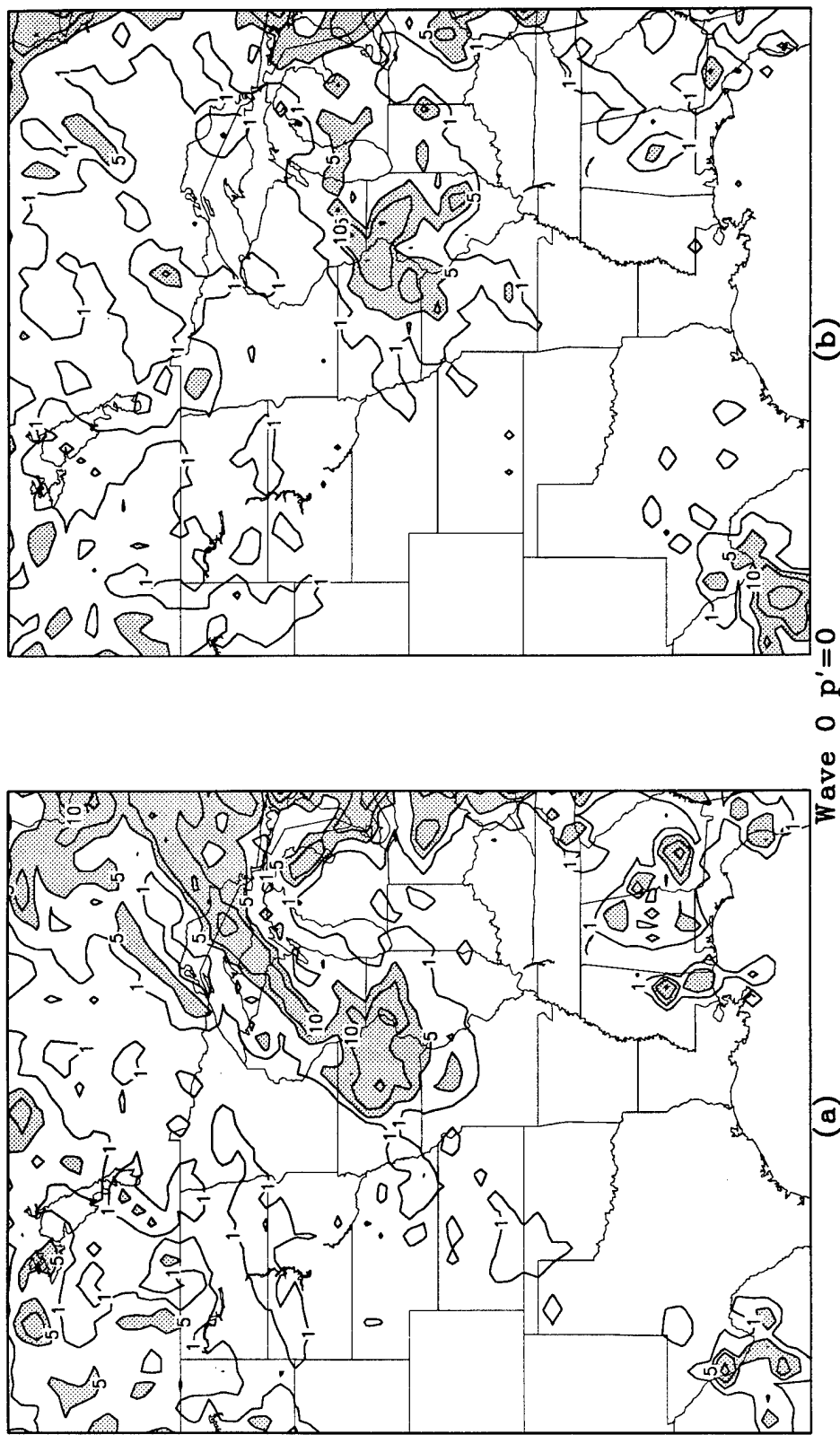


Figure 5.6. Utah LAM total precipitation during four 6-h time blocks for the 13-day period 27 June to 9 July 1993, as predicted by the wave 0 $p' = 0$ experiment. Each panel represents a different 6-h block: (a) 0000 to 0600 UTC, (b) 0600 to 1200 UTC, (c) 1200 to 1800 UTC, and (d) 1800 to 2400 UTC. Units are cm and contours are at 1, 5, 10, 20, 30, and 40 cm, with light shading above 5 cm and dark shading above 30 cm.

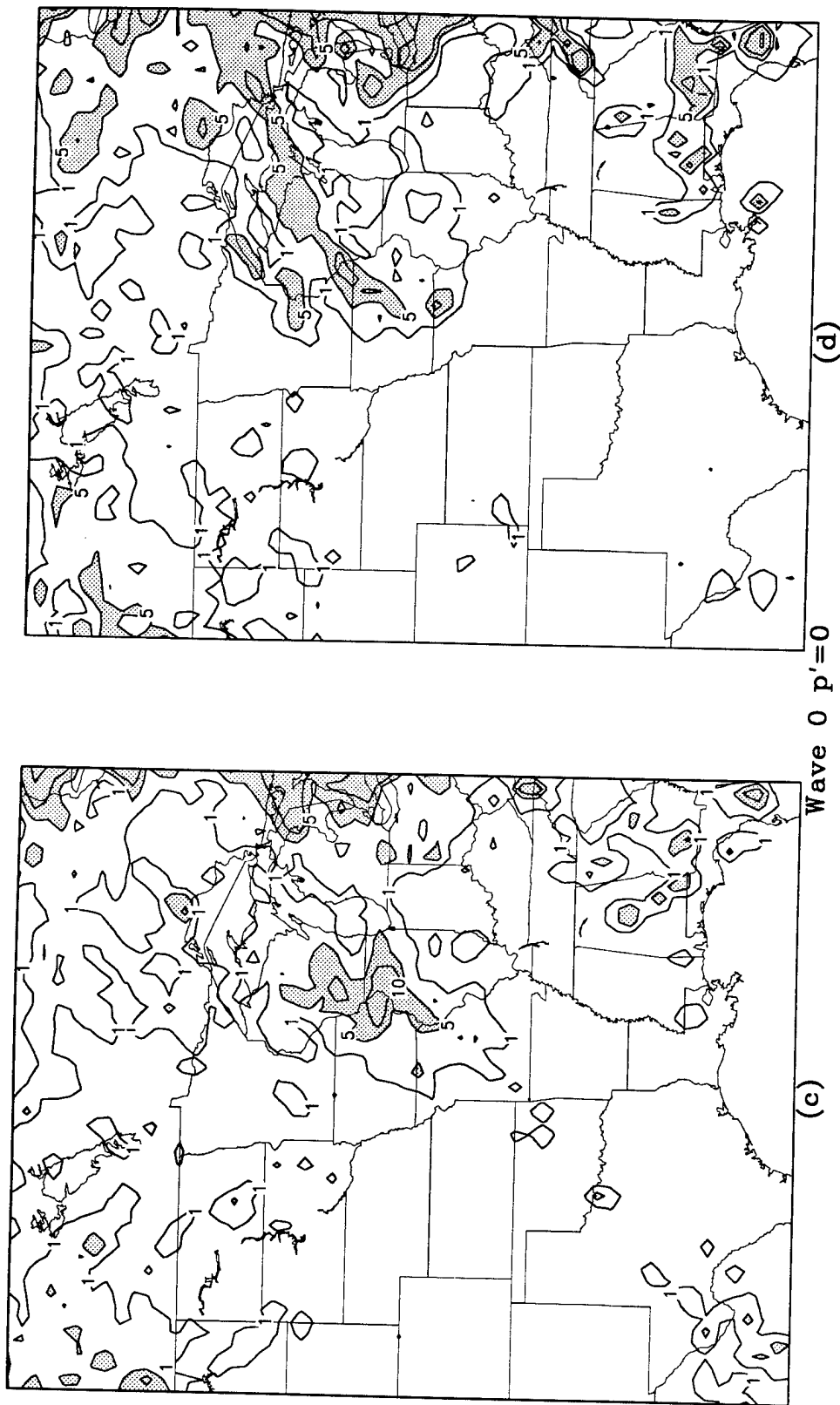


Figure 5.6. (Continued)

Figure 3.1b. For this case, the maximum was increased to 22.5 cm (in southeast Wisconsin) compared to 13.3 cm for the nonrelaxed case.

The diurnal precipitation cycle is basically unchanged with the most rainfall predicted to occur between 0000 UTC and 1200 UTC (Figures 5.6a-d). Figure 5.6a shows that nearly all of the precipitation generated over southern Kansas and southeast Nebraska (which was not produced in the nonrelaxed case) occurred during the 6-h period between 0000 and 0600 UTC. The representation of the LLJ also showed little change with the wave 0 relaxation. The average 500-m winds from the wave 0 $p' = 0$ experiment showed the same general orientation, but with slightly slower speeds in the jet exit region (Wisconsin and Michigan), as the case without relaxation (results of wave 0 $p' = 0$ not shown, see Figure 4.3 for the nonrelaxed case).

In general, the relaxation of wave 0 had little affect on the 13-day rainfall amounts and the diurnal variation of precipitation and the LLJ. Although the output for 5 July is also very similar in these two cases, examination of the daily precipitation showed numerous differences on several days (results not shown). This suggests that the wave 0 relaxation had a slightly stronger influence on the precipitation output from the LAM than would be inferred from comparison of Figures 4.1 and 5.5.

The wave 0 $w = 0$ experiment results are displayed in Figures 5.7 and 5.8 and are compared to the nonrelaxed $w = 0$ case shown in Figures 4.6 and 4.7. Figure 5.7a shows that the coverage of the 5-cm contour has been significantly reduced in this experiment and two local maximums of 26.1 and 25.3 cm were generated in southeast Iowa and northern Illinois, respectively. This is in comparison to the 5-cm contour and the 36.5 cm maximum in Illinois displayed in Figure 4.6a for the nonrelaxed case. Other differences include somewhat greater precipitation over parts of the Gulf Coast, a slight increase in rainfall over northern Minnesota (as in the wave 0 $p' = 0$ case), and 1 to 2 cm in parts of southern Kansas.

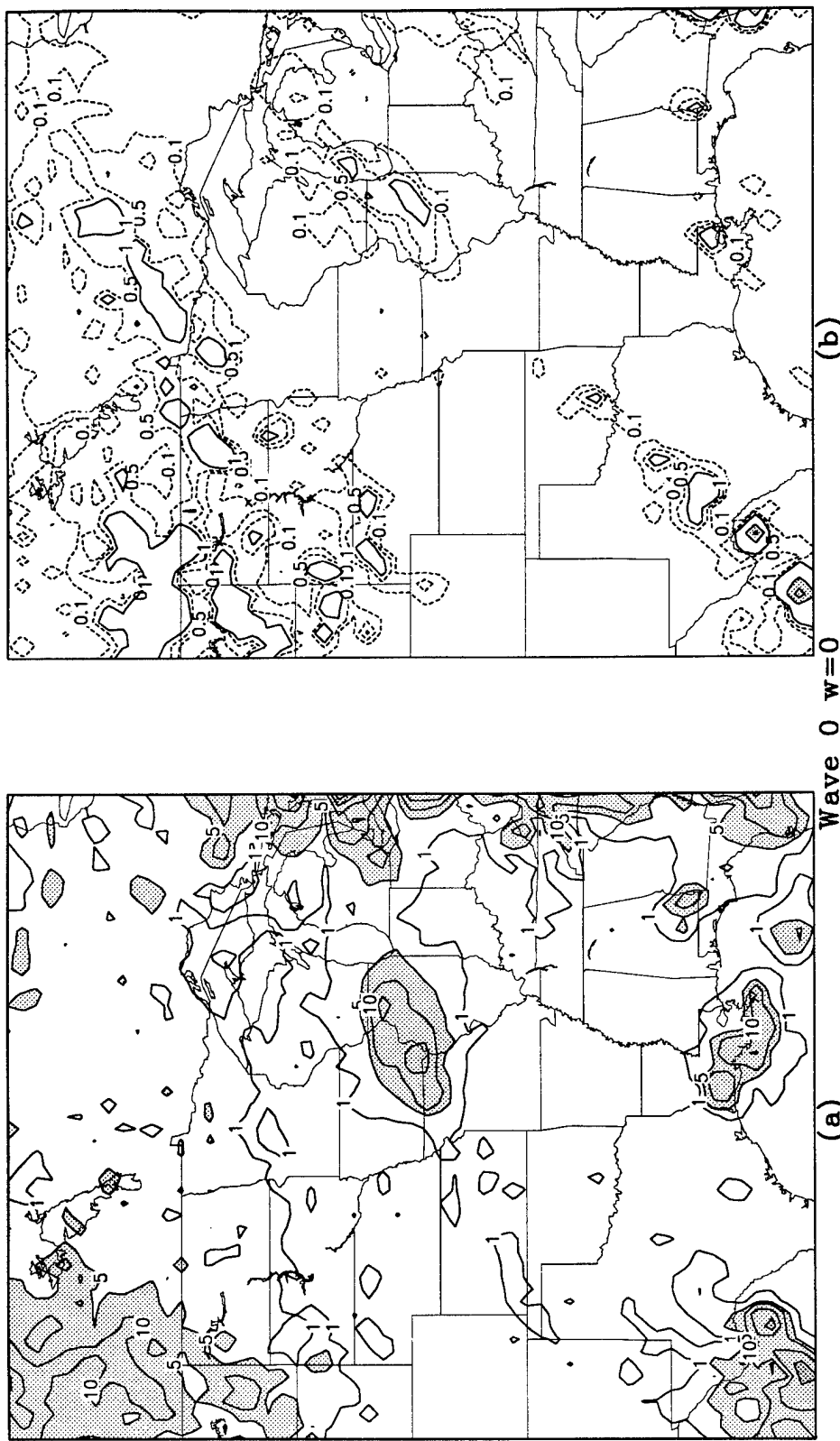


Figure 5.7. Utah LAM output from the wave 0 $w=0$ experiment: (a) 13-day total rainfall predicted for 0600 UTC 27 June to 0600 UTC 10 July, (b) 24-h rainfall predicted for 5 July. In (a), contours are for 1, 5, 10, 20, 30, 40, 50, and 60 cm, with light shading above 5 cm and dark shading above 30 cm. In (b), contours are dashed for 0.1 and 0.5 cm and solid for 1, 5, 10, and 20 cm, with shading above 5 cm.

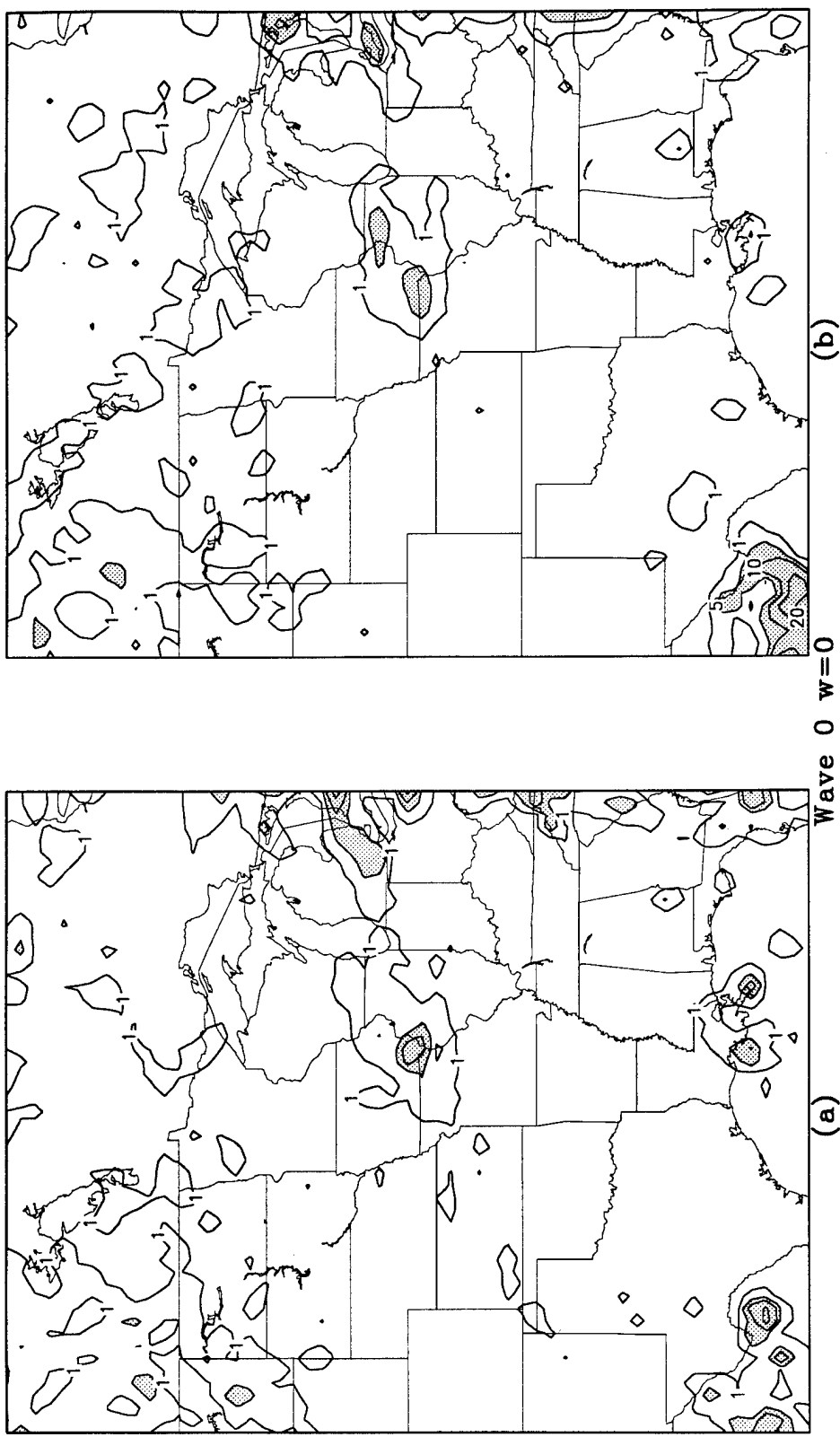


Figure 5.8. Utah LAM total precipitation during four 6-h time blocks for the 13-day period 27 June to 9 July 1993, as predicted by the wave 0 $w = 0$ experiment. Each panel represents a different 6-h block: (a) 0000 to 0600 UTC, (b) 0600 to 1200 UTC, (c) 1200 to 1800 UTC, and (d) 1800 to 2400 UTC. Units are cm and contours are at 1, 5, 10, 20, 30, and 40 cm, with light shading above 5 cm and dark shading above 30 cm.

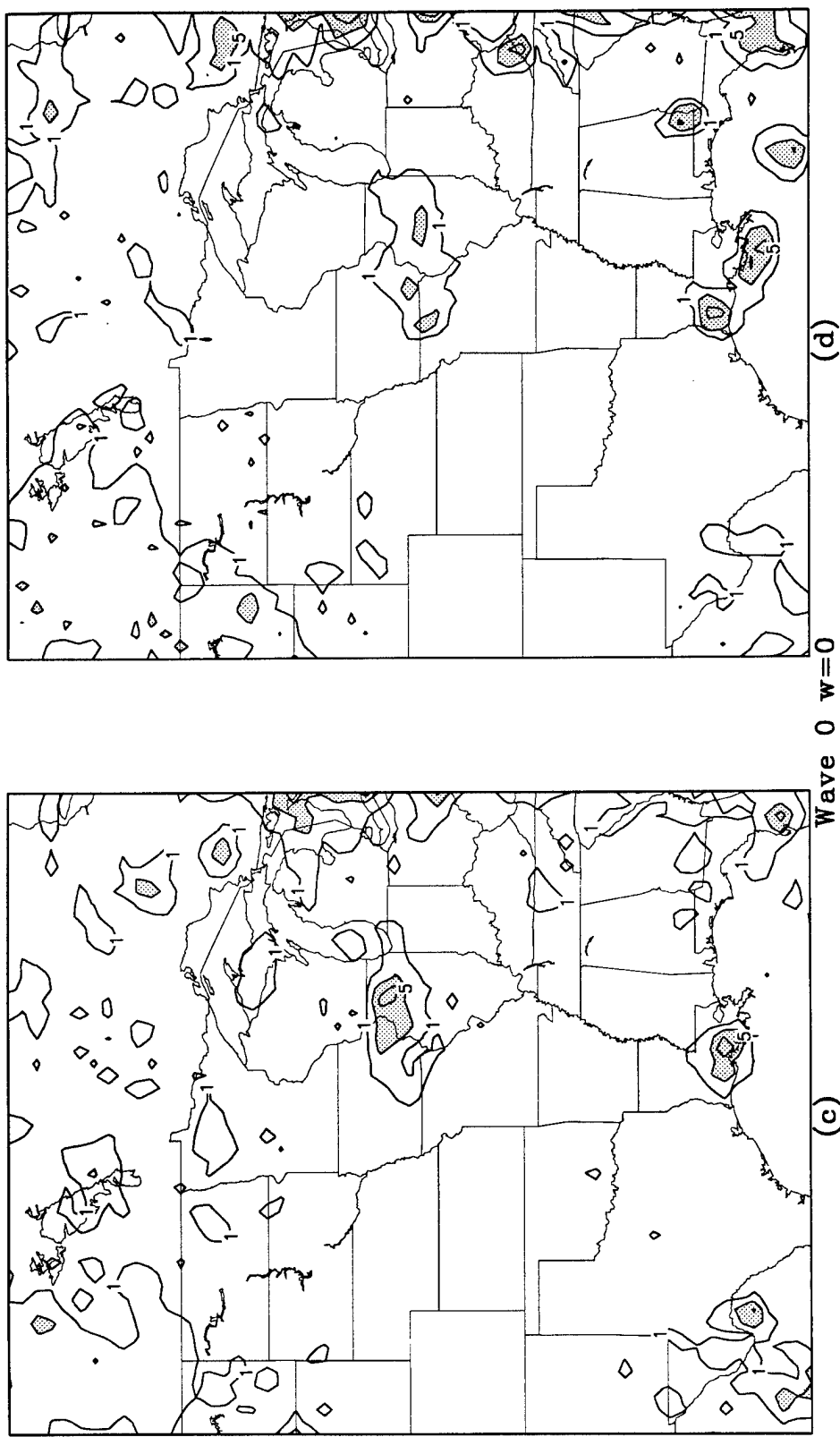


Figure 5.8. (Continued)

For 5 July, Figure 5.7b illustrates a significant change to the 24-h rainfall predicted by this experiment when compared to the nonrelaxed experiment shown in Figure 4.6b. The wave 0 relaxation reduced the precipitation over Wisconsin and Michigan to little more than 1 cm and the area shifted to the southeast. This case also generated numerous isolated areas of 2 to 3 cm rainfall over eastern Montana and the Dakotas, and a few areas of 1 cm rain in central Texas.

Figure 5.8 shows no change in the diurnal variation of the precipitation, and the result of the wave 0 relaxation was only a slight decrease in the speed of the average 500-m winds (500-m winds not shown).

In general, the wave 0 relaxation had a more pronounced affect on the Utah LAM precipitation forecast with the $w = 0$ upper boundary condition than the $p' = 0$ condition. Although the wave 0 relaxation had a stronger influence on the location and amounts of rainfall on a day-to-day analysis for both upper boundary conditions (results not shown), the 13-day totals and the diurnal cycle of precipitation and the LLJ were less affected.

Wave 1 Relaxation

Figures 5.9 and 5.10 show the precipitation fields from the wave 1 $p' = 0$ case and Figures 5.11 and 5.12 show the results of the wave 1 $w = 0$ case. These figures are configured as all previous illustrations of the 13-day, 5 July, and diurnal variation of precipitation. Figures showing the 500-m wind fields are omitted since the spectral wave relaxation has little influence on the low-level winds.

The 13-day rainfall total from the wave 1 $p' = 0$ experiment (Figure 5.9a) decreased from that predicted by the wave 0 experiment, as shown by the 15 and 20 cm contours. Also, one grid point in Illinois received more than 30 cm in this experiment (compared to 55.2 cm in the wave 0 case and 57.1 cm in the nonrelaxed case), and the maximum in Iowa was 46.4 cm (compared to 50+ cm in the wave 0 case and 50.9 cm in the non-relaxed case). The general trend remains unchanged: dry area through Texas to

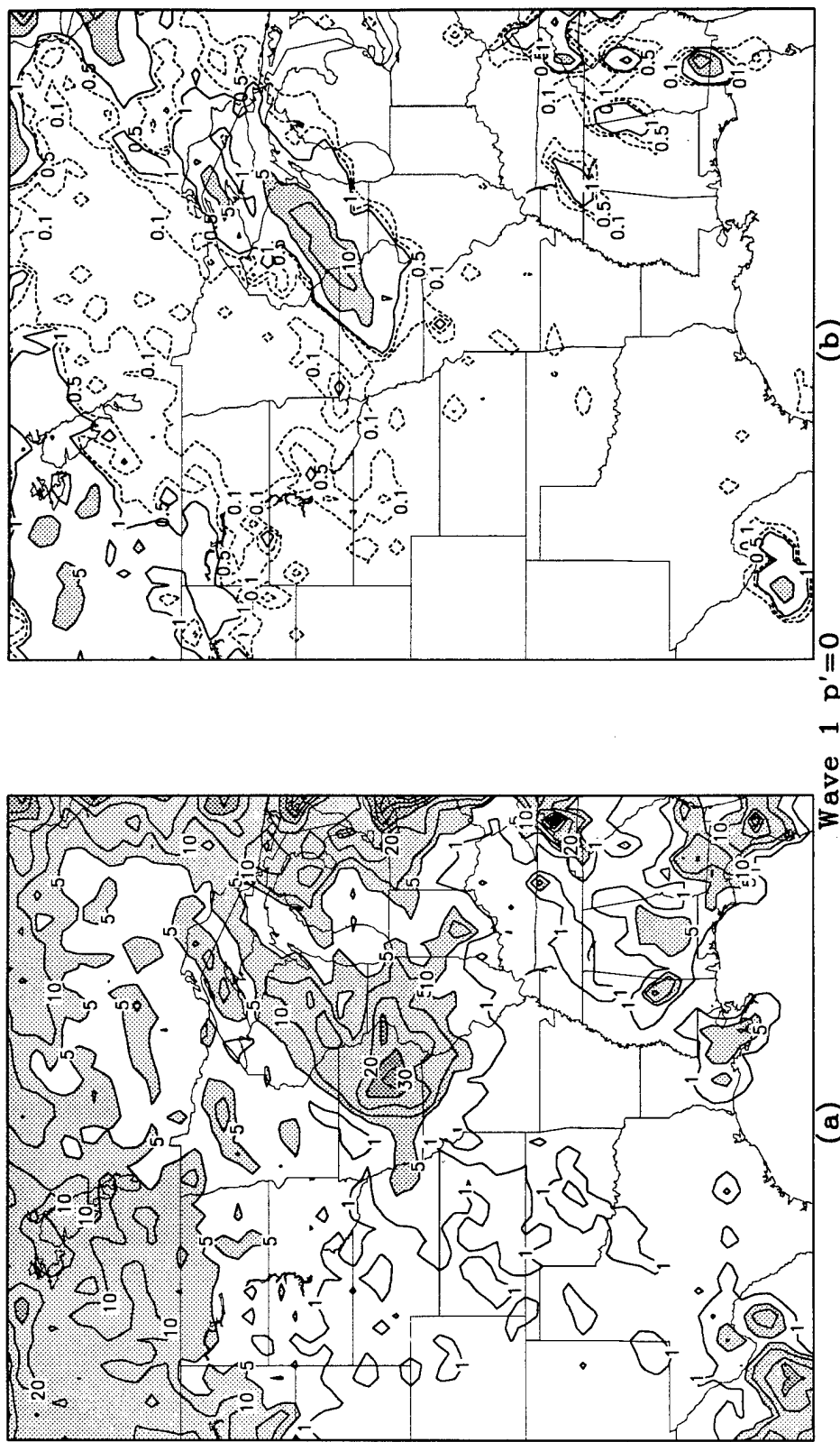


Figure 5.9. Utah LAM output from the wave 1 $p'=0$ experiment: (a) 13-day total rainfall predicted for 0600 UTC 27 June to 0600 UTC 10 July, (b) 24-h rainfall predicted for 5 July. In (a), contours are for 1, 5, 10, 20, 30, 40, 50, and 60 cm, with light shading above 5 cm and dark shading above 30 cm. In (b), contours are dashed for 0.1 and 0.5 cm and solid for 1, 5, 10, and 20 cm, with shading above 5 cm.

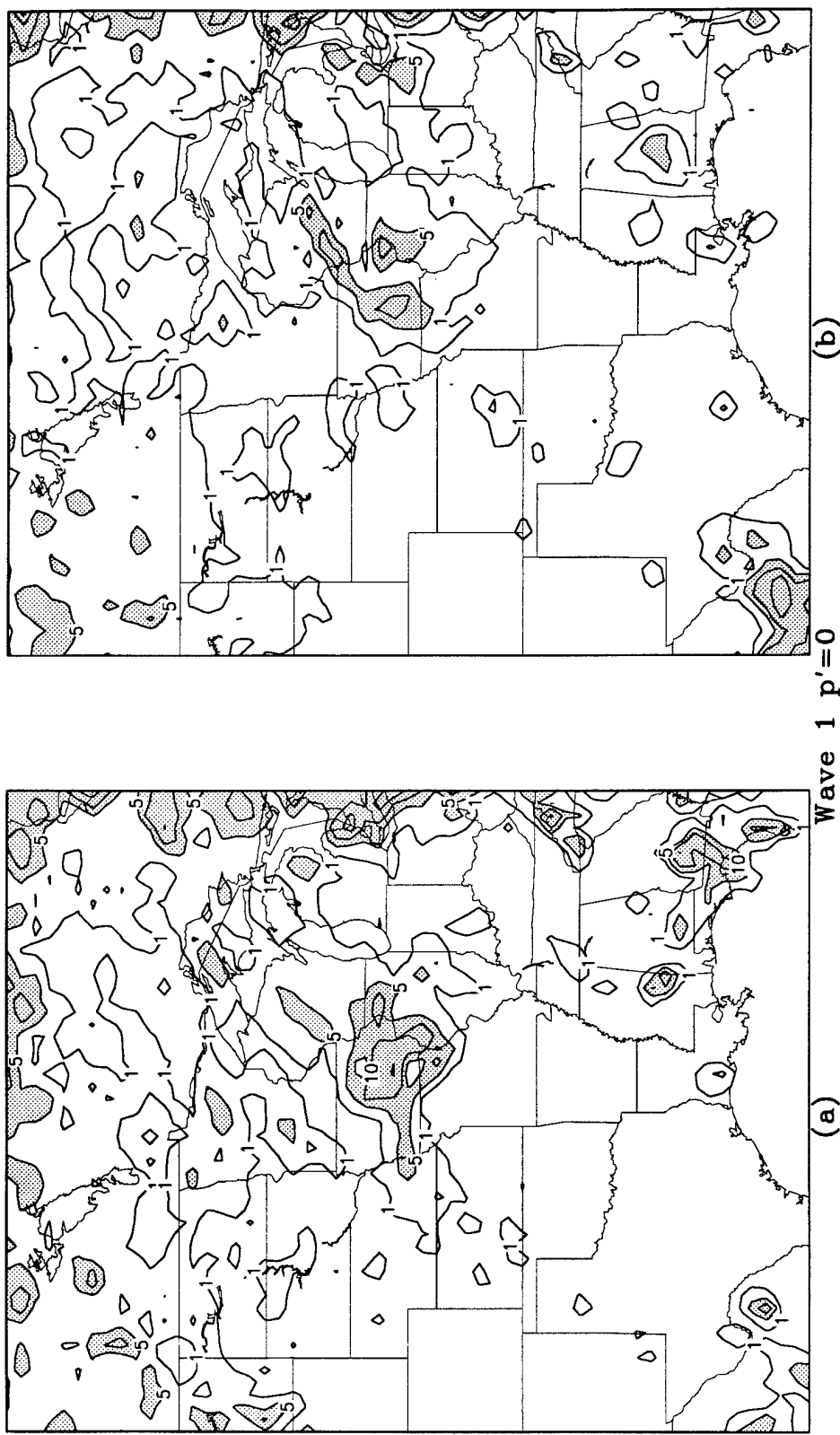


Figure 5.10. Utah LAM total precipitation during four 6-h time blocks for the 13-day period 27 June to 9 July 1993, as predicted by the wave 1 $p' = 0$ experiment. Each panel represents a different 6-h block: (a) 0000 to 0600 UTC, (b) 0600 to 1200 UTC, (c) 1200 to 1800 UTC, and (d) 1800 to 2400 UTC. Units are cm and contours are at 1, 5, 10, 20, 30, and 40 cm, with light shading above 5 cm and dark shading above 30 cm.

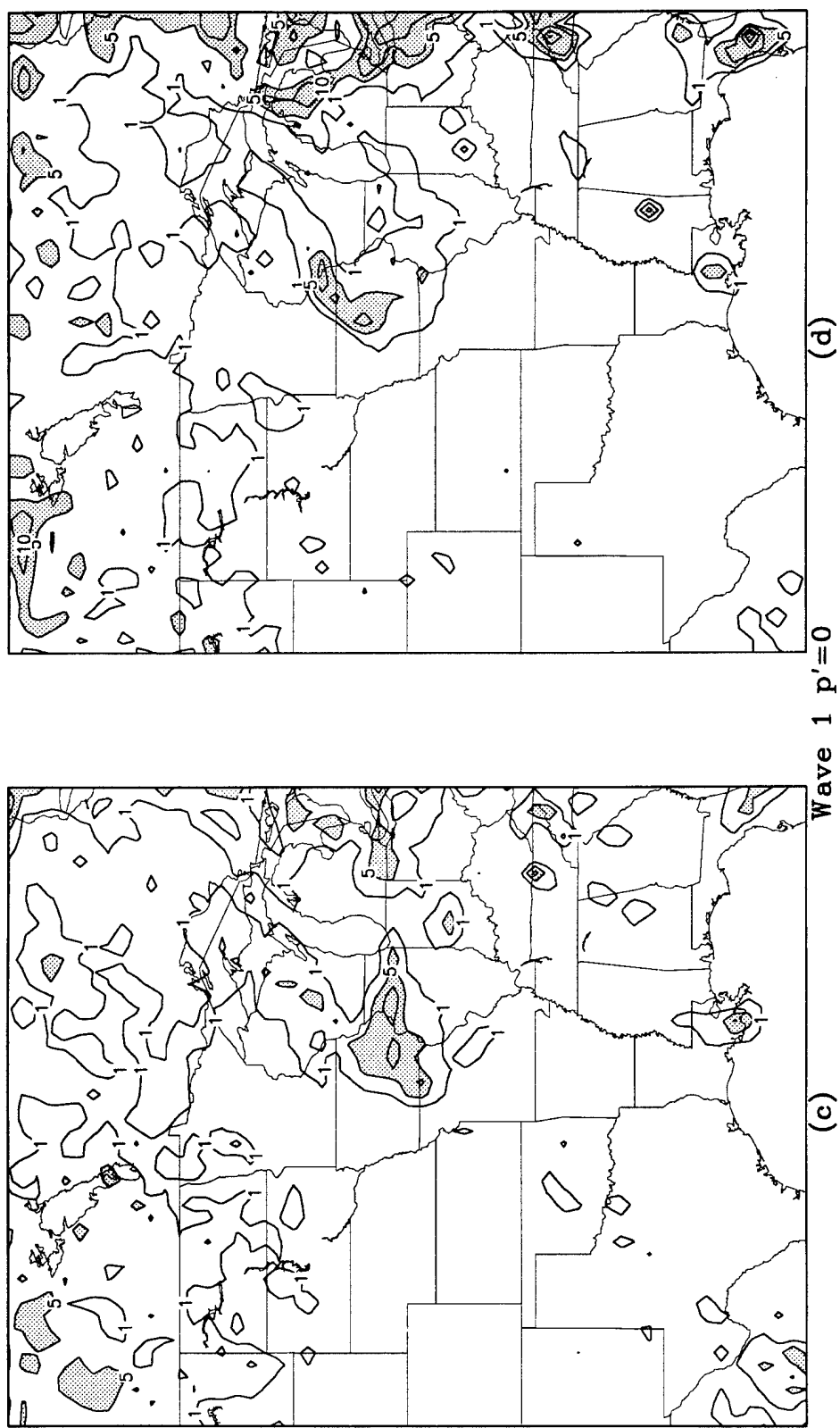


Figure 5.10. (Continued)

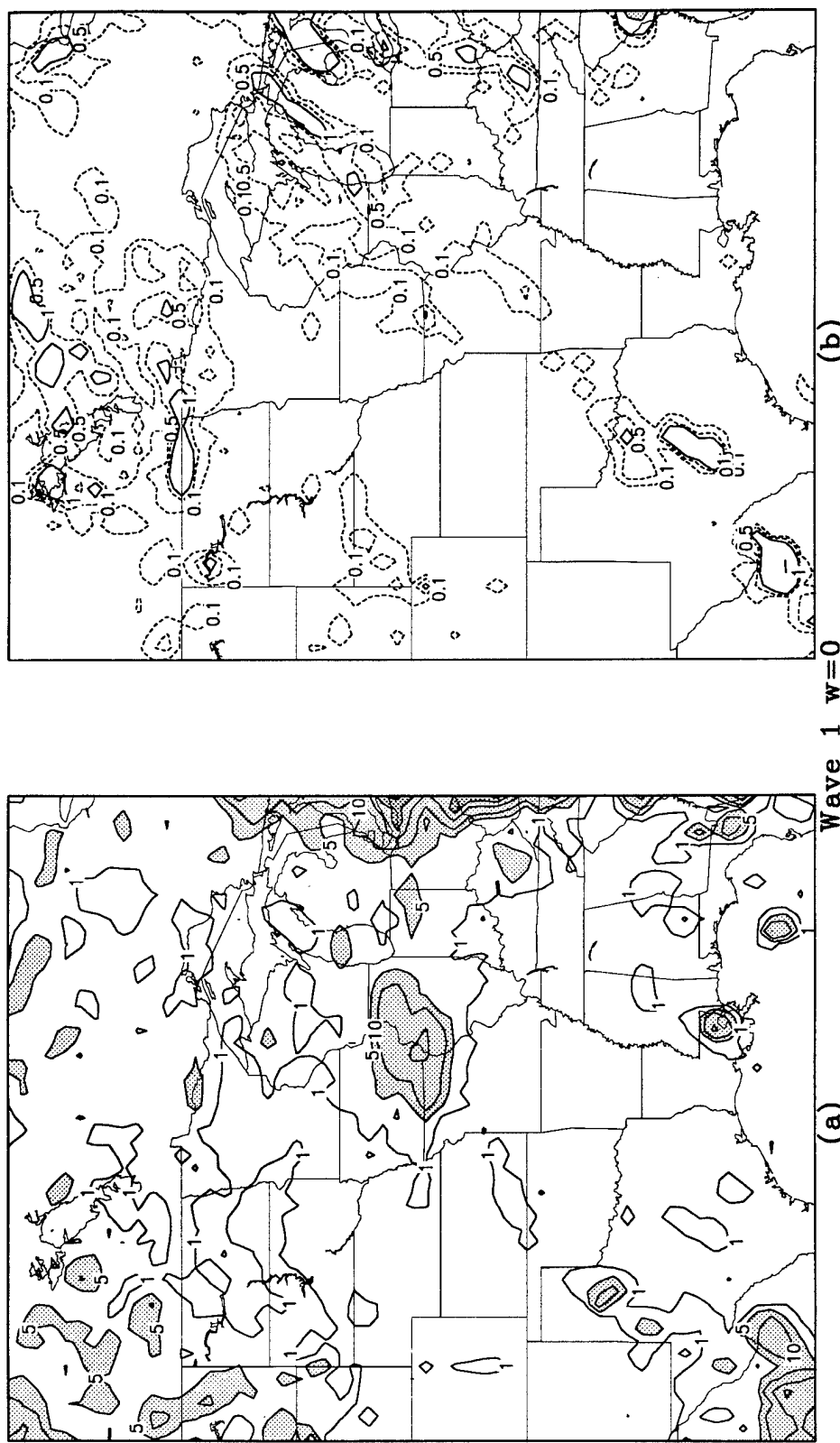


Figure 5.11. Utah LAM output from the wave 1 $w=0$ experiment: (a) 13-day total rainfall predicted for 0600 UTC 27 June to 0600 UTC 10 July, (b) 24-h rainfall predicted for 5 July. In (a), contours are for 1, 5, 10, 20, 30, 40, 50, and 60 cm, with light shading above 5 cm and dark shading above 30 cm. In (b), contours are dashed for 0.1 and 0.5 cm and solid for 1, 5, 10, and 20 cm, with shading above 5 cm.

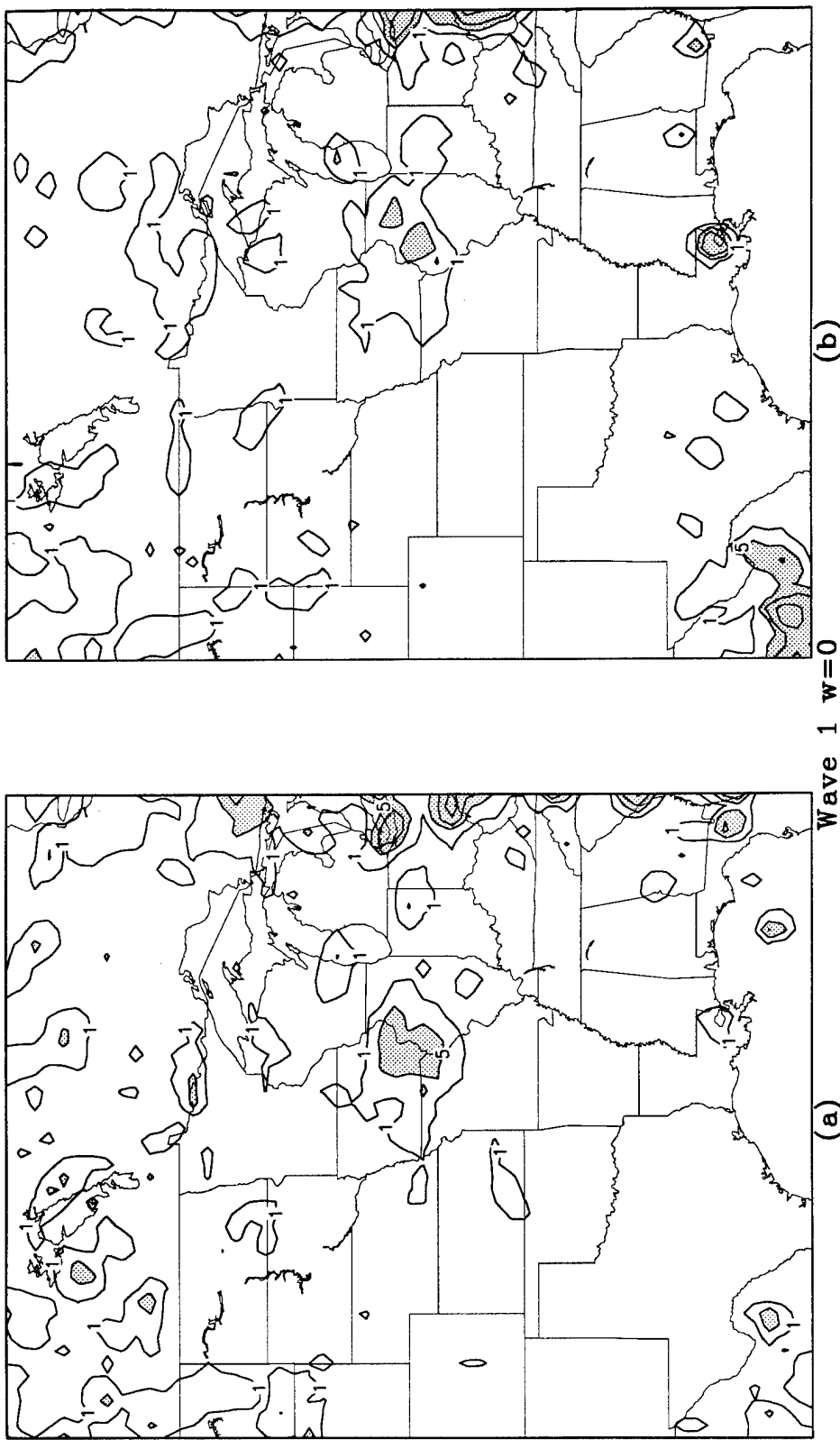


Figure 5.12. Utah LAM total precipitation during four 6-h time blocks for the 13-day period 27 June to 9 July 1993, as predicted by the wave 1 $w = 0$ experiment. Each panel represents a different 6-h block: (a) 0000 to 0600 UTC, (b) 0600 to 1200 UTC, (c) 1200 to 1800 UTC, and (d) 1800 to 2400 UTC. Units are cm and contours are at 1, 5, 10, 20, 30, and 40 cm, with light shading above 5 cm and dark shading above 30 cm.

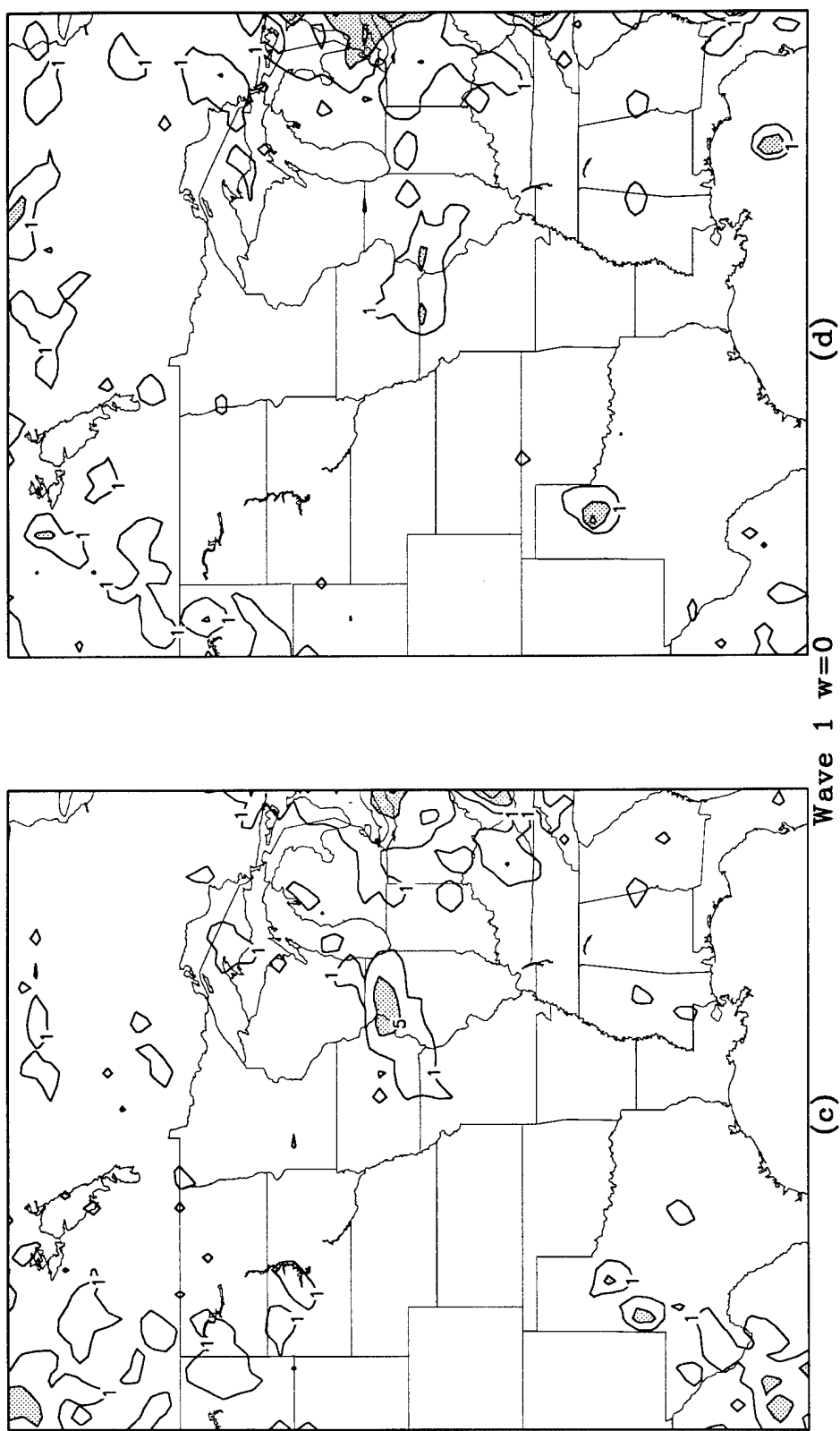


Figure 5.12. (Continued)

Kentucky and underprediction of precipitation in Kansas, Nebraska, and Minnesota. However, this experiment did generate an increased amount of rainfall in North Dakota and Minnesota.

The 24-h rainfall for 5 July (Figure 5.9b) predicted by this experiment continues to be in agreement with the station data, but the maximum in southeast Wisconsin is still too large at 18.3 cm. This is down from 22.5 cm in the wave 0 case and greater than the 17.0 cm in the nonrelaxed case. The diurnal precipitation pattern (Figure 5.10) is as the previous case with the exception that the 6-h block between 0000 and 0600 UTC appears to be picking up most of the rainfall and dominating the daily cycle in eastern Iowa. The diurnal cycle of the 500-m winds is basically unchanged; again the wind speeds are slightly slower (results not shown).

The 13-day total precipitation for the wave 1 $w = 0$ case (Figure 5.11a) is also less than the wave 0 case. The maximum amount is now along the southern border of Iowa and Illinois with a value of 21.5 cm (down from 26.1 cm in the wave 0 experiment and 36.5 in the nonrelaxed experiment). This case shows no improvement to the lack of rainfall in Kansas, Nebraska, the Dakotas, and Minnesota. For 5 July, this experiment shows even more deterioration of the rainband in Wisconsin and Michigan (Figure 5.11b) to a point that it no longer resembles the observed station data presented in Figure 3.1b. Figure 5.12 shows no change to the diurnal precipitation pattern and the 500-m winds are nearly unchanged from the wave 0 case (results not shown).

Whereas the $p' = 0$ upper boundary condition experiments showed little effect from the change to wave 0 relaxation from no relaxation, the change to wave 1 relaxation produced a more visible effect on the LAM-generated 13-day rainfall in the Upper Mississippi River Basin. On the contrary, the $w = 0$ experiments reflected a stronger influence on the predicted rainfall when changing to the wave 0 relaxation from no relaxation, than did changing to wave 1 relaxation from wave 0 relaxation.

Wave 2 Relaxation

The Utah LAM results from the wave 2 relaxation cases are provided in Figures 5.13 and 5.14 for the $p' = 0$ upper boundary condition, and Figures 5.15 and 5.16 for the $w = 0$ upper boundary condition, as done for the previous experiment.

Some of the gains made in the 13-day rainfall in parts of Minnesota, the Dakotas, and Kansas from increasing the spectral relaxation to the wave 1 $p' = 0$ experiment were lost with the wave 2 $p' = 0$ experiment (Figure 5.13a). Precipitation decreased again in northern Illinois, and the maximum in Iowa is now down to 43.2 cm (however, this is still higher than observed). More noteworthy is the significant decrease in the amount of rain generated over Wisconsin and northeast Iowa for 5 July, as shown in Figure 5.13b. The maximum value predicted by the wave 2 $p' = 0$ experiment is down to 7.0 cm from the 18.3 cm predicted in the wave 1 $p' = 0$ case.

The 0000 to 0600 UTC time block dominates the diurnal precipitation pattern in this experiment (Figure 5.14) as noted in the wave 1 $p' = 0$ experiment. Similar to the previous experiments, the change to wave 2 relaxation had little effect on the 500-m winds (results not shown).

Figure 5.15 displays the 13-day rainfall and 5 July rainfall for the wave 2 $w = 0$ simulation. The maximum in the 13-day total in southeast Iowa (Figure 5.15a) has increased to 33.2 cm; otherwise little change is seen between this and the previous experiments involving wave relaxation. What little precipitation was generated in Kansas in the earlier $w = 0$ cases is now isolated to northeast Kansas and scattered across Missouri. For 5 July, the trend for the wave relaxation on the $w = 0$ cases has been to decrease the precipitation in Wisconsin. Figure 5.15b shows that virtually no rain was generated in Wisconsin on 5 July from the wave 2 $w = 0$ experiment.

Whereas the wave relaxation on the $p' = 0$ cases has increased the dominance of the diurnal rainfall to the 0000 to 0600 UTC time block, Figure 5.16 shows that the wave 2

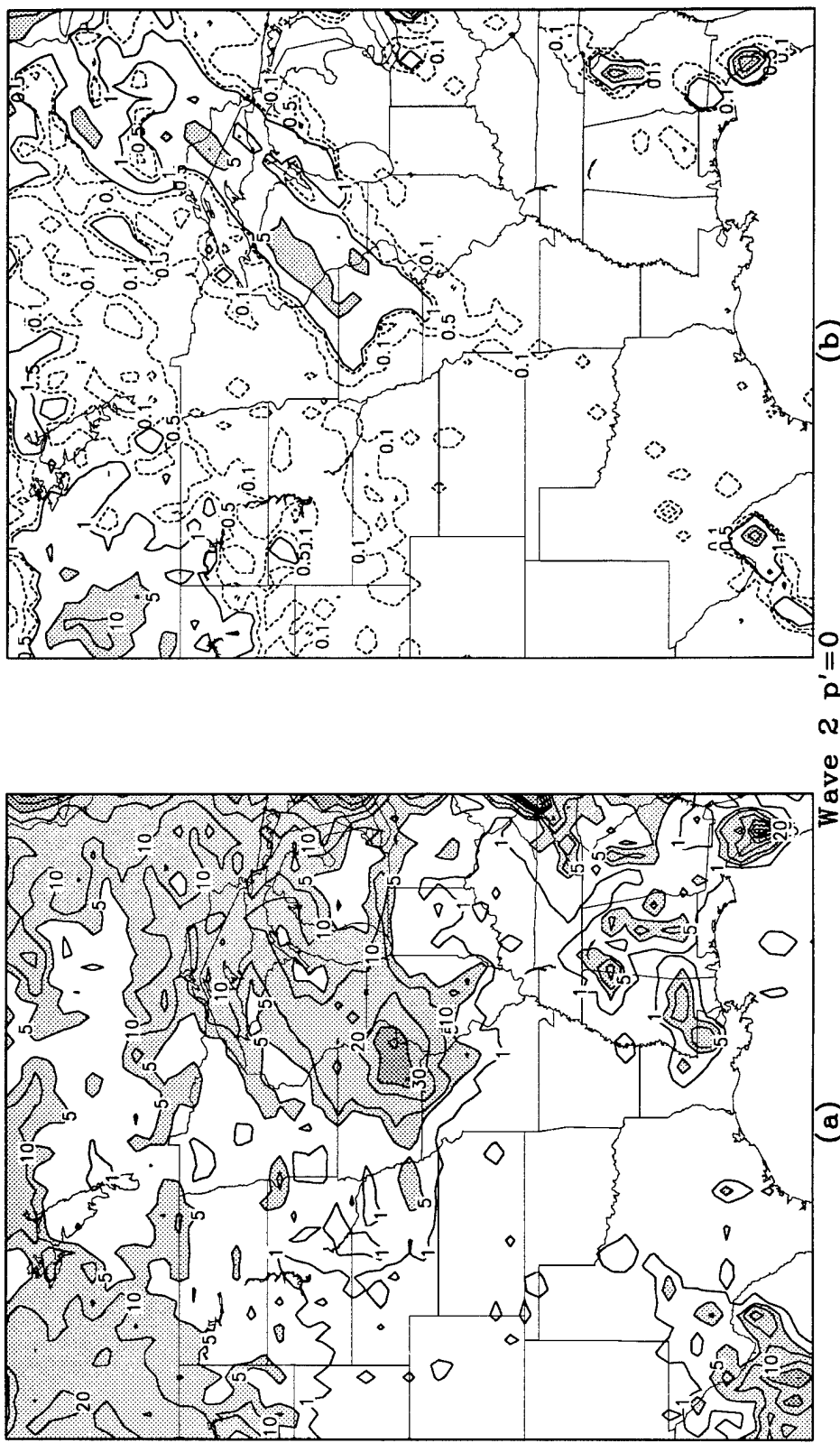


Figure 5.13. Utah LAM output from the wave 2 $p' = 0$ experiment: (a) 13-day total rainfall predicted for 0600 UTC 27 June to 0600 UTC 10 July, (b) 24-h rainfall predicted for 5 July. In (a), contours are for 1, 5, 10, 20, 30, 40, 50, and 60 cm, with light shading above 5 cm and dark shading above 30 cm. In (b), contours are dashed for 0.1 and 0.5 cm and solid for 1, 5, 10, and 20 cm, with shading above 5 cm.

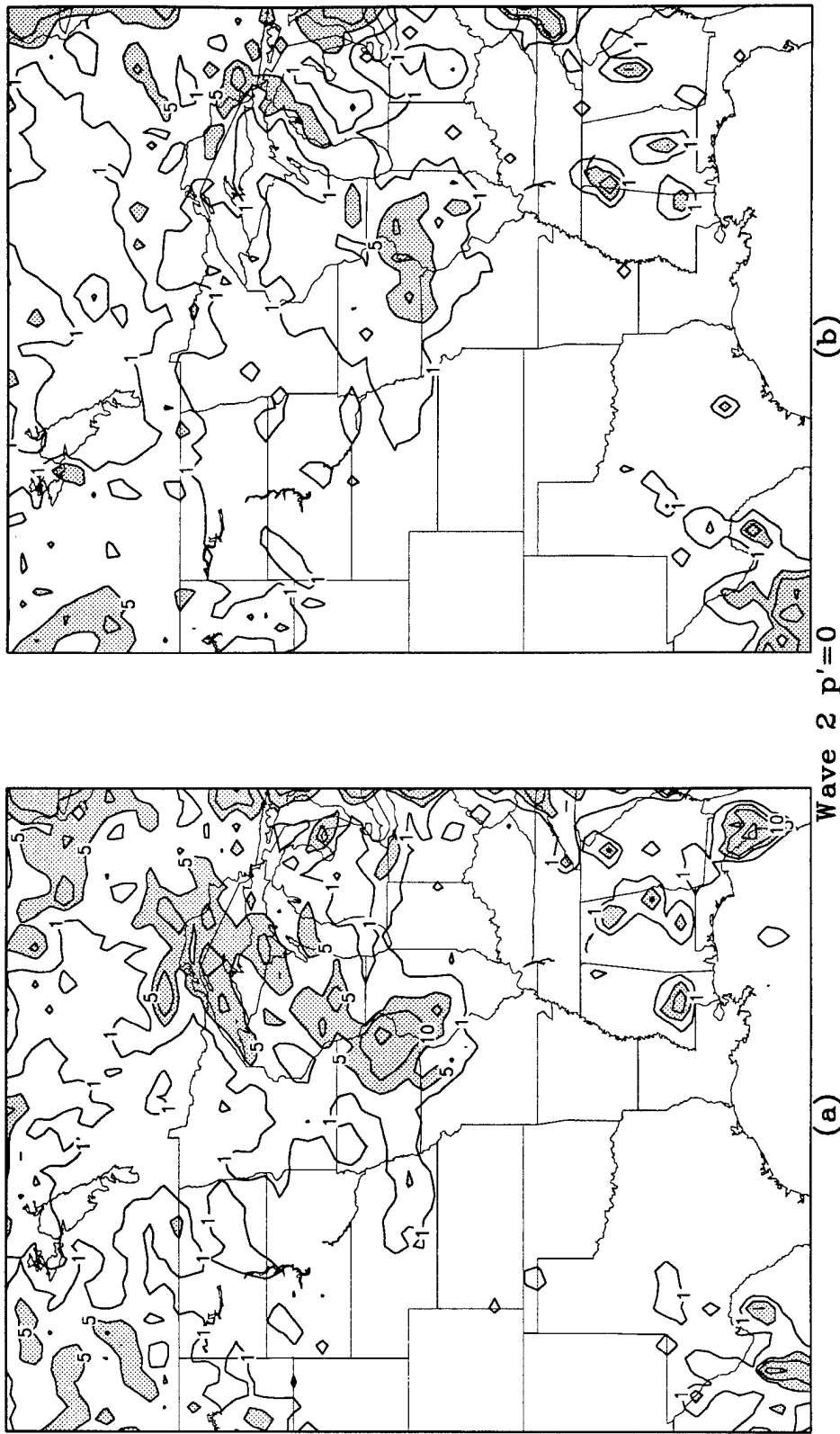


Figure 5.14. Utah LAM total precipitation during four 6-h time blocks for the 13-day period 27 June to 9 July 1993, as predicted by the wave 2 $p' = 0$ experiment. Each panel represents a different 6-h block: (a) 0000 to 0600 UTC, (b) 0600 to 1200 UTC, (c) 1200 to 1800 UTC, and (d) 1800 to 2400 UTC. Units are cm and contours are at 1, 5, 10, 20, 30, and 40 cm, with light shading above 5 cm and dark shading above 30 cm.

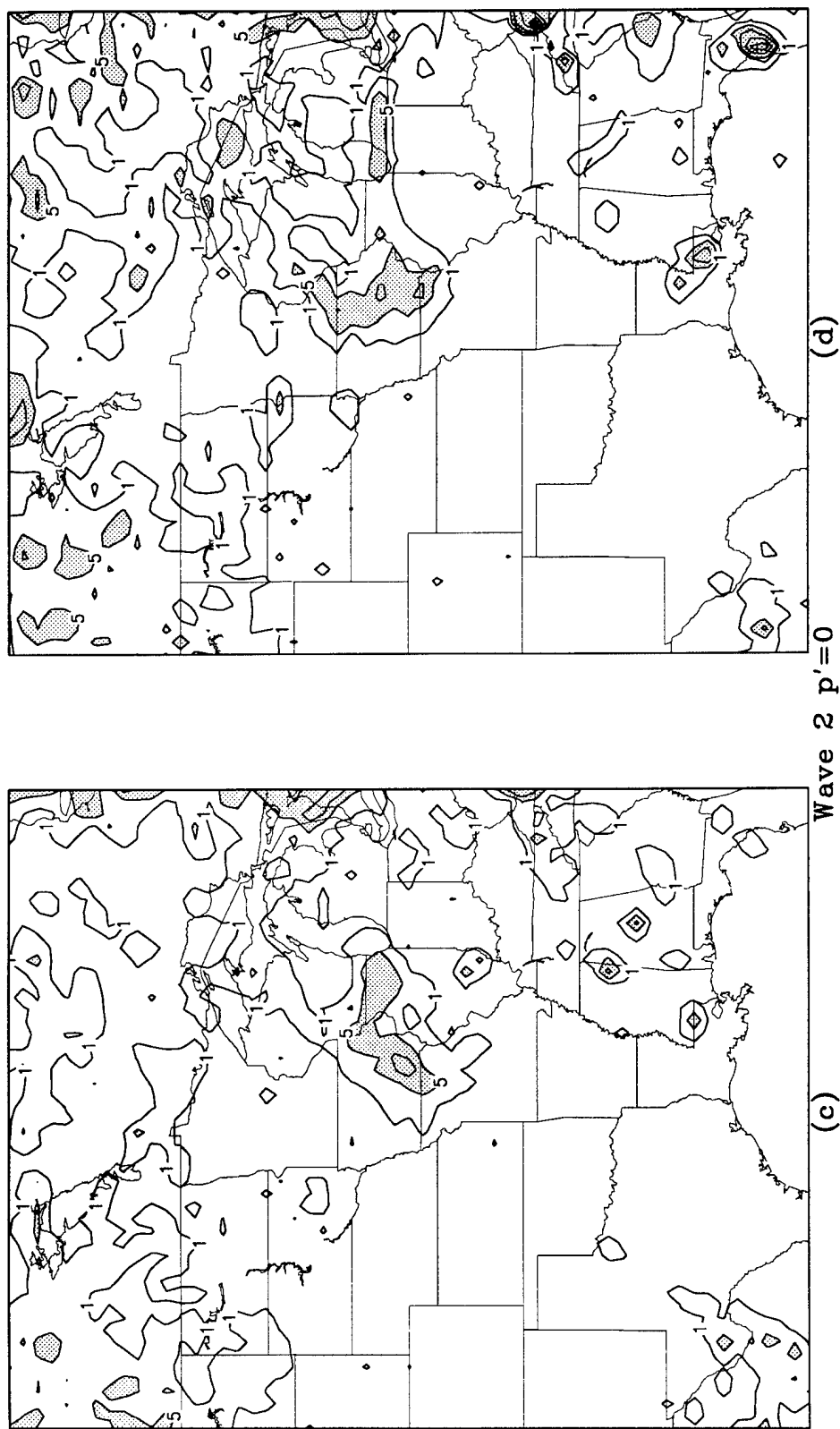


Figure 5.14. (Continued)

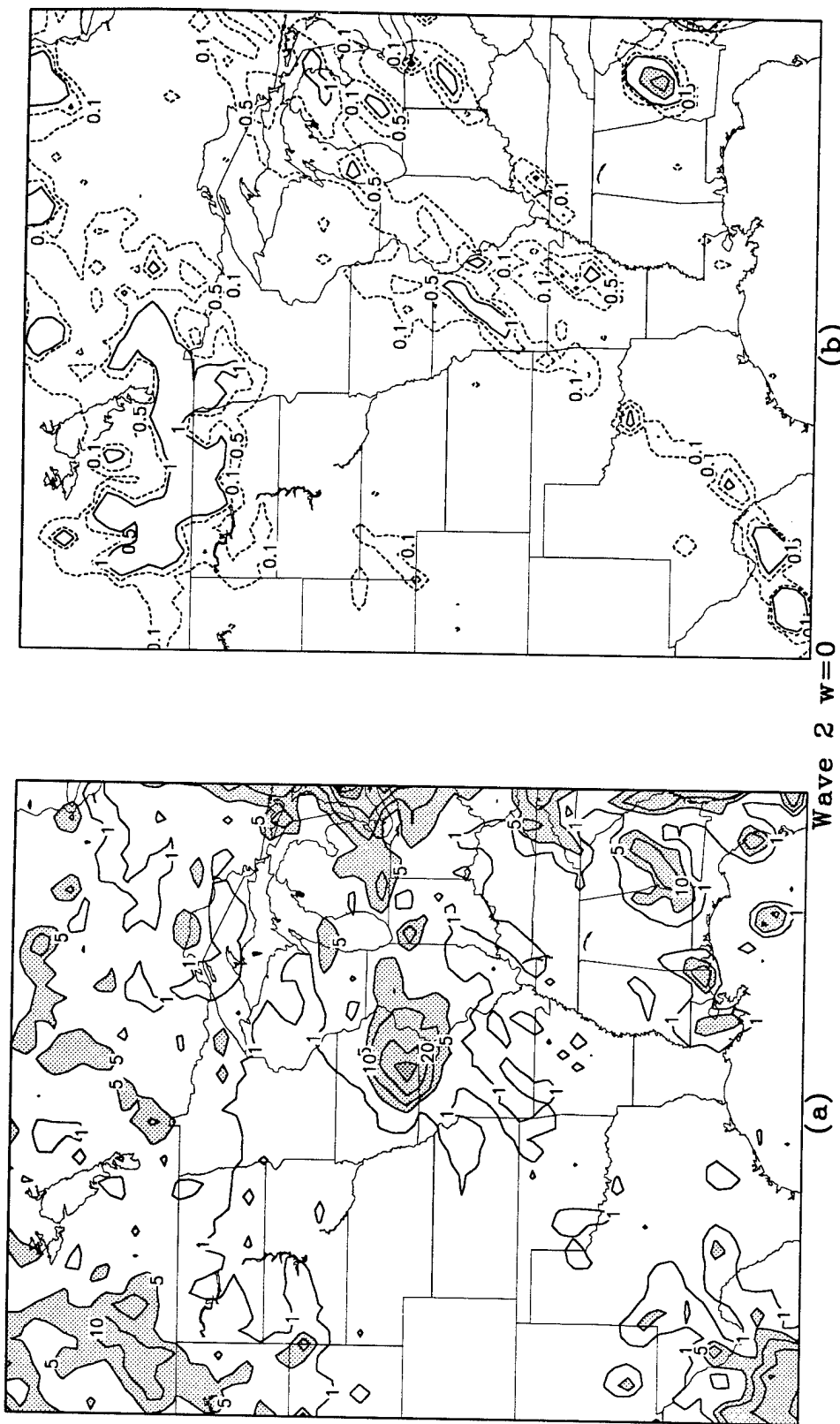


Figure 5.15. Utah LAM output from the wave 2 $w=0$ experiment: (a) 13-day total rainfall predicted for 0600 UTC 27 June to 0600 UTC 10 July, (b) 24-h rainfall predicted for 0600 UTC 27 June to 0600 UTC 10 July. In (a), contours are for 1, 5, 10, 20, 30, 40, 50, and 60 cm, with light shading above 5 cm and dark shading above 30 cm. In (b), contours are dashed for 0.1 and 0.5 cm and solid for 1, 5, 10, and 20 cm, with shading above 5 cm.

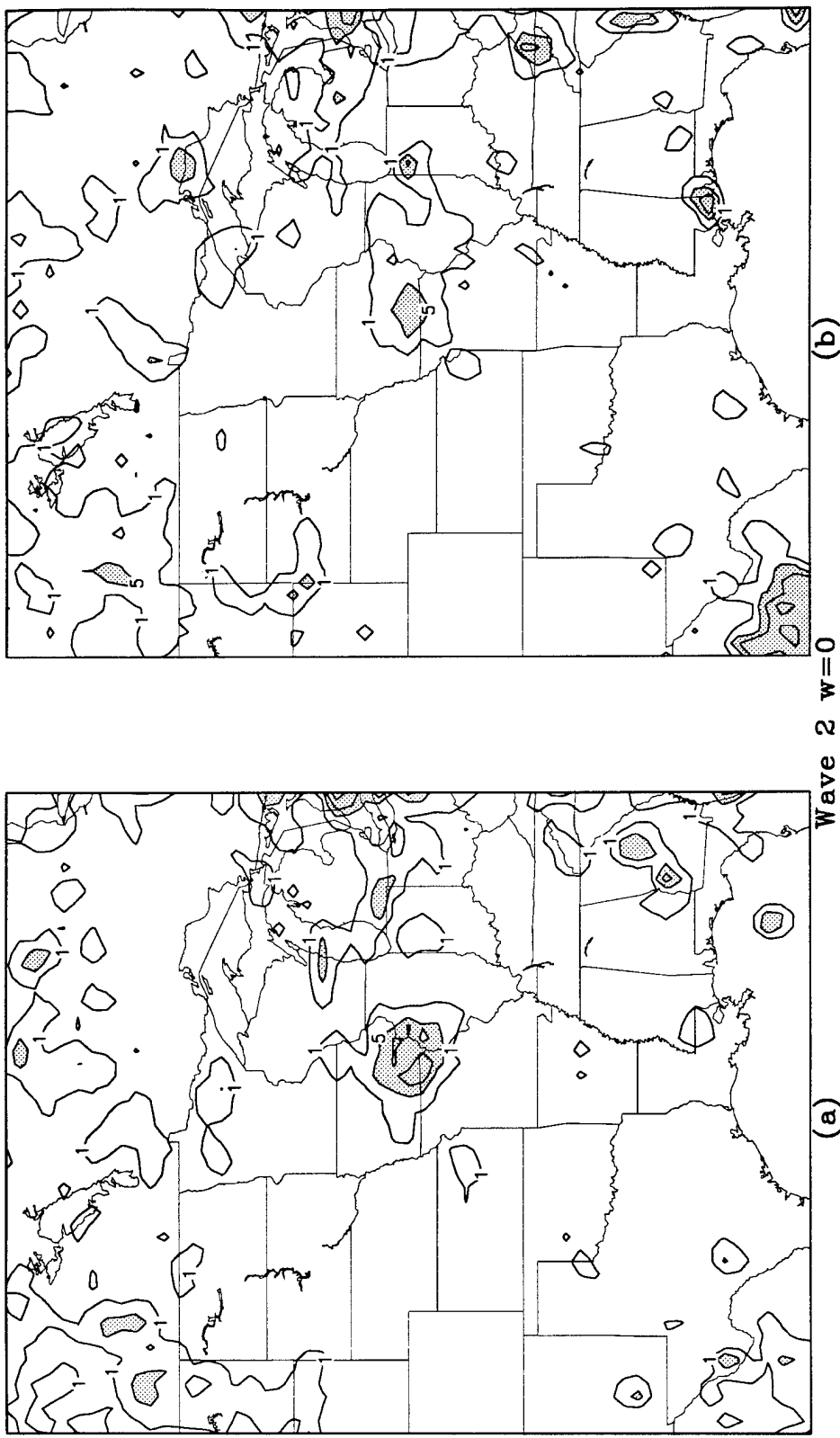


Figure 5.16. Utah LAM total precipitation during four 6-h time blocks for the 13-day period 27 June to 9 July 1993, as predicted by the wave 2 $w=0$ experiment. Each panel represents a different 6-h block: (a) 0000 to 0600 UTC, (b) 0600 to 1200 UTC, (c) 1200 to 1800 UTC, and (d) 1800 to 2400 UTC. Units are cm and contours are at 1, 5, 10, 20, 30, and 40 cm, with light shading above 5 cm and dark shading above 30 cm.

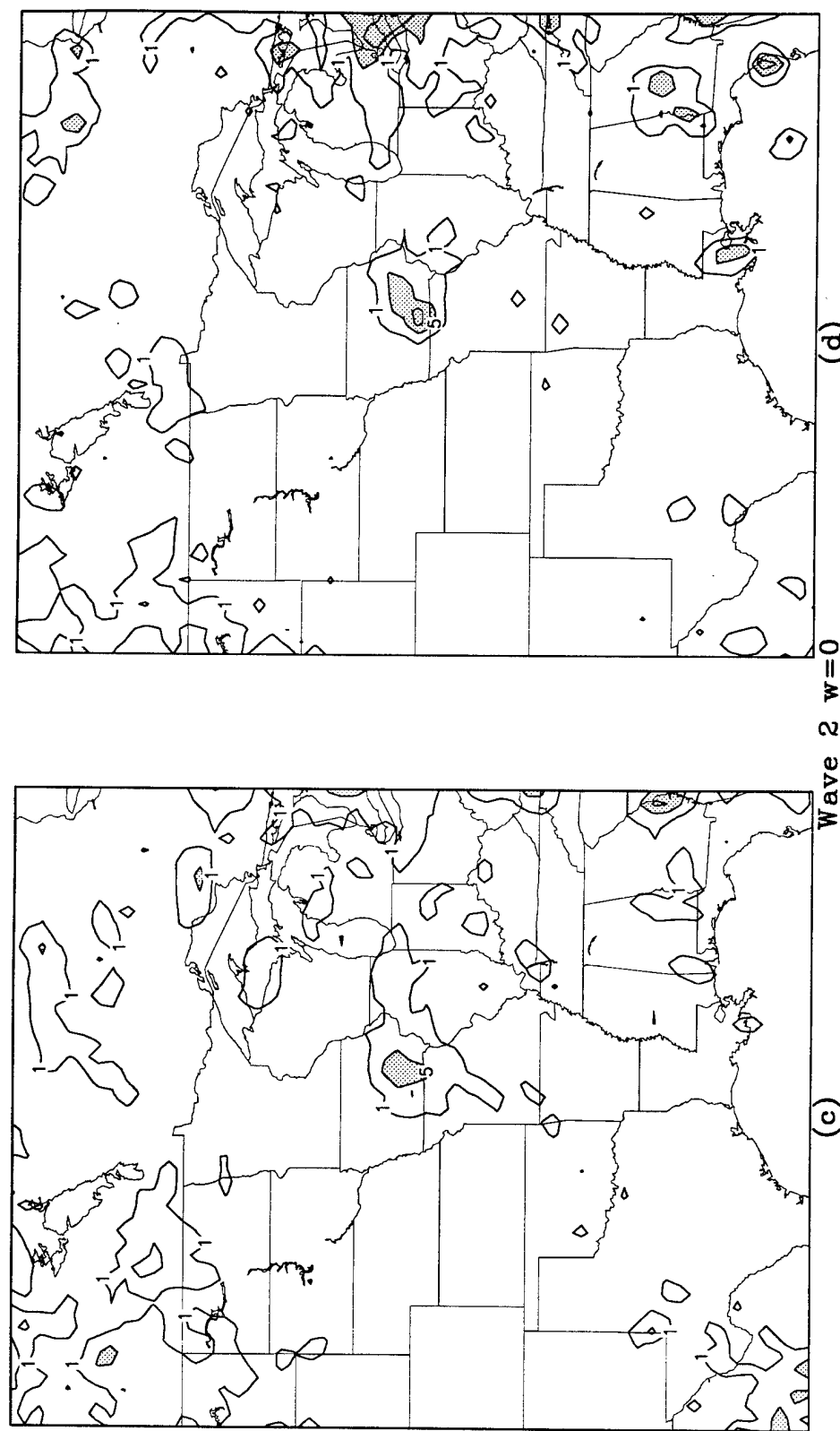


Figure 5.16. (Continued)

$w = 0$ experiment sustains the $w = 0$ trend to be more equal over the four 6-h time blocks.

To summarize, the wave relaxation on the $p' = 0$ upper boundary condition experiments tended to decrease the maximum 13-day rainfall total in Iowa and especially Illinois. Until the wave 2 relaxation was employed, the response in Kansas was slight but favorable, in that some precipitation was generated in areas that were otherwise dry. However, the underprediction of precipitation in Minnesota, the Dakotas, Nebraska, and Kansas was not remedied. For 5 July, the predicted rainfall increased with the implementation of wave 0 relaxation, then decreased steadily with the addition of wave 1 and wave 2, and the location remained unchanged. The lack of response by the 500-m wind field is not surprising because the spectral relaxation is applied above 3 km. What little changes were seen were likely driven by the changes in the precipitation generated by the LAM.

The spectral relaxation on the $w = 0$ upper boundary condition cases tended to decrease the 13-day rainfall totals in Iowa and Illinois, but only until the wave 2 relaxation was implemented. An additional trend with the $w = 0$ experiments was that as the wavenumber relaxation was increased, the 13-day maximum migrated from northern Illinois to southeast Iowa. The spectral relaxation on the $w = 0$ cases had a stronger effect on the 5 July 24-hour rainfall than it did in the $p' = 0$ cases.

CHAPTER 6

ATMOSPHERIC WATER FLUXES

The purpose of this chapter is to describe the sensitivity of simulated area-averaged precipitation and meridional water vapor transport to boundary conditions discussed in earlier chapters. Paegle et al. (1996) diagnosed the contributions of local surface evaporation to the 1993 summer rains and that due to a northward flux of atmospheric water vapor into the flood region. They concluded that the atmospheric transport was substantially larger than local surface evaporation. It was inferred that surface effects on the strength of the LLJ and on the resultant poleward flux of water vapor were more important to the rainfall than the positive feedback of locally enhanced surface evaporation.

The conclusion was supported by a series of controlled experiments with the Utah LAM in which reduced surface evaporation over the Southern Plains resulted in more rainfall over the flood region. Conditions of lower surface evaporation produced stronger buoyancy forcing of the southerly LLJ and increased horizontal flux of water vapor sufficiently to overcompensate for the reduced surface input of surface evaporation.

That explanation is made more plausible by Fig. 7 of Paegle et al. (1996) which shows that the northward flux of water vapor into the flood region is much larger than the precipitation rate over the flood region. They consequently conclude that "modifications of surface evaporation apparently are relatively more important in changing the buoyancy and resulting LLJ strength than they are in providing additional moisture to the already plentiful moisture influx from the Gulf of Mexico." Those simulations, however, underestimate the

precipitation and do not explore precipitation and atmospheric moisture transport dependency upon boundary conditions explored in the last two chapters.

Figure 6.1 presents results similar to those shown in Figs. 7 and 11a of Paegle et al (1996) for the first three experiments in Chapter 4. The left panels of this figure show the time variation of the forecast precipitation (open circles), influx of atmospheric water vapor through the south boundary (closed circles), and surface evaporation averaged over a region extending from 33°N to 45°N and 85.5°W to 120°W. This domain (illustrated by the solid box in the top right panel of Fig. 6.1) covers most of the flood region. The influx of atmospheric water vapor through the south boundary has been divided by the area of this domain and converted to units of cm day^{-1} to provide a measure of the potential precipitation that could have been supported entirely through atmospheric transport of water vapor through 33°N.

The atmospheric influx is substantially larger than either the area-averaged surface evaporation or the rainfall in each of the three experiments. This supports the inference that dynamical controls on the release of the already plentiful moisture supply may have been more critical to the floods than the positive feedback of increased surface evaporation. Mo et al. (1995) and Paegle et al. (1996) suggest that enhanced synoptic-scale cyclone activity and stronger LLJ activity may have provided the necessary dynamical modulation.

The right-hand panels of Figure 6.1 display the vertically integrated meridional moisture fluxes averaged over the 13-day period, for the first three experiments of Chapter 4. Each experiment displays a pronounced southwest-to-northeast-oriented band of poleward moisture transport, aligned approximately with the LLJ. The pattern is similar to that recently documented for different reanalyses climatologies summarized by Higgins et al (1996) as displayed in their Fig. 9. The presently computed fluxes are stronger than found by Higgins et al (1996) because the present period has more persistent cyclonic activity over the Rockies than found in the climatology.

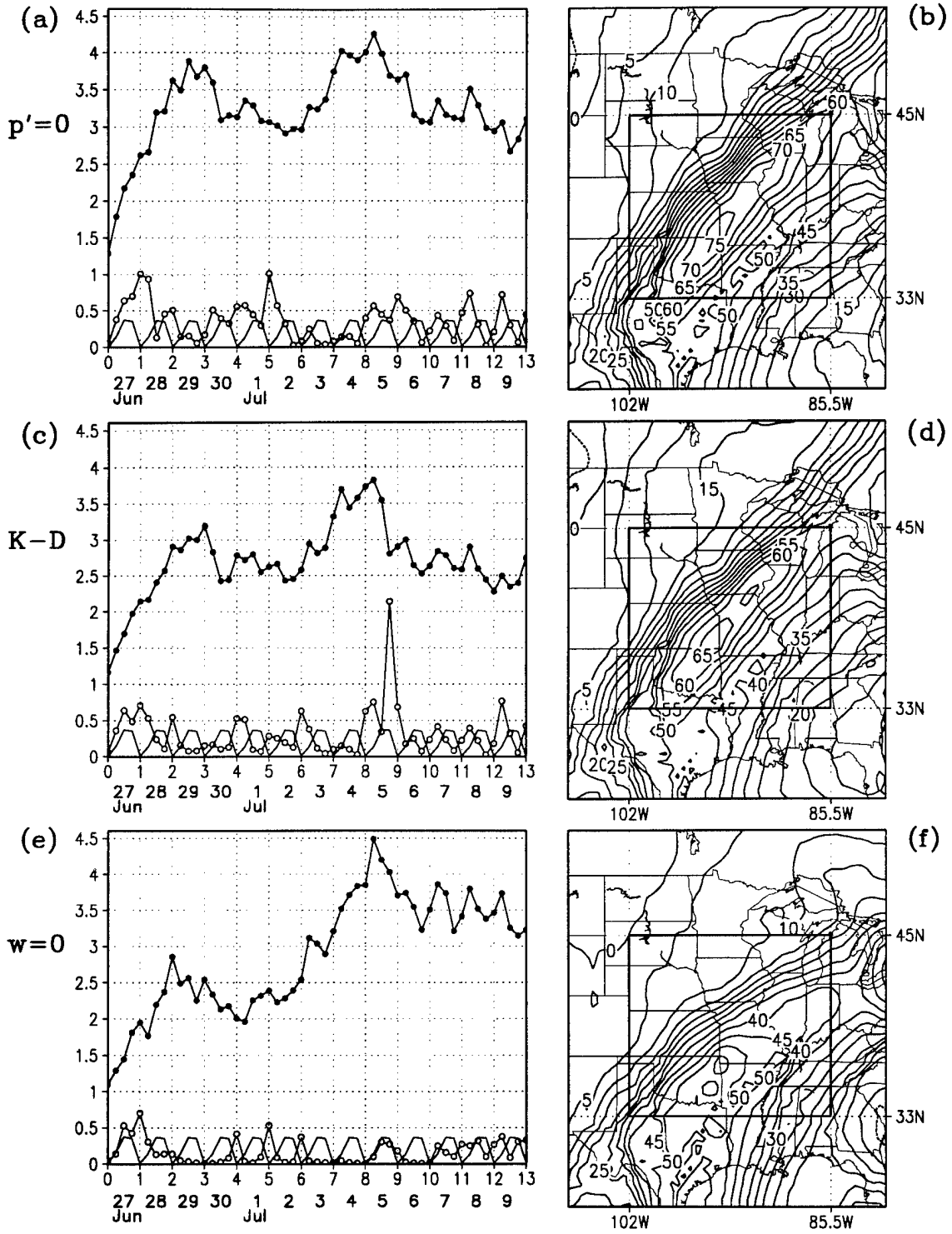


Figure 6.1. Panels (a), (c), and (e) show the area averaged rainfall (open circles) and evaporation (solid line) in the subdomain, and the vertically integrated meridional moisture flux (closed circles) through 33°N of the subdomain, at 6-h periods over the 13 days (units are cm day^{-1}). Panels (b), (d), and (f) show the vertically integrated meridional moisture flux averaged over the 13-day period (units are 10 kg m s^{-1}), and the area of the subdomain. Panels (a) and (b), (c) and (d), and (e) and (f), are for the $p'=0$, K-D, and $w=0$ experiments, respectively.

The peak meridional fluxes range from about 75 units for the case of the $p' = 0$ upper boundary condition (panel b of Figure 6.1) to about 45 units for the case of the $w = 0$ upper boundary conditions (panel f of Figure 6.1). The resultant 30% discrepancy is similar to that found by Higgins et al. (1996) between NCEP and NASA reanalyses after comparison of peak vector magnitudes in their Figs. 9 and 10. It is interesting to note that the largest discrepancies between the NCEP and NASA reanalyses occur along the axis of the LLJ.

Panels a and b of Figure 6.2 show the 13-day average of the vertically integrated meridional moisture flux as forecast/analyzed by the NGM and NCEP reanalysis models, respectively. The meridional flux is shown to be weaker than that from the Utah LAM simulations performed in this research and is consistent with the weaker LLJ shown in Chapter 3 (Figures 3.8 and 3.9).

Figure 6.3 presents results similar to those shown in Figure 6.1 for simulations using the NCEP reanalysis boundary conditions, as explained in Chapter 5. As previously mentioned, these experiments produce less rainfall and slightly weaker northerly LLJs and moisture transports than their NGM-driven counterparts in Figure 6.1.

Figures 6.4, 6.5, and 6.6 present results analogous for those shown in Figure 6.3, using the NGM boundary conditions and relaxation of waves 0, 1 and 2, respectively. These experiments produce less rainfall and slightly weaker northward moisture fluxes than results shown in corresponding experiments in Figure 6.1 that lacked spectral relaxation.

The diurnal modulation of evaporation is clearly evident in each of the evaporation curves of Figures 6.1 and 6.3-6.6. These are virtually identical in each of these experiments because the evaporation values are estimates from the NCEP operational global analysis for June 1993. Nighttime is identified as the time of zero evaporation. It is interesting to note that most experiments display more nocturnal rainfall peaks than daytime peaks, consistent with the notion that increased moisture availability due to the increased

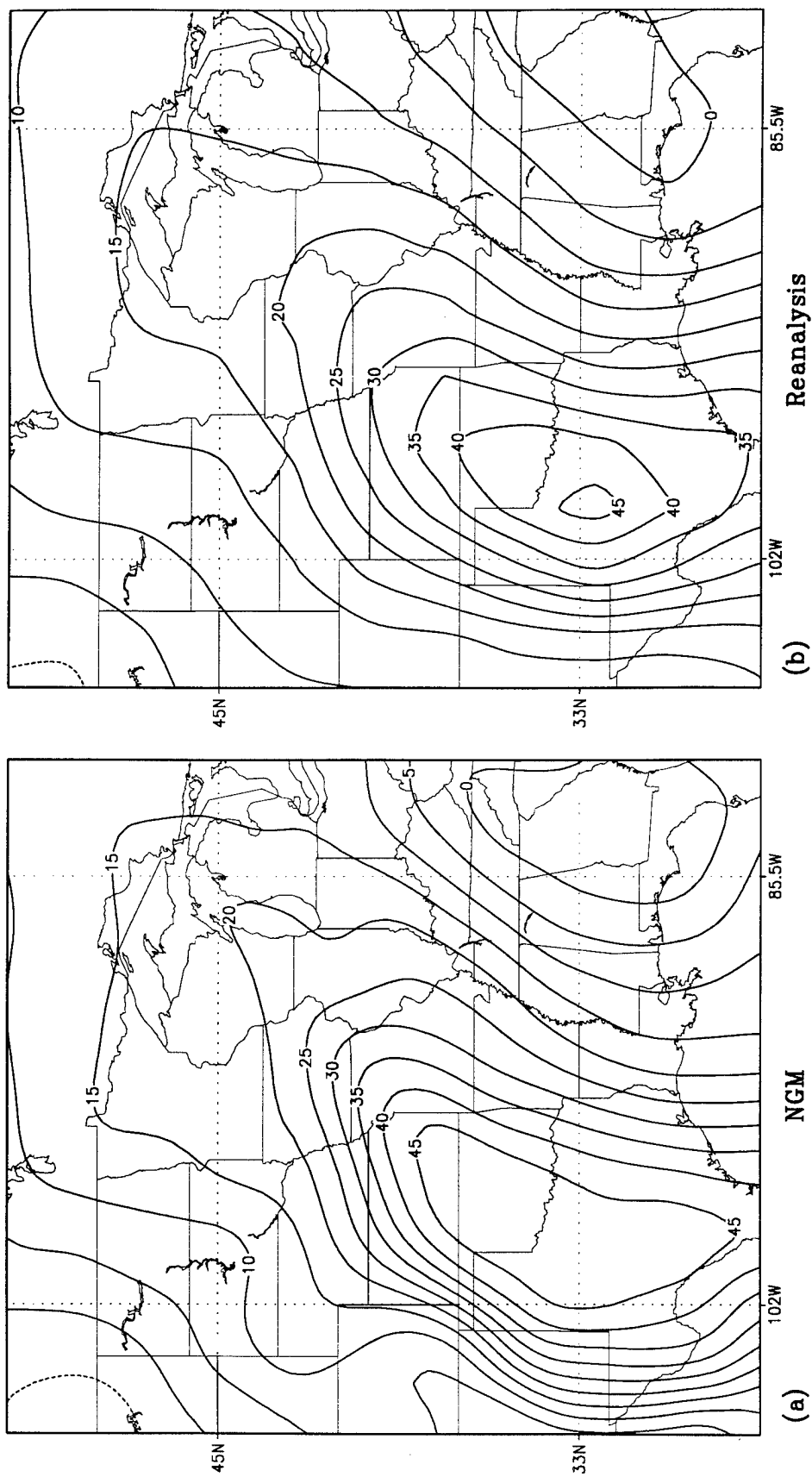


Figure 6.2. Vertically integrated meridional moisture flux averaged for the 13-day period 27 June to 9 July 1993, from (a) NCEP forecasts/analyses and (b) the NCEP reanalysis model. Units are 10 kg m s^{-1} .

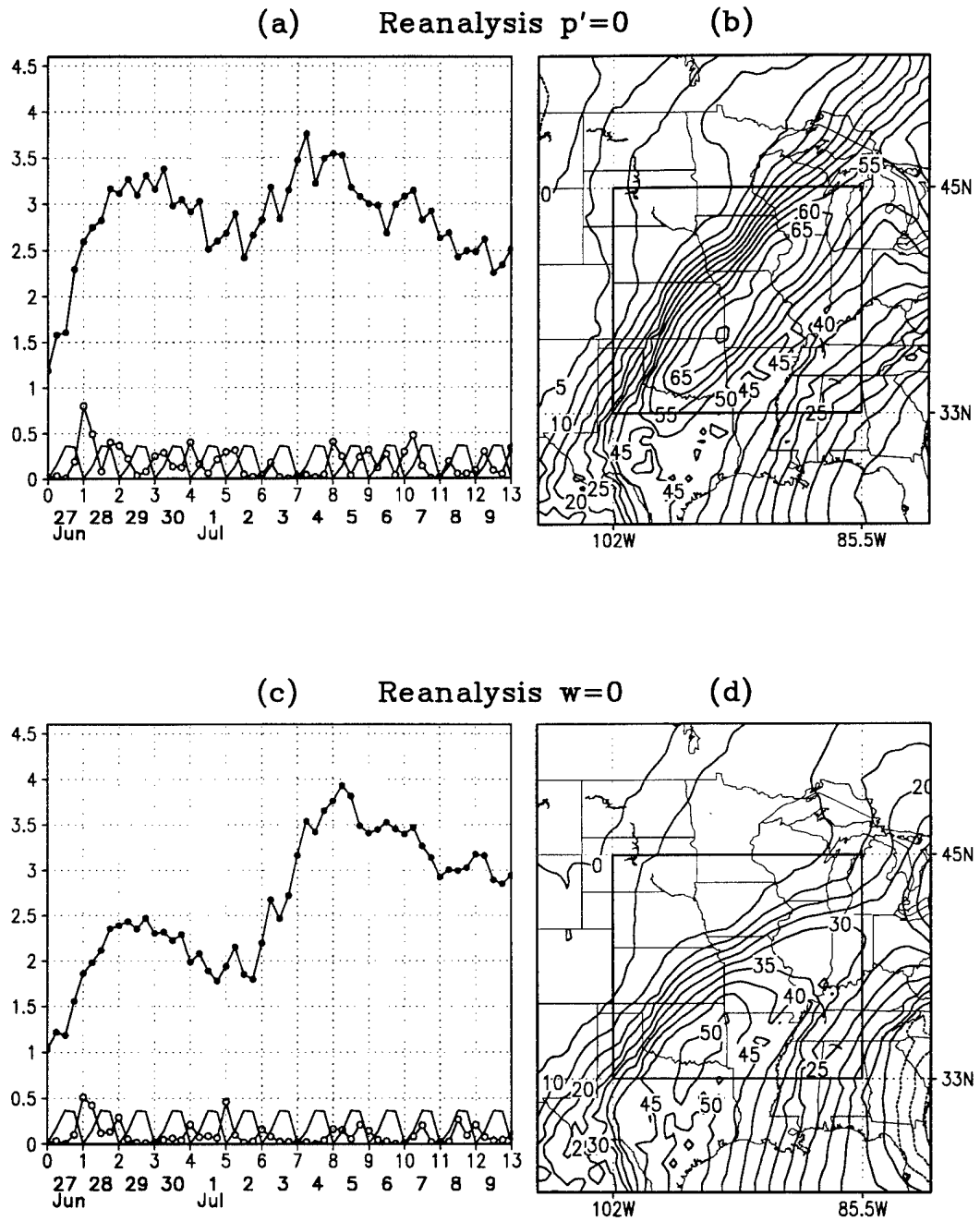


Figure 6.3. Panels (a) and (c) show the area averaged rainfall (open circles) and evaporation (solid line) in the subdomain, and the vertically integrated meridional moisture flux (closed circles) through 33°N of the subdomain, every 6 h over the 13 days (units are cm day^{-1}). Panels (b) and (d) show the vertically integrated meridional moisture flux averaged over the 13-day period (units are 10 kg m s^{-1}), and the area of the subdomain. Panels (a) and (b) are for the reanalysis $p'=0$ experiment and panels (c) and (d) are for the reanalysis $w=0$ experiment. Units are cm day^{-1} .

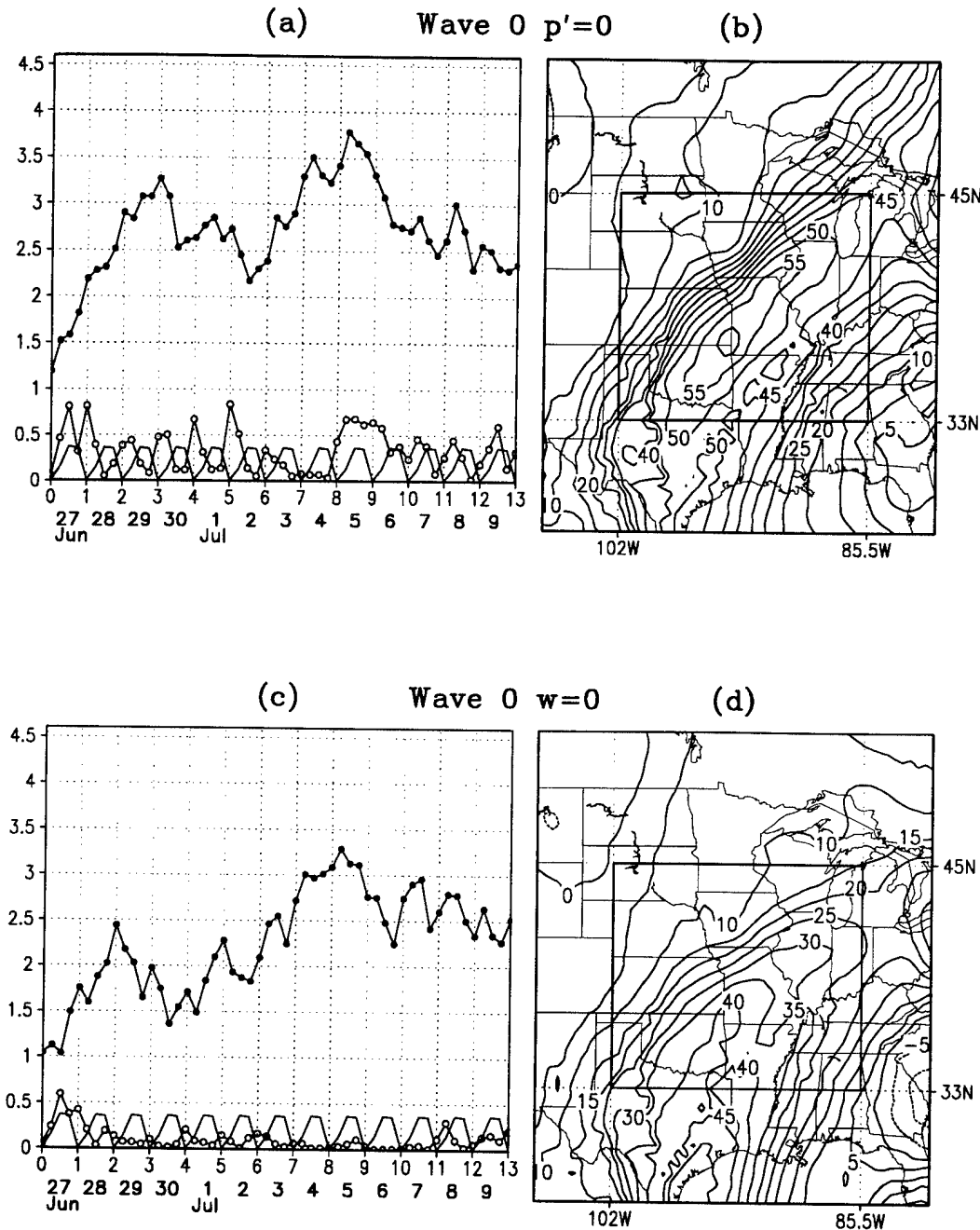


Figure 6.4. Panels (a) and (c) show the area averaged rainfall (open circles) and evaporation (solid line) in the subdomain, and the vertically integrated meridional moisture flux (closed circles) through 33°N of the subdomain, every 6 h over the 13 days (units are cm day^{-1}). Panels (b) and (d) show the vertically integrated meridional moisture flux averaged over the 13-day period (units are 10 kg m s^{-1}), and the area of the subdomain. Panels (a) and (b) are for the wave 0 $p'=0$ experiment and panels (c) and (d) are for the wave 0 $w=0$ experiment. Units are cm day^{-1} .

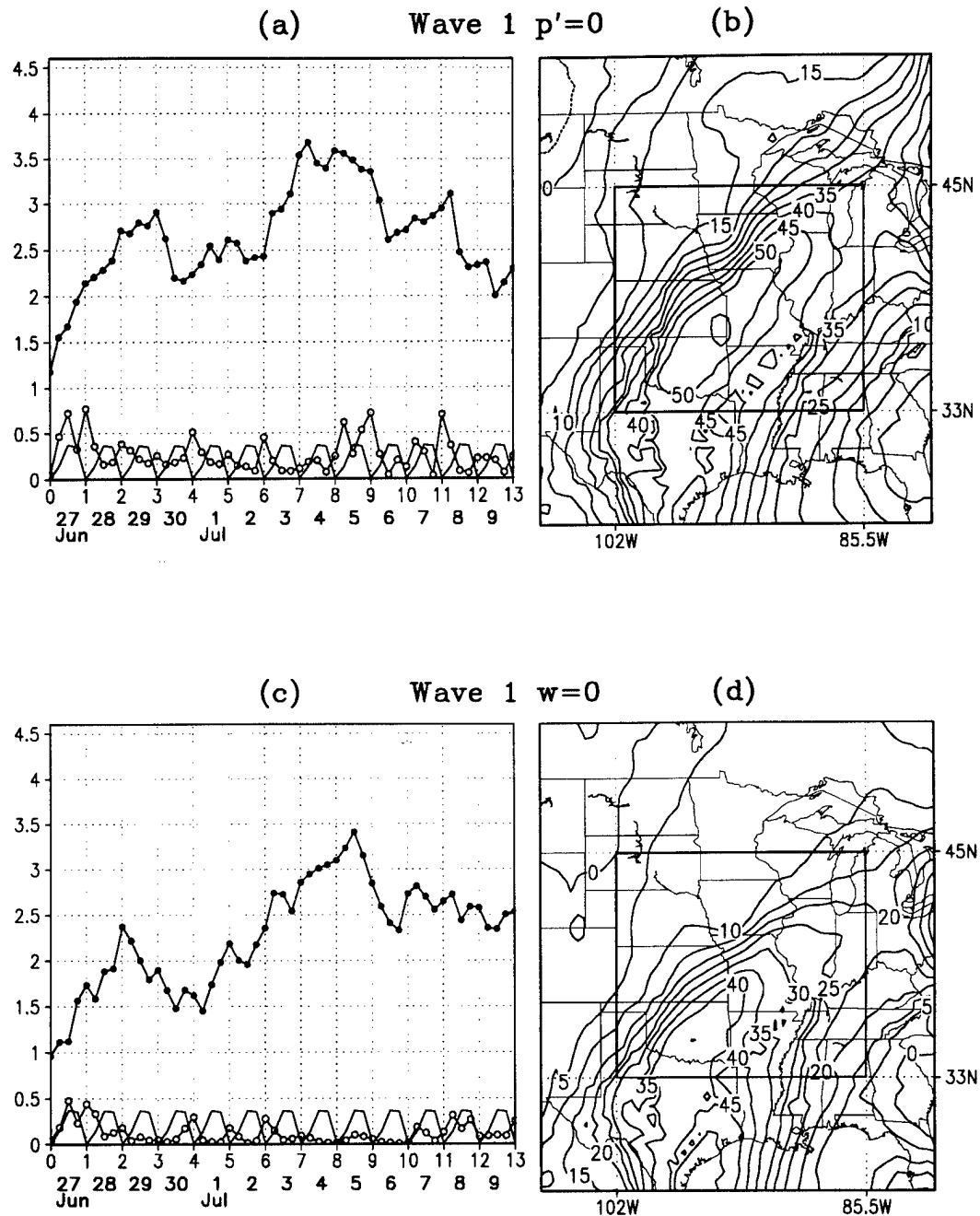


Figure 6.5. Panels (a) and (c) show the area averaged rainfall (open circles) and evaporation (solid line) in the subdomain, and the vertically integrated meridional moisture flux (closed circles) through 33°N of the subdomain, every 6 h over the 13 days (units are cm day^{-1}). Panels (b) and (d) show the vertically integrated meridional moisture flux averaged over the 13-day period (units are 10 kg m s^{-1}), and the area of the subdomain. Panels (a) and (b) are for the wave 1 $p'=0$ experiment and panels (c) and (d) are for the wave 1 $w=0$ experiment. Units are cm day^{-1} .

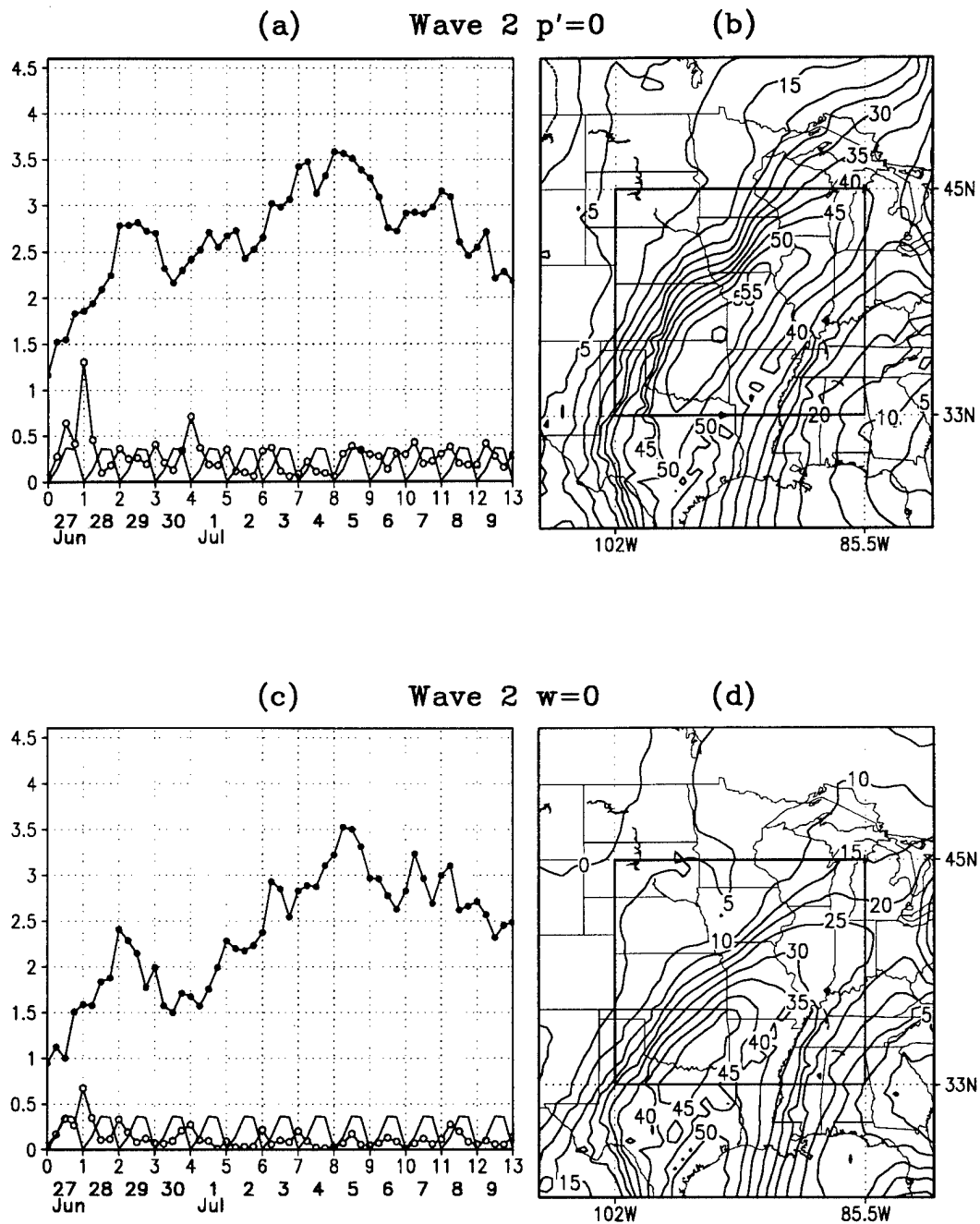


Figure 6.6. Panels (a) and (c) show the area averaged rainfall (open circles) and evaporation (solid line) in the subdomain, and the vertically integrated meridional moisture flux (closed circles) through 33°N of the subdomain, every 6 h over the 13 days (units are cm day^{-1}). Panels (b) and (d) show the vertically integrated meridional moisture flux averaged over the 13-day period (units are 10 kg m s^{-1}), and the area of the subdomain. Panels (a) and (b) are for the wave 2 $p'=0$ experiment and panels (c) and (d) are for the wave 2 $w=0$ experiment. Units are cm day^{-1} .

nocturnal southerly jet and its enhanced nocturnal convergence downwind of the jet core tend to control the precipitation timing.

The experiment which is most similar to the simulations presented in Paegle et al. (1996) corresponds to the lower two panels of Figure 6.6. This experiment evidently produces substantially less rainfall and somewhat weaker northward moisture fluxes than some of the prior experiments. However, in all cases the northward atmospheric moisture transport toward the flood region is substantially larger than either the flood-area-averaged rainfall or evaporation.

The top three rows of column 1 in Table 6.1 summarize area-averaged precipitation as obtained from station precipitation and the GrADS software, from gridded station data, and from the NCEP reanalysis precipitation for the flood region situated within the boxed subdomain displayed in the top right panel of Figure 6.1. The reanalysis precipitation is approximately 30%-40% larger than the observed estimates. The other rows of the first column represent the area-averaged precipitation as simulated by various experiments described in Chapters 4 and 5. All of these are smaller than observed, with the best simulations being the $p' = 0$ and K-D experiments with no wave relaxation or only relaxation of wave number zero. These experiments produce rainfall averages that are about 30%-40% too low. The worst experiments are the wave relaxation experiments using the $w = 0$ upper boundary condition. These produced only about 25% of the observed area-averaged precipitation.

The last two rows of Table 6.1 present results for two additional experiments which were not described in earlier sections. These experiments are identical to the unrelaxed experiments using the $p' = 0$ and $w = 0$ upper boundary conditions (rows 5 and 7 of Table 6.1). In these cases, however, certain treatments of the moisture variables are modified. In particular, the spectral filtering of waves of length two to four grid intervals (used in all other experiments) has been removed; the horizontal diffusion coefficient for the predictive equation of water substance has diminished to 10% of its prior value; and the

Table 6.1 Area averaged precipitation, area averaged evaporation, vertically integrated meridional moisture flux through the southern boundary of the subdomain, and flux divergence in the subdomain, averaged over the 13-day period 27 June to 10 July. The subdomain is 33°N to 45°N, 85°W to 102°W, as shown by the box in Figure 6.1b. Units are cm day^{-1} .

		Precipitation cm day^{-1}	Evaporation cm day^{-1}	Meridional Flux cm day^{-1}	Flux Divergence cm day^{-1}
Observations	Station Precipitation	0.47			
	Gridded Station Data	0.54			
Model forecast/ analyses	Reanalysis	0.69		1.68	-0.30
	NGM			2.29	-0.33
Experiments	$p' = 0$	0.36	0.21	3.22	-0.26
	K-D	0.32	0.21	2.70	-0.09
	$w = 0$	0.16	0.21	2.89	0.04
	Reanalysis $p' = 0$	0.17	0.21	2.84	-0.02
	Reanalysis $w = 0$	0.10	0.21	2.65	0.13
	Wave 0 $p' = 0$	0.33	0.21	2.71	-0.25
	Wave 0 $w = 0$	0.11	0.21	2.26	0.10
	Wave 1 $p' = 0$	0.27	0.21	2.64	-0.22
	Wave 1 $w = 0$	0.12	0.21	2.28	0.11
	Wave 2 $p' = 0$	0.28	0.21	2.67	-0.22
	Wave 2 $w = 0$	0.13	0.21	2.37	0.08
	$p' = 0$, NGM, no relaxation, no q filter, weak diffusion, 95 % RH.	0.44	0.21	2.93	-0.06
	$w = 0$, NGM, no relaxation, no q filter, weak diffusion, 95% RH.	0.24	0.21	2.86	-0.47

criterion defining grid square condensation has been reduced from 100% to 95%.

These modifications allow a more nearly conservative prediction of water vapor and permit local condensation within a grid square before the entire square is saturated. They thus constitute conditions that are commonly used in other simulations which pay special attention to conservation of water substance and allow for subgrid variability of condensation. It is noteworthy that these changes double the amount of precipitation produced by the $w = 0$ boundary condition for the wave-nudged cases, and increase it by 50% with respect to values produced by the $w=0$ upper boundary condition for the unrelaxed cases.

The second column of Table 6.1 presents the area and time-averaged evaporation over the flood subdomain, the third column presents the average simulated meridional moisture flux through its south boundary expressed in units of cm day^{-1} as in the curves of Figures 6.1 and 6.3-6.6, and the last column represents the flux divergence within the subdomain (also in cm day^{-1}). The moisture fluxes vary from 1.68 cm day^{-1} for the NCEP reanalysis to almost twice this for the simulation using $p' = 0$ upper boundary conditions and no wave relaxation. In comparison, the NGM analysis and 6-h forecast archive produce a value of 1.97 cm day^{-1} . The large discrepancies in moisture fluxes are consistent with those found in prior reanalysis intercomparisons by Higgins et al. (1996) and in other data archives by Wang and Paegle (1996).

Column 1 of Table 6.1 provided estimates of time and area-averaged precipitation in the Upper Mississippi River Basin. Although these values can be used to assess the model performance over the 13-day period, they do not distinguish whether or not the Utah LAM captured the daily variation of the precipitation events. Figure 6.7 illustrates that the Utah LAM showed little success in predicting the periods of heavier rainfall. Panel a displays the time series of area-averaged rainfall (cm day^{-1}), within the subdomain outlined in Figure 6.1b, from the CPC-gridded station data (closed circles) and the Utah LAM forecast from the $p' = 0$ experiment (open circles). Panel b shows the same CPC-gridded station

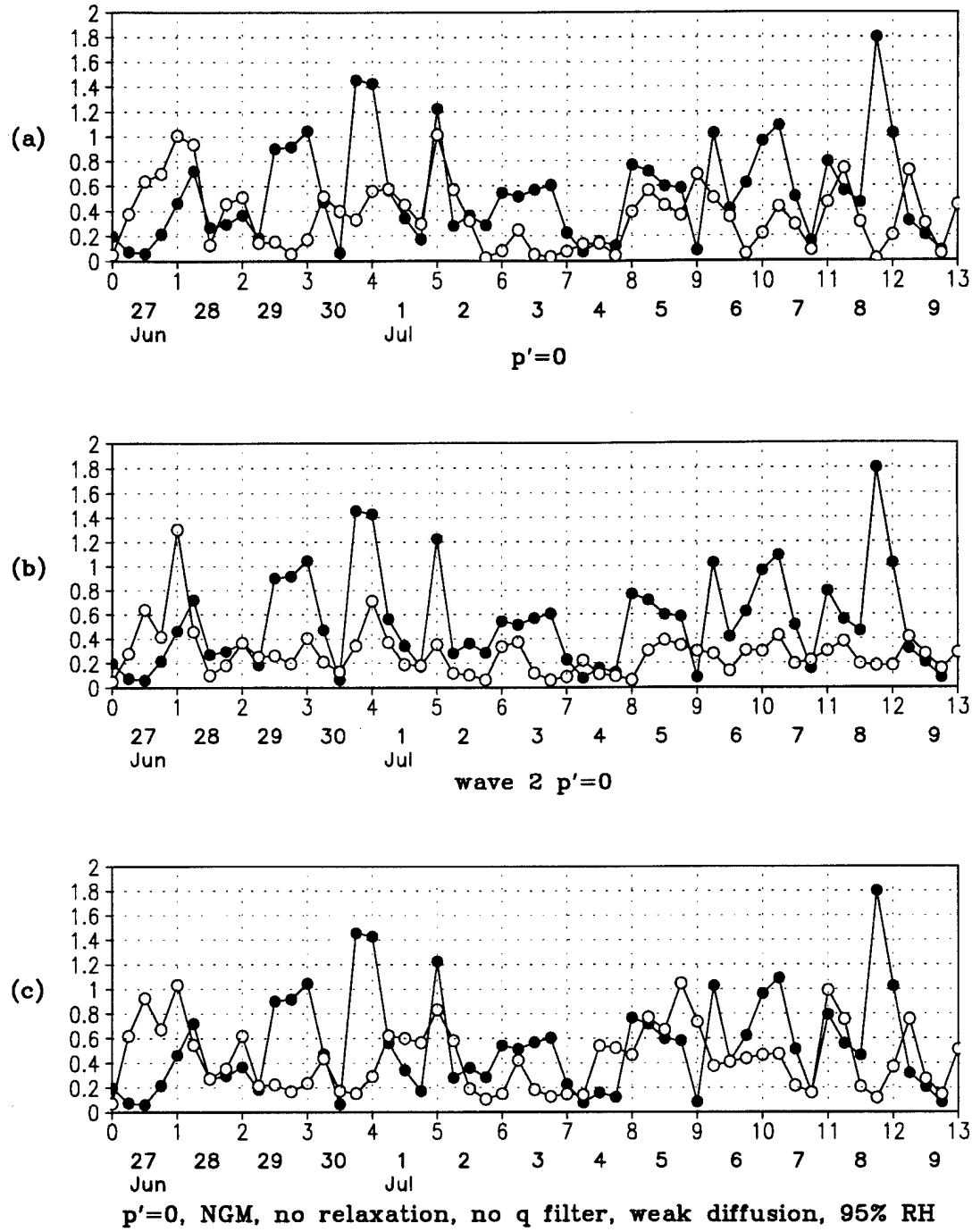


Figure 6.7. Time series of area averaged precipitation in subdomain bounded by 33°N , 45°N , 85.5°W , and 102°W (cm day^{-1}) plotted every 6 h from 0600 UTC 27 June to 0600 UTC 10 July, 1993. All three panels show the CPC-gridded station data (closed circles) plotted with the Utah LAM output from one simulation. Open circles in (a) $p' = 0$ experiment, (b) wave 2 $p' = 0$ experiment, and (c) $p' = 0$, NGM, no relaxation, no q filter, weak diffusion, 95% RH experiment.

data (closed circles) and the wave 2 $p' = 0$ experiment results (open circles), and panel c shows the results from the additional $p' = 0$ experiment (not described in detail) with the modified moisture variable treatment. These three cases show little change in the day-to-day variation of precipitation. The timing of the relative peaks is similar among these three simulations, but the magnitudes show a greater difference.

CHAPTER 7

CONCLUSIONS

The goals of this investigation have been to describe the sensitivity of the Utah LAM to specification of upper and lateral boundary conditions. The emphasis is upon recently developed upper boundary and lateral boundary conditions, whose impacts have been previously examined only in limited individual case studies. The approach used NCEP analysis and model guidance to provide initial data and upper and lateral boundary conditions for the Utah LAM. The upper boundary conditions included the commonly used $p' = 0$ specification, as well as gravity wave transmitting conditions proposed by Klemp and Durran (1983) and rigid lid ($w = 0$) specifications that are extensions of methods suggested by Innocentini et al. (1993).

The validation procedures emphasized a 13-day period during the summer 1993 Mississippi River Basin floods. Model simulations of total rainfall and rainfall during one particularly wet event were compared to observed rainfall and rainfall analyzed by other analysis methods. More detailed verification statistics such as threat scores were not computed because the level of model skill was obviously too low to justify such an effort. All model forecasts produced a wet region centered approximately on Iowa and dry areas south and west of this region. The observations show heavy rainfall over Iowa and also indicate heavy rain to the southwest of Iowa over parts of Nebraska, Kansas, and Oklahoma. The Utah LAM underforecast precipitation in these regions, where the NCEP reanalysis rainfall was in better agreement with observations.

The Utah LAM was able to resolve a relatively drier tongue extending over Kentucky and Tennessee and another wet region over the southeast, in approximate agreement with observed rainfall patterns. The details of these structures and the rainfall magnitudes over Iowa depend relatively upon the specification of boundary conditions, as summarized below. In some simulations these patterns were in closer agreement with observations than were the NCEP reanalyses which missed the drier tongue over Kentucky and Tennessee.

The model displays substantial sensitivity to specification of upper boundary conditions. Both the $p' = 0$ and the K-D upper boundary conditions overestimated rainfall over Iowa whereas the closed upper boundary condition of Innocentini et al. (1993) underestimated rainfall over Iowa and reduced the region of heavy rainfall compared to the other simulations. This may explain the relatively small region of rainfall in the flood simulations of Paegle et al. (1996).

The Utah LAM displays substantial sensitivity to the outer model used to provide initial and boundary conditions. The best simulations of rainfall were driven by NGM analyses and 6-h forecasts together with the $p' = 0$ upper boundary conditions. These simulations produced substantially more rain over the southeast than did the Utah LAM driven by reanalysis boundary conditions.

Spectral relaxation produced smaller modifications than those due to changes of the outer model (NGM or reanalysis) or due to the type of upper boundary condition. It appears that $p' = 0$ and K-D upper boundary conditions produce excessive rainfall over some portions of the domain, whereas the $w = 0$ upper boundary condition underestimates the rainfall in most regions. The $w = 0$ upper boundary condition produces the most economical forecasts, because these can be executed with a longer time step and also appear to be the most stable upper boundary conditions. It is not surprising that $w = 0$ upper boundary conditions produce the least rainfall, because they most strongly limit the vertical extent of the rising motion.

It would be useful to determine whether the unrealistically small precipitation in this case is due to the relatively low position (14.5 km) of the upper boundary. Ciliberti (unpublished master's thesis draft) finds that for shorter term winter conditions this boundary condition produces similar precipitation as the $p' = 0$ and K-D boundary conditions. Winter precipitation events are usually more shallow than summertime cases.

Another potential deficiency is that the present version of the $w = 0$ upper boundary condition is applied in the terrain following model coordinate, rather than in the customary z coordinate. Consequently the model wind at the upper boundary is constrained to flow parallel to this surface, implying a topographic "wedging" effect at the level of the upper boundary. It would be useful to explore ways to generalize this boundary condition so that it applies to vertical velocity with respect to the regular z coordinate. Finally, precipitation forecasts are known to be sensitive to a variety of physical processes which are highly parameterized in the present model. Future research should continue to examine the sensitivity of the Utah LAM precipitation forecasts to these processes, which were shown to substantially influence the precipitation in the $w = 0$ upper boundary case in Chapter 6.

It would also be useful to examine the model simulated LLJ, which appears to be too strong. Unfortunately, available radiosonde guidance is insufficient to compare with the 500 m wind field predicted by the model. The observed Great Plains LLJ is most active around local midnight, or slightly later, at times lacking radiosonde observations. Future research should compare the model forecasts against the demonstration profiler observations which became available in 1993.

Although the simulations are quite sensitive to boundary conditions and other uncertainties, all of these are consistent with earlier conclusions by Mo et al. (1995) and Paegle et al. (1996) in regard to the dominant role of enhanced atmospheric moisture transports during the 1993 floods.

REFERENCES

Astling, E. G., J. Paegle, E. Miller, and C. J. O'Brien, 1985: Boundary layer control of nocturnal convection associated with a synoptic scale system. *Mon. Wea. Rev.*, **113**, 540-552.

Blackadar, A. K., 1957: Boundary layer wind maxima and their significance for the growth of nocturnal inversions. *Bull. Amer. Meteor. Soc.*, **38**, 283-290.

Bonner, W. D., S. Esbensen, and R. Greenberg, 1968: Kinematics of the low-level jet. *J. Appl. Meteor.*, **7**, 339-347.

Ciliberti, C. M., 1996: Sensitivity of the Utah limited area model to upper boundary conditions. Unpublished master's thesis draft, University of Utah, 72pp.

Davies, H. C., 1976: A lateral boundary formulation for multi-level prediction models. *Quart. J. Roy. Meteor. Soc.*, **102**, 405-418.

Higgins, R. W., K. C. Mo, and S. D. Schubert, 1996: The moisture budget of the central United States in spring as evaluated in the NCEP/NCAR and NASA/DAO reanalyses. *Mon. Wea. Rev.*, **124**, 939-963.

Holton, J. R., 1967: The diurnal boundary-layer wind oscillation above sloping terrain. *Tellus*, **19**, 199-205.

Innocentini, V., N. S. Ferreira, and C. N. E. Dos Santos, 1993: A simple numerical method for hydrostatic incompressible models with rigid lids. *Mon. Wea. Rev.*, **121**, 3438-3442.

Juang, H. M. H., and M. Kanamitsu, 1991: Regional spectral modeling in NMC. *Preprint Volume of the Ninth Conference on Numerical Weather Prediction of the American Meteorological Society*, 14-18 Oct. 1991, Denver, CO, 270-273.

Kalnay, E., M. Kanamitsu, R. Kistler, W. Collins, D. Deaver, L. Gandin, M. Iredell, S. Saha, G. White, J. Woollen, Y. Zhu, M. chelliah, W. Ebisuzaki, W. Higgins, J. Janowick, K. C. Mo, C. Ropelewski, J. Wang, A. Leetmaa, R. Reynolds, R. Jenne, and D. Joseph: The NCEP/NCAR 40-year reanalysis project. *Bull. Amer. Meteor. Soc.*, **77**, 437-471.

Klemp, J. B., and D. R. Durran, 1983: An upper boundary condition permitting internal gravity wave radiation in numerical mesoscale models. *Mon. Wea. Rev.*, **111**, 430-444.

Kondratyev, J., 1969: *Radiation in the Atmosphere*. Academic Press. 912pp. (187-202).

Lorenz, E. N., 1969: The predictability of a flow which possesses many scales of motion. *Tellus*, **21**, 289-307.

Mo, K. C., J. N. Paegle, and J. Paegle, 1995: Physical mechanisms of the 1993 summer floods. *J. Atmos. Sci.*, **52**, 879-895.

Nicolini, M., K. M. Waldron, and J. Paegle, 1993: Diurnal oscillations of low-level jets, vertical motion and precipitation: A model case study. *Mon. Wea. Rev.*, **121**, 2588-2610.

Nordeng, T. E., 1986, Parameterization of physical processes in a three-dimensional numerical weather prediction model. Tech. Report #65, Det Norske Meteorologiske Institutt, ISSN 0332-9879, 48pp.

Paegle, J., and D. W. McLawhorn, 1983: Numerical modeling of diurnal convergence oscillations above sloping terrain. *Mon. Wea. Rev.*, **111**, 67-85.

_____, K. C. Mo, and J. N. Paegle, 1996: Dependence of simulated precipitation on surface evaporation during the 1993 United States summer floods. *Mon. Wea. Rev.*, **124**, 345-361.

_____, and T. Vukicevic, 1987: On the predictability of low-level flow during ALPEX. *Meteor. Atmos. Phys.*, **36**, 45-60.

Perkey, D. J., and C. W. Kreitzberg, 1976: A time-dependent lateral boundary scheme for limited-area primitive models. *Mon. Wea. Rev.*, **104**, 744-755.

Ross, B. B., and I. Orlanski, 1982: The evolution of an observed cold front. Part I: Numerical Simulations. *J. Atmos. Sci.*, **39**, 296-327.

Sellers, P. J., 1987: Modeling effects of vegetation on climate. *The Geophysiology of Amazonia: Vegetation and Climate Interactions*, R. E. Dickinson, Ed., Wiley and Sons, 526pp.

Thompson, P. D., 1957: Uncertainty of initial state as a factor in the predictability of large scale atmospheric flow patterns. *Tellus*, **9**, 275-295.

Vukicevic, T., 1989: The influence of lateral boundary conditions, fixed surface forcings, and synoptic situations upon predictability estimates using limited area numerical models. Ph.D. dissertation, University of Utah, 132pp.

_____, and J. Paegle, 1989: The influence of one-way interacting lateral boundary conditions upon predictability of flow in bounded numerical models. *Mon. Wea. Rev.*, **117**, 340-350.

_____, and R. M. Errico, 1990: The influence of artificial and physical factors upon predictability estimates using a complex limited-area model. *Mon. Wea. Rev.*, **118**, 1460-1482.

Waldron, K. M., 1994: Sensitivity of local model prediction to large scale forcing. Ph.D. dissertation, University of Utah, 150pp.

_____, J. Paegle, and J. D. Horel, 1996: Sensitivity of a spectrally filtered and nudged limited-area model to outer model options. *Mon. Wea. Rev.*, **124**, 529-547.

Welch, R. M., 1976: A numerical simulation of the polluted atmospheric boundary layer. Doctoral dissertation, University of Utah, 173pp.

Williamson, D. L., J. T. Kiehl, V. Ramanathan, R. E. Dickinson, and J. J. Hack, 1987: *Description of NCAR Community Climate Model (CCM1)*. NCAR/TN-285+STR, NCAR Tech. Note, 112pp. [Available from authors at the National Center for Atmospheric Research, P.O. Box 3000, Boulder, CO, 80307-3000.]

Wurtele, M. G., J. Paegle, and A. Sielecki, 1971: The use of open boundary conditions with the storm-surge equations. *Mon. Wea. Rev.*, **99**, 537-544.

Yamada, T., and S. Bunker, 1989: A numerical model study of nocturnal drainage flows with strong wind and temperature gradients. *J. Appl. Meteor.*, **28**, 545-554.

Yang, Q., 1992: Predictability of mesoscales in a variable resolution barotropic global model. M.S. thesis, University of Utah, 45pp.